Effects of 304 Stainless Steel Microstructure on Short-Time Corrosion in High Temperature Water

Submitted in partial fulfillment of the requirements for

the degree of

Doctor of Philosophy

in

Materials Science and Engineering

Rachel E. Turfitt

B.S., Biological Sciences, State University of New York at Buffalo
B.S., Metallurgical and Materials Engineering, Colorado School of Mines
M.S., Materials Science and Engineering, Carnegie Mellon University

Carnegie Mellon University
Pittsburgh, PA

May 2022

Abstract

Austenitic stainless steels of the 300 series are commonly used for low to moderate temperature air and high temperature, high pressure water environments that are found in the primary coolant loop of pressurized water reactors due to their corrosion resistance, low cost, wide availability, weldability, and formability. Understanding the material condition and environmental combinations that may be present in a pressurized water reactor can help make the reactors safer with longer lifespans through material selection insight and predictive modelling. The austenite phase present in some grades of the 300 series, including 304, is metastable and can be transformed to martensite through cooling and deformation. In this work, surface condition and its oxidation effects are studied in air at 280, 400, and 700 °C for 50 hours and plastic strain and surface finish oxidation effects are studied in pressurized water at 280 °C for 10, 50, and 100 hours. Deformation microstructures accompanying each condition vary: surface preparation can result in a deformation zone localized to the near surface while plastic strain results in uniform deformation throughout the thickness with potentially deformation-induced martensite. Martensite results in a higher density of grain boundaries and also has a different crystal structure than austenite leading to differences in diffusion kinetics between the two phases. Differences between the deformation microstructures can alter the oxidation behavior; various surface conditions and material plastic strain are present as a material starting condition in nuclear reactors and can affect material degradation.

Uniaxial tension and plastic strain are characterized for 304 at 21, 250, and 338 °C on cold worked and mill annealed conditions. Prior material condition leads to differences in mechanical behavior and martensite transformation upon deformation: the cold worked samples result in lower strain at failure and deformation induced martensite is found to occur in all samples at low temperature and in the cold worked samples at high temperatures. Local misorientation provides a proxy for plastic strain for specific testing conditions. A relationship between axial and lateral strain is derived and tested for isotropic and anisotropic materials up to necking.

High temperature deformation induced martensite is shown to form in specimens that

contain cold work prior to high temperature tension. Deformation induced martensite in the 300 series is reported to be limited to occur exclusively at low temperatures (less than 100 °C), although it is shown in this work to occur as high as 347 °C. High temperature deformation induced martensite can increase or decrease oxidation kinetics when formation occurs inside an environmentally assisted crack.

Surface preparation and martensite content are studied in low temperature air at 280, 400, and 700 °C in a thermogravimetric analyzer. Surface preparation can leave a deformation layer that extends a few microns in depth into the material; a fine grained layer forms on the outer most layer with deformation bands at a deeper level. The finer grain structure increases the grain boundary surface area which can act as fast diffusion paths for alloying elements, changing the oxidation behavior of the material. The mass of oxide formed on the surface is too small to be resolved in the thermogravimetric analyzer. Scanning electron microscopy did confirm that an oxide layer(s) formed as a result of the low temperature air exposure.

Macroscale corrosion properties of austenitic stainless steel in high temperature water conditions have been studied extensively at long exposure time, although effects of microstructural and phase differences within these steels at short exposure times are largely unknown. Tensile specimens with a range of plastic strain and machined surface finish are exposed to high temperature water for 10, 50, and 100 hours. Polished surface finish with plastic strain and a range of surface finishes with and without cold work are oxidized for 100 hours in high temperature water. The resulting oxide thickness for all exposures is determined by plasma focused ion beam milling and scanning electron microscopy imaging of the cross sections. Inner oxide thickness is modeled as a parabolic rate law. The effect of plastic strain and surface finish are concomitant. The effect of plastic strain is linked with deformation induced martensite in the near surface structure. Surface finishing exhibits a positive correlation between oxide thickness and finishing particle size. A metallic nickel rich phase is seen in place of an outer oxide and the inner oxide contained metallic phase embedded within a variable density inner oxide. Faster oxidation kinetics are determined to be present in current experiments as compared to oxidation kinetics reported in literature. The presence of nickel was confirmed to be a result of the high flow in the loop system,

while several mechanisms are proposed to account for the faster oxidation kinetics.

ACKNOWLEDGEMENTS

I would like to thank my advisor, Professor Bryan Webler, for the support and guidance he has provided throughout my project. I would also like to thank my CMU committee members Professor Chris Pistorius and Professor Tony Rollett for their critical insights into my project. Special thanks must be extended to my Rickover Fellowship mentor and external committee member, Dr. John Savchik, along with fellow external committee member Dr. Kevin Fisher.

I am grateful for the hours spent in meetings weekly by John along with Tom allowing John the time to be a wonderful mentor.

This research was performed under appointment to the Rickover Fellowship Program in Nuclear Engineering sponsored by Naval Reactors Division of the U.S. Department of Energy. I am grateful to all of the technicians and engineers who enabled my experimental exposures to occur. Both the Webb group at Bettis and Randy Catalogna were significant in allowing this work to be completed. Critical conversations were promoted by both the Webler group and the Webb group at Bettis.

I owe a great deal of emotional support to my friends and family who promoted me along the way.

I would particulary like to thank my husband, Teddy, for all of the support he has provided to me the years leading up to these studies along with during my time at CMU. Through his support through both critical discusssion about my work and helping with analysis scripts, he has been a great motivator and supporter.

Rachel E. Turfitt 2022
Pittsburgh, PA

May 2022

TABLE OF CONTENTS

Abstract . . . . . **i**

Acknowledgements . . . . . **iii**

List of Tables . . . . . **ix**

List of Figures . . . . . **x**

List of Acronyms and Symbols . . . . . **xiii**

I. Introduction and Motivation 1

1.1 Austenitic Stainless Steels 1

1.1.1 Nuclear Applications 1

1.1.2 Stress Corrosion Cracking and Corrosion Fatigue 3

II. Technical Background 4

2.1 Austenitic Stainless Steels 4

2.1.1 Microstructure 6

2.1.2 Martensite 7

2.2 Martensitic Transformations 8

2.2.1 Martensite Formation in Austenitic Stainless Steel 9

2.2.2 Deformation Induced Martensite 11

2.2.3 Stacking Fault Energy 14

2.3 Uniaxial Deformation and Strain 15

2.3.1 Plastic Strain 17

2.3.2 Axial and Lateral Strain in the Plastic Regime 17

2.4 Oxidation of Austenitic Stainless Steels 18

2.4.1 300 Series Austenitic Stainless Steels: Passive Oxide Formation 18

2.4.2 300 Series Austenitic Stainless Steels in Air Environments 19

2.4.3 300 Series Austenitic Stainless Steels in Steam Environments 20

2.4.4 300 Series Austenitic Stainless Steels in PWR Environments 20

2.5 Material Deformation and Oxidation Behavior of Austenitic Stainless Steels in High Temperature Water 24

2.5.1 Surface Finish 24

2.5.2 Plastic Strain 26

2.5.3 Near Surface Martensite 26

III. Objective and Hypotheses 29

IV. Strain in the Three Principal Directions 32

4.1 Introduction . . . 32
4.2 Principal strains during plastic deformation . . . 33
4.2.1 Isotropic materials . . . 35
4.3 Experimental methods . . . 35
4.3.1 Material . . . 35
4.3.2 Uniaxial tension . . . 36
4.4 Results and discussion . . . 37
4.5 Conclusions . . . 39
V. Characterization of Uniaxial Deformation and plastic strain . . . 41
5.1 Introduction . . . 41
5.2 Technical Approach . . . 43
5.2.1 Material . . . 43
5.2.2 Tensile Testing to Failure . . . 44
5.2.3 Digital Image Correlation . . . 44
5.2.4 Microhardness . . . 44
5.2.5 X-ray Diffraction . . . 45
5.2.6 Electron Backscatter Diffraction . . . 46
5.3 Results . . . 49
5.3.1 Tensile Testing . . . 49
5.3.2 Microhardness . . . 49
5.3.3 X-ray Diffraction . . . 50
5.3.4 Electron Backscatter Diffraction . . . 52
5.4 Discussion . . . 61
5.4.1 Mechanical Properties . . . 61
5.4.2 Hardness . . . 62
5.4.3 XRD and EBSD . . . 62
5.5 Conclusions . . . 64
VI. High Temperature Deformation Induced Martensite . . . 67
6.1 Introduction . . . 67
6.2 Experimental Procedure . . . 70
6.2.1 Material . . . 70
6.2.2 Uniaxial Tension . . . 71
6.2.3 Microstructural Characterization . . . 72
6.2.4 Electron Backscatter Diffraction . . . 72
6.3 Results . . . 73
6.3.1 Mechanical Properties . . . 73
6.3.2 Microstructure . . . 74
6.3.3 Deformation induced martensite . . . 75
6.4 Discussion . . . 78
6.4.1 Mechanical Behavior . . . 78
6.4.2 Martensite Transformation in Room Temperature Air . . . 79
6.4.3 Martensite Transformation at Elevated Temperature . . . 80
6.5 Conclusions . . . 82
VII. Effect of Surface Condition on Oxidation in Low Temperature Air 84
7.1 Introduction . . . 84
7.2 Technical Approach . . . 85
7.2.1 Material . . . 85
7.2.2 Thermogravimetric Analysis . . . 85

7.2.3 Oxide Analysis . . . 85
7.3 Results and Discussion . . . 86
7.3.1 Thermogravimetric Analysis . . . 86
7.3.2 Oxide Characterization . . . 88
7.4 Conclusions . . . 89
VIII. Effect of Material Deformation on Short Time Oxidation in High Temperature Water Environments . . . 91
8.1 Introduction . . . 91
8.2 Experimental Setup . . . 94
8.2.1 Material . . . 94
8.2.2 Deformation . . . 94
8.2.3 Exposure . . . 95
8.2.4 Characterization . . . 96
8.3 Results . . . 97
8.3.1 Effects of Plastic Strain . . . 97
8.3.2 Effects of Surface Finish . . . 105
8.4 Discussion . . . 108
8.4.1 Thermodynamically stable phases . . . 109
8.4.2 Short Time Oxidation Mechanism in a Loop Environment 112
8.4.3 Effect of material deformation . . . 118
8.4.4 Nickel Enrichment in SCC Cracks . . . 122
8.5 Conclusions . . . 123
IX. Conclusions and Future Work . . . 125
9.1 Conclusions . . . 125
9.1.1 Strain in the Three Principal Directions . . . 126
9.1.2 Characterization of Uniaxial Deformation and Strain . . . 126
9.1.3 Effect of Surface Condition on Oxidation in Low Temperature Air . . . 127
9.1.4 High Temperature Deformation-Induced Martensite . . . 127
9.1.5 Effect of Material Deformation on Short Time Oxidation in High Temperature Water Environments . . . 129
9.2 Future Work . . . 131

Bibliography . . . **133**

LIST OF TABLES

1.1 PWR design parameters [1] 3

2.1 Compositional specifications for select austenitic stainless steel grades [2]. 5

4.1 Tensile parameters for dog bone specimens pulled to failure. 36
4.2 Mean squared error for each condition plotted in Figure 4.2. 37
4.3 Value of x in Equation 4.7 calculated for each sample condition. 38

5.1 Condition and compositional specifications (wt.%) for 304 heats characterized in uniaxial tension. 43
5.2 Mechanical properties for each heat tested to failure at 21, 250, and 338 °C. 49
5.3 EBSD results after cleaning data. 58

6.1 Composition and stacking fault energy of the 304 stainless steel heats. . . 71
6.2 Test matrix for all specimens. 72
6.3 Ms temperature (°C) for each heat using the Pickering empirical formula. [3] 80

7.1 Chemistry for the 304 exposed to low temperature air. 85
7.2 Mass change for each specimen determined by TGA and pre- and post-test mass measurements with a balance. 87

8.1 Composition of the 304 stainless steel heats. 94
8.2 Plastic strain (%) induced into microstructure. 94
8.3 Surface finishes of the exposed samples. 95
8.4 Chemical composition (at%) of the outer particles and inner oxide, as determined by EDS. 101
8.5 Composition of the 304 stainless steel heats. 107

LIST OF FIGURES

1.1 Schematic of a PWR primary and secondary circuit [4]. 2

2.1 Schaeffler diagram showing phase stability based off of chromium and nickel equivalents [5]. The stability range of 301, 304, and 316 is inlaid. 6
2.2 Annealed 304 microstructure showing grain boundaries and twin boundaries, a 10% oxalic acid in water etch at 6V was used and imaged with polarized light in an optical microscope. 7
2.3 Transformation of the face centered cubic crystal structure to the hexagonal close packed structure [6]. 10
2.4 Schematic of an engineering stress versus engineering strain curve. 16
2.5 Oxide layers formed on the surface of austenitic stainless steels in high temperature water. Oxidation and reduction reactions occurring in the oxidizing system are shown along with ionic transport through the inner oxide; Cr* indicates chromium that is not transported in the oxide, remaining in its original location at oxidation. 21
2.6 Plot of the logarithm of the diffusion coefficient for chromium and carbon in FCC and BCC iron [7–9]. 27

4.1 Tensile specimen geometry. 36
4.2 Axial vs. lateral engineering strain measured by DIC for a) 6061-T6511 Al, b) Mill annealed 304, and c) cold rolled 304; relationship between axial and lateral engineering strain calculated from Equation 4.10 for an isotropic material is given as the dashed line in each plot. 37
4.3 Thickness vs. lateral true strain for a) 6061-T6511 Al, b) Mill annealed 304, and c) cold rolled 304. A linear best fit is shown for each material condition. 38

5.1 Schematic of Knoop hardness indents along the gauge length. 45
5.2 Schematic of XRD locations for (a) heat 1, (b) heat 2, and (c) heat 3. . . 46
5.3 Schematic of EBSD locations for (a) heat 1, (b) heat 2, and (c) heat 3. . 47
5.4 Hardness vs axial engineering strain for heats 1, 2, and 3 at 21, 250, and 338 °C. 50
5.5 Microstrain in austenite at each location within the gauge section for heats 1, 2, and 3 at 21 °C. 51
5.6 Phase fraction, (vol %), martensite as a function of location for the heats 1, 2, and 3 at 21 °C. 52
5.7 FSD image, phase, and local misorientation maps for heat 1 at the fracture. 53
5.8 FSD image, phase, and local misorientation maps for heat 1, 4.6 mm from the fracture. 54

5.9 FSD image, phase, and local misorientation maps for heat 1, 9.6 mm from the fracture. 55
5.10 FSD image, phase, and local misorientation maps for heat 1 in the grip region. 56
5.11 Relationship between axial engineering strain and mean local misorientation for all samples (a) and for samples without cold work (b). 59
5.12 Local misorientation (green) and engineering strain as produced during uniaxial straining. Red areas in the maps are α' martensite. 60
5.13 Local misorientation and plastic strain as produced during uniaxial straining 60
5.14 Martensite content and plastic strain as produced during uniaxial straining 61

6.1 Tensile specimen used for uniaxial straining. 71
6.2 Stress vs strain curves for all three heats at the three temperatures tested in uniaxial tension to failure. 73
6.3 Yield stress for all heats pulled to failure for each temperature. 74
6.4 Light optical microscopy for heats a) 1 and b) 2 in the annealed starting condition and c) 3 in the 20% cold rolled starting condition. The yellow arrow in c) highlights deformation created by cold rolling. 74
6.5 Total martensite volume percent, determined by EBSD phase maps, vs engineering strain in the gauge region The dashed line is the relationship between martensite and plastic strain created by Olson and Cohen (Equation 6.2) [10]. 75
6.6 EBSD phase maps of austenite (blue), ε martensite (yellow), and α' martensite (red) for plastic strain samples: 5%, 10%, 20%, 30%, 40%, 45%, 55%, and 60%. Black scale bar for each map is 100 μm. 76
6.7 Phase fraction of martensite as a function of lateral strain, measured by EBSD, for the room temperature specimens pulled to failure a) and the high temperature specimens b) pulled to failure. 77
6.8 EBSD phase maps for 338 °C cold rolled specimen. Black scale bar for each map is 100 μm. 78

7.1 TGA results for 304 at 3000 min (50 hour) exposures to synthetic air at 280, 400, 700 °C. 86
7.2 SEM image of 400 °C, 50 hour exposure using the through lens detector. 88
7.3 SEM image of a cross section through the oxide into the metal substrate. 89

8.1 Dual layer oxide morphology formed on an austenitic stainless steel in high temperature, high pressure water. 92
8.2 Schematic of the specialized loop system at NNL used to expose samples to high temperature, high pressure water. 96
8.3 Surface SEM images for (a) 10 hours, (b) 50 hours, and (c) 100 hours. . . 97
8.4 Boxplot of outer particle diameter for 10, 50, and 100 hour exposure. Individual exposures for each value of plastic strain are shown in (a) while all the plastic strain values for each time are compiled in (b) 98
8.5 Cross sections created with the PFIB and imaged using the SEM at a 52° tilt using the Everhart-Thornley detector at 5 kV and 0.17 nA for (a) 10 hours, (b) 50 hours, and (c) 100 hours. 99

8.6 Boxplots for all three exposure times with a machined surface finish showing a: all values of plastic strain and b: plastic strain condensed for each time. 100
8.7 TEM EDS of 30% plastic strain exposed for a: 10, b: 50, and c: 100 hours, and selected area diffraction patterns for d: outer particle, e: inner oxide, and f: base metal. 102
8.8 Surface after oxidation for 100 hours at (a) 8000x and (b) 25000x. Yellow dashed lines show twin boundaries and the blue dashed line is located at a grain boundary 103
8.9 Cross section of an exposed specimen using the PFIB and imaged using SEM. Embedded metallic particles in the inner oxide layer are highlighted with arrows 103
8.10 Boxplots showing the oxide penetration (inner oxide thickness) for each strain level of the polished surface finish exposed for 100 hours. 104
8.11 HAADF TEM of polished surface exposed for 100 hours. 105
8.12 Surface morphology with surface finish after 100 hour exposure for (a) 80 grit, (b) 220 grit, (c) 600 grit, (d) 800 grit, (e) 1200 grit, and (f) 40 nm. . 106
8.13 Boxplot showing the oxide penetration for each heat starting material condition (mill annealed and cold rolled) and surface finish exposed for 100 hours. 107
8.14 Mean oxide thickness plotted against mean particle size for each surface finishing; the area shaded in gray denotes the finishing particle sizes that results in consumption of the deformation layer formed during oxidation. . 108
8.15 Pourbaix diagram for iron, chromium, and nickel on a 304 SS surface. . . . 110
8.16 Pourbaix diagram for iron, chromium, and nickel on a 304 SS surface. . . . 112
8.17 Oxidation in a low flow and high flow i.e., loop environments 119

LIST OF ACRONYMS AND SYMBOLS

Acronyms

AES - Auger electron spectroscopy

BCC - body centered cubic

BCT - body centered tetragonal

BWR - boiling water

CI - confidence index

CW - cold work

DIC - digital image correlation

DIM - deformation induced martensite

EAC - environmentally assisted cracking

ECCI - electron channeling contrast imaging

EBSD - electron backscatter diffraction

EDS - energy dispersive spectroscopy

FCC - face centered cubic

FEA - finite element analysis

FSD - forescatter diode

HCP - hexagonal close packed

KAM - kernel average misorientation

LM - local misorientation

MAD - mean angular deviation

NNL - Naval Nuclear Lab

OPS - oxide polishing suspension

PFIB - plasma focused ion beam

PWR - pressurized water reactor

SCC - stress corrosion cracking

SG - steam generator

SEM - scanning electron microscopy

SFE - stacking fault energy

SIMS - secondary-ion mass spectroscopy

SS - stainless steel

TEM - transmission electron microscopy

TGA - thermogravimetric analysis

UTS - ultimate tensile strength

VASE - variable angle spectroscopic ellipsometry

WDS - wavelength dispersive spectroscopy

XRD - x-ray diffraction

Symbols

A - area

a - lattice parameter

α - martensite saturation parameter

α' - body centered cubic martensite

β - martensite saturation parameter

c - concentration

C_p - heat capacity at constant pressure

D - diffusion coefficient

δ - phase before/after reflection

Δ - delta

e - true strain

ε - engineering strain/microstrain/hexagonal close packed martensite

γ - austenite

J - flux

k_p - parabolic rate constant

k - thermal conductivity

l - length

M_f - martensite finish temperature

M_s - martensite start temperature

ν - Poisson's ratio

p - probability of a martensitic embryo

P - force

Ψ - psi

$\boldsymbol{q}$ - conductive heat flux

Q - heat source

R - production/consumption rate of c

R_p - reflection coefficient for p-polarized light

R_s - reflection coefficient for s-polarized light

ρ - density

σ - engineering stress

t - time

T - temperature

$\boldsymbol{u}$ - velocity vector of translational motion

V - volts

x - oxide thickness

CHAPTER I

Introduction and Motivation

1.1 Austenitic Stainless Steels

Austenitic stainless steels, which are classified by a face centered cubic (FCC) crystal structure, are employed in a wide range of applications from household items to components in nuclear reactors. Due to their wide range of uses, they are subject to a variety of processing procedures, environments, and temperatures. The austenitic stainless steels are desirable due to their good corrosion resistance, low cost, wide availability, good weldability, and formability [11]. Major alloying additions include 16-30% chromium and 2-20% nickel with different grades depending on alloying content of chromium and nickel, along with minor additions such as carbon and molybdenum [2]. The different grades have different stabilities; some grades are metastable where the FCC crystal structure can transform to a body centered cubic (BCC) or hexagonal close packed (HCP) martensite upon cooling or deformation [12, 13]. Prior material condition along with grade will elicit different behaviors in the same environment [14–16].

1.1.1 Nuclear Applications

Austenitic stainless steels within the nuclear industry are used in a wide number of environments including air, steam, and water. The 300 series are commonly found in both the primary and secondary side of boiling water reactors (BWR) and pressurized water reactors (PWR) where high pressures and low to moderate temperatures exist. A labeled diagram of both the primary and secondary circuit of a PWR is shown in Figure 1.1. The austenitic stainless steels are widely used in control rod containers, piping, cladding, struc-

tural components, and within the pump in PWRs [4, 17]. Entirely internal components, such as cladding and core structures are exposed to either liquid water or steam while piping components may be internally exposed to water or steam; the outside of the pipes are exposed to air.

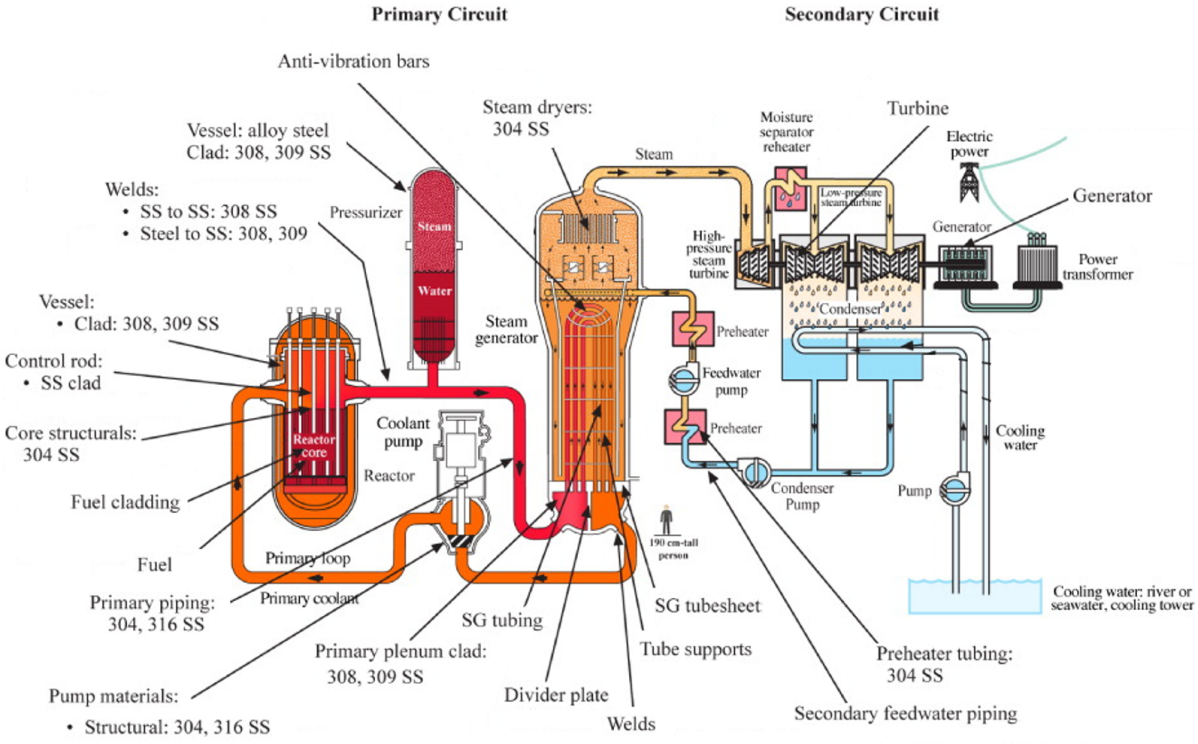

Figure 1.1: Schematic of a PWR primary and secondary circuit [4].

Design and operating conditions for a PWR are given in Table 1.1. The water in the primary circuit is maintained around 340 °C and 13.8-15.4 MPa when operating. The primary loop is often deaerated using small amounts of boric acid, lithium hydroxide, and hydrogen additions [1, 18]. Low oxygen concentration helps to minimize the susceptibility of stress corrosion cracking and corrosion fatigue.

Table 1.1: PWR design parameters [1]

Design Parameters	Range
Primary circuit	
Design pressure (MPa)	17.1
Nom. Operating Press. (MPa)	13.8-15.4
Design Temp. (°C)	343
Secondary circuit	
Design pressure (MPa)	7.1-8.2
Nom. Operating Press. (MPa)	3.9-6.9
Design Temp. (°C)	316

1.1.2 Stress Corrosion Cracking and Corrosion Fatigue

The water environment inside the PWR can promote stress corrosion cracking (SCC) and corrosion fatigue. SCC and corrosion fatigue are both types of material failure that are promoted by a corrosive environment, material condition, and stress. SCC, as the name implies, leads to cracking of the material that can cause unexpected catastrophic failure in a material at much lower stress values than would cause failure outside of a corrosive environment. Corrosion fatigue is also an environmentally driven failure mechanism that combines fatigue, or failure due to alternating stresses, with corrosion. Both SCC and corrosion fatigue cracks propagate through the material exposing new surfaces to the environment. The small volume present in the crack can have a different chemistry than the bulk due to the buildup of corrosion products that may promote further cracking. Susceptibility of a material to SCC or corrosion fatigue is related to microstructure and processing; these will be discussed in more detail in Chapter 2.

CHAPTER II

Technical Background

2.1 Austenitic Stainless Steels

Austenitic stainless steels have a primarily austenite matrix, an FCC crystal structure that is nonmagnetic, and are the most common type of stainless steel [2]. They are divided into 3 subgroups: 100 series, 200 series, and 300 series. The 100 and 200 series are general purpose, while the 300 series are tailored to more specific engineering applications through alloying element compositions. Nickel additions stabilize the austenite in the 300 series, resulting in higher production costs, and also increase corrosion resistance. The 300 series stainless steels are the most commonly used series of austenitic stainless steel [2].

Major alloying additions of the 300 series include 18-30% chromium and 6-20% nickel. A minimum of 10.5-12% chromium, a ferrite stabilizer, promotes formation of a protective chromium oxide layer on the surface providing a diffusion barrier to further oxidation, and 8-9% nickel promotes a fully austenitic structure [19]. Minor alloying elements including molybdenum and tungsten act as ferrite stabilizers, while carbon stabilizes austenite. The composition of the alloying elements result in the microstructure, mechanical properties, and corrosion resistance of the steel. The most commonly used grade of austenitic stainless steel is 304 [20].

Two other common 300 series stainless steels grades are 301 and 316. Type 301 is less expensive and less corrosion resistant than 304 due to the lower nickel content than 304 while type 316 is more expensive and more corrosion resistant than type 304 due to higher nickel content and addition of molybdenum. Alloying composition also determines the materials' susceptibility to transformation of the austenitic structure to martensite in

certain conditions. Specifications of 301, 304, and 316 are given in Table 2.1, where the numbers are given in weight %. Other specifications that can be made within a grade are allowable carbon and nitrogen concentration; common grades are L grades which specify a maximum carbon concentration of 0.03%.

Table 2.1: Compositional specifications for select austenitic stainless steel grades [2].

	301	304	316
Chromium	16.00-18.00	18.00-20.00	16.00-18.00
Nickel	6.00-8.00	8.00-12.00	10.00-14.00
Carbon	≤0.15	≤0.08	≤0.08
Manganese	≤2.00	≤2.00	≤2.00
Phosphorus	≤0.045	≤0.045	≤0.045
Sulfur	≤0.03	≤0.03	≤0.03
Silicon	≤0.75	≤0.75	≤0.75
Nitrogen	≤0.10	≤0.10	≤0.10
Molybdenum	0	0	2.00-3.00
Iron	Bal	Bal	Bal

A Schaeffler diagram used to predict stability of austenite, ferrite, and martensite based off of the chemical composition of the steel and the chromium and nickel equivalents is given in Figure 2.1. Stability regions for 301, 304, and 316 based off the compositional ranges given in Table 2.1 are inlaid. All three phases span a large range of phase stability based on the composition alone, although these steels are tailored to be austenitic, and the extremes are not expected to be present. The 301 has the smallest range of austenite stability with large regions existing in the austenite + ferrite and the austenite + martensite + ferrite. The 304 grade is intermediate to 316, which has the largest range of austenite stability. All three grades have the potential to contain ferrite and the 301 and 304 grades are more likely than the 316 grade to contain martensite.

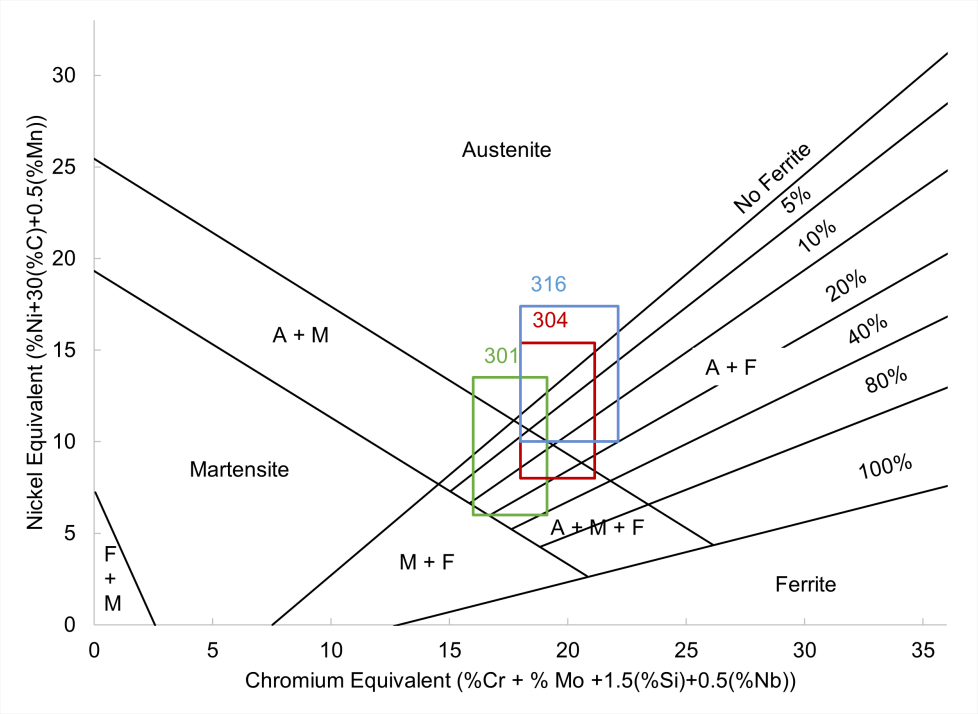

Figure 2.1: Schaeffler diagram showing phase stability based off of chromium and nickel equivalents [5]. The stability range of 301, 304, and 316 is inlaid.

2.1.1 Microstructure

The microstructure of an annealed 304 that was etched using 10% oxalic acid in water using 6V and imaged using polarized light in an optical microscope is shown in Figure 2.2. Austenitic stainless steels are commonly used in the annealed or cold worked conditions as these grades are not hardenable through heat treatments but only through cold work [2]. Grains appear as different shades of gray, and annealing twins are shown by the parallel lines that traverse some grains. Grain size is a function of the annealing and processing procedures and is controlled to reach desired mechanical properties. Precipitates, including δ ferrite, carbides, and sulfides, are often detrimental to material behavior and can form within these grades due to annealing treatments or composition variations.

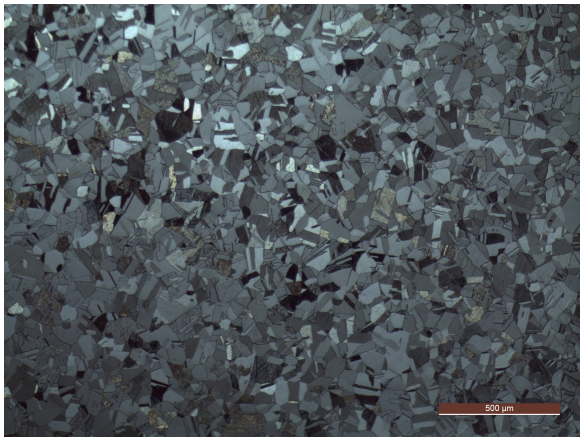

Figure 2.2: Annealed 304 microstructure showing grain boundaries and twin boundaries, a 10% oxalic acid in water etch at 6V was used and imaged with polarized light in an optical microscope.

Microstructure is also influenced by the forming and finishing procedures used to obtain the final desired shape. Components are permitted to contain a specified amount of intentionally induced or known cold work when they are put in service in a PWR environment. Deformation acts to increase the number and density of dislocations [13]. Mechanical twins, along with deformation induced martensite, can be induced into the microstructure through deformation such as cold rolling, drawing, and forming. Surface finishing procedures can create a surface deformation microstructure that can extend a few microns in depth into the surface. Both cold work and surface finishing can alter the oxidation behavior by altering the microstructure and phases present in the base material which will oxidize differently in the PWR environments [21–24].

2.1.2 Martensite

As was apparent from the Schaeffler diagram, compositional variations can result in martensite formation. Metastable grades of austenitic stainless steel, including 301, 304, 316, 321, and 347, can form martensite during cooling or deformation resulting in a BCC or HCP microstructure [25–27]. Low strain levels can promote formation of both types of martensite, while only BCC martensite is formed at higher strains [25]. Martensite grains form across austenite grains, terminating at the austenite grain boundary. This results in an increase in the grain boundary surface area. The type of martensite formed (BCC or HCP) and the extent of transformation are functions of the steel chemistry, temperature, and deformation

process [3, 28, 29]. Lower temperatures promote a higher extent of transformation [13]. Diffusion properties and maximum solubility of alloying components differ between austenite and martensite which can alter the oxidation behavior of the two phases [30–35].

2.2 Martensitic Transformations

Martensitic transformations are diffusionless transformations that involve long range cooperative shear movement of atoms less than one interatomic spacing, resulting in a change in crystal structure. A change in the shape and volume of the crystal also accompany the change in microstructure. When the transformation occurs near the surface, surface relief is provided by a change in the shape of the unconstrained surface crystal. Lattice imperfections are created to accommodate the transformation of the shape and volume change of the crystal because elastic strains are not sufficient to relax the stresses produced during the transformation. Other requirements of all martensitic transformations are a habit plane and an orientation relationship between the transformed and un-transformed microstructure. A combination of all of the features mentioned above are required to be considered a martensitic transformation [13].

During a martensitic transformation, one single phase transforms to another single phase. No long range diffusion occurs during the transformation which is evidenced by no change in chemical composition between the parent and transformed phase. Atoms are however displaced from their original position by cooperative motions to accommodate the transformation. A consequence of this cooperative motion is that martensite is not able to grow across the grain boundaries, although martensite can nucleate in multiple places inside a parent grain. The transformation can therefore result in a fine grain size [13].

Cooperative motion often results in the change in crystal shape and volume. Grains on the surface are unconstrained at the surface unlike internal grains which results in surface relief by a change in shape of the unconstrained surface. Changes to the shape and volume in internal grains are constrained by surrounding matrix; plastic deformation within the martensite is necessary to accommodate the strain. Dislocation density is higher for the martensitic transformations than is required during normal plastic deformation.

2.2.1 Martensite Formation in Austenitic Stainless Steel

Two types of martensite that can form in austenitic stainless steel are ε martensite which has a hexagonal close packed (HCP) lattice and α' martensite which has a body centered cubic (BCC) crystal structure that is ferromagnetic. The α' martensite phase takes on the cubic structure due to the low carbon content of the steel (<0.25% C), whereas steels with higher carbon content transform to martensite with a tetragonal structure to accommodate carbon in the interstitial sites [13]. In steels, carbon occupies a fraction of the interstitial sites. The position of the carbon in the crystal determines the crystal structure of the martensite. The martensite phase is harder and stronger than the parent austenite (γ) phase and provides a barrier to dislocation movement during plastic deformation. This has an effect to increase the strength of the material.

Common transformation paths from austenite to martensite have been devised. Proposed paths of transformation are:

γ austenite $\rightarrow$ ε martensite

γ austenite $\rightarrow$ ε martensite $\rightarrow$ α' martensite

γ austenite $\rightarrow$ α' martensite

Some researchers initially thought that ε martensite was an intermediate step in the γ austenite $\rightarrow$ α' martensite transformation and that α' martensite could not be formed directly from the γ austenite [36]. However, other studies have shown that γ austenite $\rightarrow$ α' martensite transformation can occur without the ε martensite phase present. The direct transformation has been studied in grains that have an orientation that suppresses the ε martensite formation [37].

Both FCC and HCP have close packed structures; the difference between FCC and HCP is the stacking order of the close packed planes. FCC has ABCABC... stacking while HCP has ABAB... stacking sequence. The FCC structure can be transformed into the HCP structure through deformation by stacking faults; shifting of every second (111) FCC plane by $(a/6)[11\bar{2}]$ will result in the transformation from FCC to HCP [13]. A low stacking fault energy promotes this transformation path. The transformation of γ austenite to ε martensite is shown in Figure 2.3. Transformation from ε martensite $\rightarrow$ α' martensite

requires a distortion on the $(0001)_{\varepsilon}$. The transformation from ε martensite to α' martensite is not well understood and requires shear deformation on two planes to transform [6].

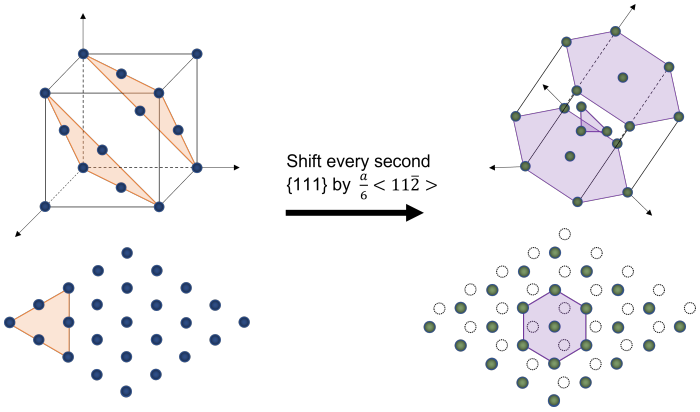

Figure 2.3: Transformation of the face centered cubic crystal structure to the hexagonal close packed structure [6].

Bain was the first to propose a transformation mechanism: γ austenite$\rightarrow$ α' martensite. The Bain model of transformation results in a body centered tetragonal (BCT) lattice. The BCC lattice can be created by expanding $(1/2)[110]_{\gamma}$ and $(1/2)[\bar{1}10]_{\gamma}$ by 12.6% while reducing $[001]_{\gamma}$ by 20.3% [38]. Inherent defects are present in the Bain model such as the differences in orientation relationships from those found experimentally. Olson and Cohen proposed a mechanism of transformation such that two consecutive shears result in the transformation [39]. A shear of $(1/8)<112>_{\gamma}$ on $\{111\}_{\gamma}$, which is produced by shifting of every second (111) FCC plane by $(a/6)[11\bar{2}]$ Shockley partial dislocations, followed by a shear of $(1/18)<112>_{\gamma}$ on $\{111\}_{\gamma}$, which is produced by shifting of every third (111) FCC plane by $(a/6)[11\bar{2}]$ Shockley partial dislocations [40]. The mechanism proposed by Olson and Cohen does not have flexibility to allow for the orientation relationships seen experimentally. A less rigidly defined transformation path is likely to occur. Plastic deformation that accompanies the FCC to BCC transformation is very large and the shear angle can reach 20°. Lattice imperfections are created to allow the transformation to proceed.

Martensitic transformations in austenitic stainless steel can be initiated several ways including refrigeration and deformation as deformation induced martensite (DIM). Martensitic transformations that are a result of refrigeration begin at M_s, the martensite start temperature is athermal: no thermal driving force is necessary to begin the transformation.

The amount of austenite that is transformed to martensite depends on the temperature to which the material is cooled. At the martensite finish temperature, M_f, the martensitic transformation will no longer proceed. Cooling below this temperature does not induce further transformation.

Empirical formulas have been derived by Eichelmann [28], Monkman [29], and Pickering [3] to determine the M_s for austenitic stainless steels as a function of composition. Using the composition of 301, 304 and 316 shown in Table 2.1 along with the empirical formulations, the M_s ranges from 0 K to above room temperature for the 300 series stainless steels. Along with composition, prior grain size can also have an effect on M_s: finer grained specimen show a depressed M_s as compared to the larger grain sized specimen [41].

$$M_{s,Eichelmann} = 1350 - 1665(C+N) - 28Si - 33Mn - 42Cr - 61Ni1001[28] \tag{2.1}$$

$$M_{s,Monkman} = 1182 - 1456(C+N) - 37Cr - 57Ni1001[29] \tag{2.2}$$

$$M_{s,Pickering} = 502 - 810C - 1230N - 13Mn - 30Ni - 12Cr - 54Cu - 46Mo1001[3] \tag{2.3}$$

2.2.2 Deformation Induced Martensite

DIM can be categorized as stress assisted martensite and strain induced martensite [42]. Stress assisted martensite occurs at lower levels of deformation and nucleates at sites already present in the material; the same sites where refrigeration induced martensite would nucleate. Strain induced martensite occurs at higher levels of deformation and forms as a result of plastically deforming the austenite phase, creating new nucleation sites. Deformation can be a result of cold working, surface preparation, cyclic stresses, static loads, and other modes of deformation. Alloying elements and material condition such as plastic strain, grain size, and grain orientation, as well as parameters of deformation such as strain rate have an effect on the extent of the martensitic transformation through cooling and deformation [43].

Plastic deformation that accompanies cold working can result in dislocation formation and glide, mechanical twinning, stacking faults, and transformation from austenite to martensite at temperatures higher than M_s [44–47]. The amounts of each formed are related to the materials composition and temperature at which the plastic deformation occurred. Many of the deformation structures that are a result of plastic deformation, particularly mechanical twins and martensite, act to impede motion of dislocations, strengthening the material.

A number of nucleation sites for the strain induced martensitic transformation have been proposed including shear band intersections [48–50], parallel shear bands [51], isolated shear bands [50, 51], intersection of grain boundaries and shear bands [51], grain boundary triple points [50, 51], twin boundaries [52], and twin intersections [53]. Shear bands can be of the form of ε martensite, mechanical twins, or dense stacking fault bundles [54].

Different characterization techniques have been used to determine the amount of martensite present in austenitic stainless steels. Methods include: Feritscope measurements, X-ray diffraction, electron backscatter diffraction, Satmagan (Saturated Magnetic Analysis) measurement, magnetic force microscopy, vibrating sample magnetometers, density measurement, magnetic balance, and quantitative optical metallography. Most studies have focused on martensitic volume determination after deformation although some recent studies have considered in-situ transmission electron microscopy (TEM) during deformation to monitor the progression of DIM.

DIM in Austenitic Stainless Steel

The volume fraction of DIM has a dependence on pre-strain, strain, strain rate, stress state, stacking fault energy, alloy composition, and temperature. Olson and Cohen studied the transformation kinetics of DIM and proposed an equation to relate the amount of α' martensite transformed to the plastic strain in the material [47]:

$$f^{\alpha'} = 1 - exp\left\{-\beta[1 - exp\left(-\alpha\varepsilon\right)]^n\right\} \tag{2.4}$$

$$\beta = \frac{\bar{\nu^{\alpha'}}\kappa}{\left(\bar{\nu^{sb}}\right)^n}p \tag{2.5}$$

Where p is the probability that a new martensitic embryo will be generated by intersecting shear bands, β is the probability of martensitic embryo formation accounting for temperature and geometry, and α is a strain dependent constant that is related to shear band formation at low strain rates. Both α and β parameters are dependent on temperature; the value of saturation of the martensite phase is determined by β, while both α and β control the rate of approach to the saturation level. β caps the upper temperature at which martensite should be able to transform at 50 °C [47].

The model predicted in Equation 6.2 has been tested extensively by a number of investigators [55, 56]. These investigators found that the true strain results in an increase in volume fraction of martensite that decreased with increasing temperature. There is a saturation of about 89 vol% martensite for temperature below -30 °C, while the maximum volume fraction martensite at higher temperatures is much lower. Martensitic transformation was found to occur over temperatures of 50 °C, which is not in agreement with the β parameter defined in Equation 2.5. Discrepancies may arise since the volume fraction of martensite in Equation 2.5 is assumed to be due to shear band intersections where other nucleation processes may exist [47].

As discussed previously, α' martensite is only one of the two types of martensite that can form upon deformation. The model predicted by Olson and Cohen ignores the possibility of formation of ε martensite. Formation of ε martensite is suggested to occur at lower strain levels, up to 15% strain, and transforms to α' martensite at higher levels of strain [25, 52, 55, 56].

Strain rate and strain mechanism also alters the martensite transformation upon deformation. Deformation induced martensite forms faster at lower strain rates and is fully suppressed at very high strain rates [55, 57, 58]. This phenomenon has been attributed

to adiabatic heating within the material at high strain rates that repress the martensitic transformation [55]. Biaxial straining increases the martensite formed compared to uniaxial straining [55].

At the lower temperature, strain induced martensite contributes to the mechanical properties resulting in the large increase in stress at lower temperatures. When the temperature is increased, strain induced martensite contributes to a lesser extent and does not contribute at high enough temperatures. The rate at which martensite transforms due to strain is also higher at lower temperatures [59]. This increases the strength of the material thereby decreasing the total elongation of the sample.

2.2.3 Stacking Fault Energy

Stacking fault energy (SFE) is the energy required for a dislocation to be broken into partial dislocations and is related to the energy required for a dislocation to cross slip from one glide plane to another. Stacking fault energy is closely linked with the deformation process the material undergoes: mechanical twinning and dislocation glide are promoted in materials with a low (<18 $\frac{mJ}{m^2}$) SFE [60], twinning occurs when the SFE is at intermediate values (18-45 $\frac{mJ}{m^2}$) [58], and dislocation glide is predominant in materials with a high SFE (>45 $\frac{mJ}{m^2}$) [58]. Formation of ε martensite from γ austenite occurs through partial dislocations. Materials with low SFE would therefore promote the formation of ε martensite.

Stacking fault energy in austenitic stainless steels as a function of alloying content can be calculated by [61]:

$$SFE(mJ/m^2) = -53 + 6.2(\%Ni) + 0.7(\%Cr) + 3.2(\%Mn) + 9.3(\%Mo) \tag{2.6}$$

Where the alloying content is in weight percent.

Martensitic transformations are long range diffusionless transformations that can occur in many alloy systems. Metastable austenite can transform to martensite in a number of ways including strain. Straining the material creates new nucleation sites, such as shear band intersections and twin boundaries, for martensite to form in the austenite lattice.

Martensite grains are smaller than the prior austenite grains, increasing the grain boundary area. Two types of martensite form from austenitic stainless steel including α' martensite (BCC) and ε martensite (HCP). Austenite can form directly to ε or α' and ε can also transform to α'. The amount of ε martensite peaks at low strain values while α' martensite continues to increase as strain increases. Mode and temperature of strain also affect transformation; slow strain rate tension straining at lower temperatures results in a higher amount of martensite. It is generally accepted that strain induced martensite will not occur at high temperatures. Strain induced martensitic transformation is a competitive mechanism, and other deformation mechanisms such as slip and twining can occur. Stacking fault energy of the material has an effect on which deformation mechanism will dominate. Lower stacking fault energy materials promote formation of strain induced martensite by increasing the nucleation sites for martensitic transformation, while higher stacking fault materials are more likely to deform by dislocation glide.

2.3 Uniaxial Deformation and Strain

The mechanical behavior of austenitic stainless steels subjected to uniaxial tensile deformation is a highly studied and well understood system. A schematic for an engineering stress-strain curve is shown in Figure 2.4. Engineering stress is defined as:

$$\sigma = \frac{P}{A_0} \tag{2.7}$$

Where σ is the engineering stress, P is the load, and A_0 is the original cross sectional area of the specimen. Engineering strain is defined as:

$$\varepsilon = \frac{\Delta l}{l_0} \tag{2.8}$$

Where ε is the axial engineering strain, Δl is the change in length of the gauge length, and l_0 is the original gauge length.

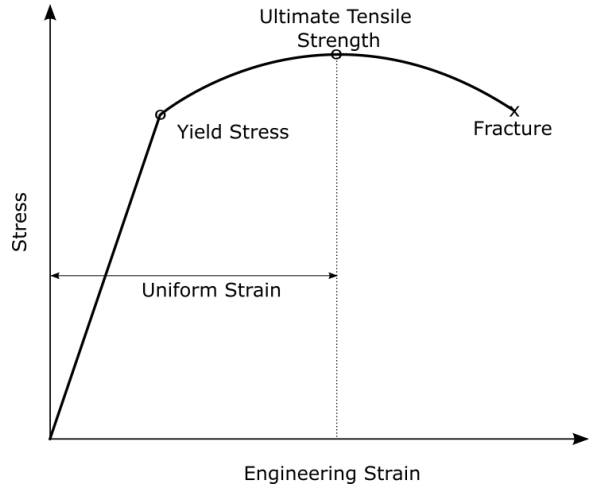

Figure 2.4: Schematic of an engineering stress versus engineering strain curve.

The material begins to deform elastically upon loading as shown by the linear portion of the curve. The relationship between axial and lateral elastic engineering strain is known as Poisson's ratio and is given as

$$\nu = \frac{\varepsilon_l}{\varepsilon_a} \tag{2.9}$$

Where ε_a is the axial engineering strain and ε_l is the lateral engineering strain. Elastic deformation is due to bond stretching and has a non-conservative volume change where the shape can be returned to the original shape by unloading.

Beyond the yield stress, the material begins to deform plastically; unloading will not return the sample to its original dimensions. The stress continues to increase with increasing strain up to the ultimate tensile strength where uniform strain ends. The deformation in this region is due to dislocations moving, along with possible phase transformation such as austenite to martensite, throughout the gauge length of the specimen [25, 27]. Phase transformations will be discussed in later sections. Dislocations increase the hardness by pinning other dislocation motion in the material, known as strain hardening.

After the ultimate tensile strength, the strain hardening is not fast enough to counter the reduction in area and necking, or an area of concentrated stress and a reduced cross sectional area, will occur and persist until fracture occurs at the neck. The total strain at

this point includes both elastic and plastic strain. Elastic strain can be removed from the sample using Young's modulus to determine the relationship between stress and strain in the elastic regime. Once elastic strain is removed, the plastic strain is known in the sample.

2.3.1 Plastic Strain

Plastic strain, or accumulated engineering strain, is often measured during deformation with the use of extensometers, strain gauges, digital image correlation (DIC), and pre- and post-test measurements. Traditional extensometers and strain gauges are equipment that are mounted to a specimen to measure change in dimensions; DIC equipment uses a camera to monitor the change in shape and position of points on the surface to monitor the strain. DIC has the benefit of analyzing the specimen multiple times with sub-micron resolution possible [62]. Plastic strain can also be quantified through other techniques after deformation is complete.

Characterization techniques used to quantify the plastic strain within the sample after deformation include hardness [63–65], electron backscattered diffraction (EBSD) [66, 67], and x-ray diffraction (XRD) [68, 69]. These techniques make it possible to determine material strain without knowing the exact prior processing or deformation of the material. This is important because plastic strain can affect how a material will behave in different environments.

Plastic Strain and Misorientation

EBSD gives orientation information that can be used to determine misorientation between a voxel and its neighboring voxels along with average misorientation information for large areas. Misorientation can be used as a proxy for plastic strain and increases with increasing dislocation densities [70]. A linear relationship is often found between misorientation and plastic strain [66, 71–73], although calibration of the misorientation and plastic strain curve is sensitive to straining technique [71, 74] and step size used in the EBSD map [75].

2.3.2 Axial and Lateral Strain in the Plastic Regime

While lateral strain is commonly used to determine Poisson's ratio in the elastic regime, few studies consider lateral strain in the plastic regime. During plastic deformation, plastic

incompressibility is present, and plastic true strain in the three principal directions sum to zero [76, 77]. The plastic incompressibility gives a relationship between axial and lateral strain during plastic deformation. In a tensile specimen of rectangular area, the ratio of lateral to axial strain will remain constant at any point outside of the neck [78, 79].

2.4 Oxidation of Austenitic Stainless Steels

The family of austenitic stainless steels often exhibit strong corrosion resistance in a variety of environments which is owed to a passive oxide film promoted by alloying with chromium [19,80]. The specific material, material condition, and environment combination play a large role in the oxidation behavior. Formation of a passive oxide layer, oxide layers formed in air, oxides formed in steam, and oxides that form in high temperature, high pressure water will be evaluated in turn. Dual oxide layers form in most environments; the stability of the austenitic stainless steels in specific environments is dependent on the protective oxide layer stability. Material conditions that can affect oxidation behavior include prior cold work, residual stress and strain, surface finish, grain size, and martensite content. The effect of each of these is complex and coupled with the environment [21, 22].

Many oxidation studies in PWR environments focus on the long term behavior of oxidation while disregarding the short term behavior [21, 22, 24]. The extent of martensite content on oxidation behavior has been studied in general, but the oxidation differences between martensite and austenite has not been studied in detail [81, 82]. Understanding the short term behavior is important for events that cause bare material to be exposed, such as crack initiation or propagation; martensite oxidation differences are important for predicting microscopic oxidation behavior in the material. Understanding the effects of the conditions and environments in which the austenitic grade of stainless steels are exposed can help to better inform decisions on which material conditions are best suited for varying applications.

2.4.1 300 Series Austenitic Stainless Steels: Passive Oxide Formation

When a bare 300 series metal surface is exposed to air or an electrolyte solution, a "native" or "passive" oxide film of only a few nanometers in thickness quickly forms on the surface

[83, 84]. A duplex oxide layer forms with a chromium-rich inner oxide between the metal and an outer iron-rich oxide phase [84,85]. A metallic nickel rich layer is often present below the chromium-rich oxide and bulk metal [84, 85].

The composition of the chromium rich oxide formed is not agreed upon and has been proposed to be chromia (Cr_2O_3) or $FeCr_2O_4$ [80]. The chromium rich layer is amorphous and provides a diffusion barrier for further oxidation [84]. The iron rich oxide layer (Fe_2O_3) does not provide protection to the metal [80]. Transport of iron from the alloy surface occurs by diffusion through the inner oxide and is required to grow the outer oxide layer. Oxygen transport through the outer oxide layer is by oxygen vacancy transport; this is the same mechanism as in the thermally grown oxide [80].

2.4.2 300 Series Austenitic Stainless Steels in Air Environments

Oxides formed at elevated temperatures in gaseous environments, also called thermally grown oxides, are different in composition and structure than the native oxide, although a dual oxide layer is also reported on thermally grown oxides at some temperatures [80]. The oxide composition and morphology are dependent on the conditions at which it is grown.

Increasing oxidation temperature results in a change in the structure and composition of the already formed native oxide layer. Oxidation between 300-600 °C results in an oxide that is composed primarily of iron oxide (Fe_2O_3) due to the fast growth kinetics of iron rich oxides along with the low diffusion of chromium at these temperatures [86, 87]. The iron oxides are more porous than the native chromium rich oxide [87]. Diffusion is much faster through the porous oxide, decreasing the protective nature of the oxide. Further increasing temperature above 700 °C results in a shift back to a chromium rich oxide [86]. The protective nature of the oxide layer is restored and a dual oxide with an iron chromium mixed spinel and iron rich outer oxide forms [80]. Manganese enrichment in the outer oxide is also reported and its presence is suggested to provide more protection than when the iron rich outer oxide does not contain manganese [88, 89]

Oxidation at temperature beyond 950 °C results in formation of a volatile chromium species and breakthrough oxidation can occur [90–92]. The deterioration of chromium oxide stability limits the environments in which the austenitic stainless steels can be used.

2.4.3 300 Series Austenitic Stainless Steels in Steam Environments

Systems that result in exposure of austenitic stainless steels to steam environments are common in industrial settings. Exposure to steam, or even small amounts of water vapor in elevated temperature air environments shifts the oxidation behavior of austenitic stainless steels from that which is seen in elevated temperature air alone, resulting in an accelerated oxidation in steam as compared to air [93–95]. Enhancement of the oxidation kinetics in steam is not well understood, although features consistent with internal oxidation mechanisms and inner oxide porosity have been reported [95].

A dual layer oxide is reported to form with an iron rich outer oxide and a chromium rich inner oxide [22, 95–97]. The inner oxide/outer oxide interface is the location of the original metal interface, and oxidation of the inner oxide proceeds by oxygen anion ingress through the inner oxide [95].

2.4.4 300 Series Austenitic Stainless Steels in PWR Environments

In the presence of high temperature water, such as that which is present in the primary coolant loop of pressurized water reactors, austenitic stainless steels form a double layer oxide with compositions similar to those formed in a steam environment. A schematic of the oxide formed along with reactions and transport processes is shown in Figure 2.5. The outer oxide layer is iron rich with Fe_3O_4 and can contain Ni in the form of $Ni_xFe_{3-x}O_4$ or $Fe(Cr,Ni)_2O_4$ particles and the inner layer is a chromium rich spinel of the form $Ni_xCr_yFe_{3-x-y}O_4$ [98–101]. The chromium rich inner layer, with a thickness of 50-100 nm, is more compact and less porous than the outer layer, which can range from 100-1500 nm in thickness [98, 102, 103]. The grain size of the inner layer is smaller than the grain size of the outer layer which consists of large, nonuniform grains. The chromium rich inner layer provides protection to the steel from further corrosion while the outer oxide layer does not provide protection to the base metal [98]. This is similar to the oxide layers formed in ambient electrolyte, through thermal oxide growth, and in steam environments. As with the oxide formed in a steam environment, the boundary between the inner and outer layer is the site of the metal surface before oxidation occurred [21, 22].

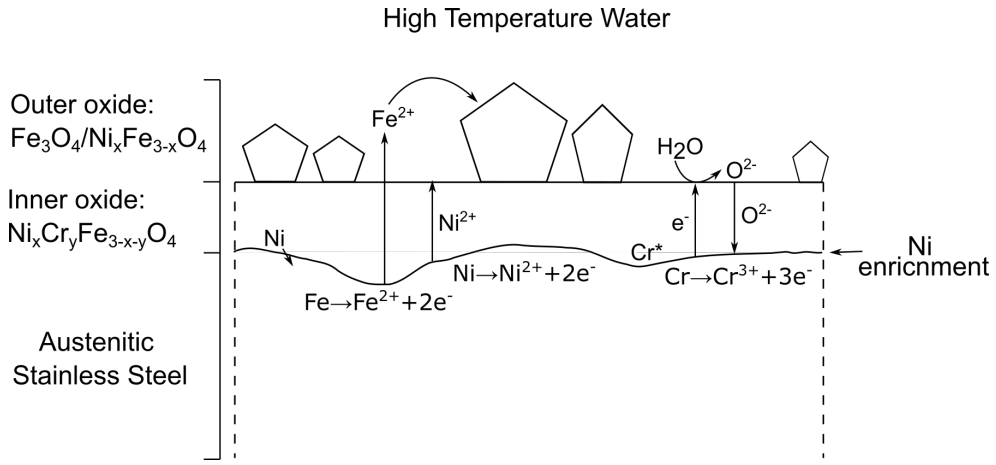

Figure 2.5: Oxide layers formed on the surface of austenitic stainless steels in high temperature water. Oxidation and reduction reactions occurring in the oxidizing system are shown along with ionic transport through the inner oxide; Cr* indicates chromium that is not transported in the oxide, remaining in its original location at oxidation.

A volume change accompanies oxidation: the inner oxide formed in the volume originally occupied by the metal is approximately half the density of the metal phase [104]. About half of the metal that originally occupied the inner oxide volume must be released into solution to overcome this volumetric constraint.

Three oxidation growth models are proposed for oxidation of austenitic stainless steel in high temperature water:

1. Solid state growth of inner oxide layer and precipitation of metal ions to form outer oxide layer [105]
2. Solid state growth of inner and outer oxide layers [104]
3. Dissolution of metal and precipitation to form both inner and outer oxide layers [106]

A parabolic rate law of oxidation kinetics of the form:

$$x = k_p t^{0.5} \tag{2.10}$$

Where x is the oxide thickness, k_p is the parabolic rate constant, and t is the time is reported to describe the kinetics of oxide growth on austenitic stainless in high temperature water [21, 99, 104, 107–109]. Parabolic growth kinetics are common for processes that are

diffusion controlled and are observed for growth of both oxide layers at longer growth times. Some authors have reported logarithmic rate law at short times before both layers have fully formed, although there is a lack of kinetic data in the literature for this behavior [105, 110, 111].

Diffusion of ions and atoms in the system determine the rate of growth. The rate of growth is proposed to be limited by:

1. Solid state diffusion through the solid oxide [105]
2. Diffusion of ions in the liquid through pores in the oxide [112]
3. Diffusion through grain boundaries [104]

Diffusivity, along with electrochemical stability, of the major alloying elements not only control the rate of oxidation, but also determine where they end up in the system during oxidation. The nobility of the major alloying elements from least to most noble is:

$$Cr < Fe < Ni \tag{2.11}$$

While the trend in diffusivity in the metallic phase for an austenitic stainless steel is as follows [113]:

$$D_{Cr} > D_{Fe} > D_{Ni} \tag{2.12}$$

Where

$$\frac{D_{Cr}}{D_{Ni}} \simeq 2.5;\ \frac{D_{Fe}}{D_{Ni}} \simeq 1.8 \tag{2.13}$$

and diffusivities of the metal ions in a spinel oxide formed in high temperature water follows [104]:

$$D_{Fe^{2+}} > D_{Ni^{2+}} >> D_{Cr^{3+}} \tag{2.14}$$

Chromium, the least noble of the alloying elements, readily oxidizes. The low diffusivity of chromium in the inner oxide results in nearly all of the oxidized chromium remaining in the inner oxide. This is shown schematically as Cr* in Figure 2.5. Iron also readily oxidizes in the environment, some is incorporated into the inner oxide. The majority of the oxidized iron diffuses through the inner oxide and is released into solution to accommodate the volume change accompanying oxidation. Iron in solution quickly reaches saturation, precipitating on the surface to form the outer oxide particles [114].

While chromium and iron readily oxidize in high temperature, high pressure water and are incorporated into the dual oxide layers, the system oxygen potential may not be high enough to oxidize the nickel. A small amount of the nickel does oxidize and is found in both the inner and outer oxide layers even though the majority of nickel remains in the metallic form. The nobility of nickel, combined with the low diffusivity of nickel in the metallic phase results in the nickel enrichment often seen at the inner oxide/metal interface.

Exposure to High Temperature Water Environments

Autoclaves are commonly used to expose samples high temperature water, i.e., PWR environments [21, 98–100]. The samples are exposed within the autoclave which is connected to a tank that holds a large volume of water and allows water samples to be collected during exposure. In line heaters, pressurizers, and ion exchange columns are used to maintain temperature, pressure, and chemistry requirements. The result of the large auxiliary systems is a large volume of water which requires very long heat up and cool down time of the system. Flow in these systems is very low and are kept at a level that allows chemistry and temperature to be controlled in the system. The long heat up times and low flow conditions make realistic short term oxidation behavior difficult to study.

Effect of material condition, such as surface finish, cold work, and martensite content, on oxidation behavior will be addressed in depth in the following sections.

2.5 Material Deformation and Oxidation Behavior of Austenitic Stainless Steels in High Temperature Water

Deformation from processing and finishing procedures is found in the starting material condition. Material deformation can include near surface deformation from finish procedures along with cold work. Austenitic stainless steel components are permitted to contain a specified amount of intentionally induced or known cold work when they are put in service in a PWR environment. Cold work accompanies processes such as forming of a part into the final shape through rolling, drawing, extruding, and surface finishing procedures on components.

Surface finishing procedures result in a near surface deformation zone, which along with cold working increases the number and densities of dislocations and twins along with other deformation microstructures, increasing fast oxidation pathways. Martensitic phase transformations may also be promoted by cold work; the difference in crystal structure between the phases alters the diffusion kinetics within the phase. Microstructural and phase transformations can both alter the oxidation behavior of austenitic stainless steels.

2.5.1 Surface Finish

Grinding, machining, and polishing are common surface finishing procedures for austenitic stainless steels; all of these procedures use mechanical means to remove material, inducing deformation on the surface and subsurface layers. Surface preparation procedures can induce high dislocation density, recrystallization, and phase transformations [115]. A nanograined layer is found near the finished surface while deformation bands are found under the surface layer of both a ground and machined surface finish; deformation induced by polishing is less severe [22, 24, 116]. Surface finishing can also lead to deformation induced martensite [24]. Starting material condition, such as cold rolling, can change the morphology of the deformation layer as well [24].

The surface finishing procedure also has an effect on the thickness of the deformed layers, while the double layer morphology remains unaffected [105, 117]. Polished surfaces have deformation layers that are 2-3x thinner than those present on ground and machined surfaces. Some studies have found a nanograin structure up to 2 μm in thickness [117] while

others have reported the fine grained layer up to approximately 5 μm [24] with the total depth of the deformed layer reaching up to 10μm [16]. The deformation structures and residual stresses that are a result of surface preparation can lead to varying susceptibilities to oxidation [116]. Studies have shown that this deformation layer along with the residual stresses can lead to a decrease in the materials corrosion resistance [16].

Grain boundary area increases from the formation of martensite and formation of the deformation induced nanograined layer. Grain boundaries, dislocations, and deformation bands all act as fast diffusion paths, compared to matrix material, for oxidation to proceed [15, 115, 117]. Deformation bands can act as fast diffusion paths for chromium resulting in localized oxidation down deformation bands [117].

More deformation is most commonly reported to increase oxidation [117], although some authors have found that more deformation results in less oxidation [22, 99, 118]. The grain boundaries were reported to be poorer at diffusing chromium leading to a thinner oxide layer [22].

Other authors have studied the effects of electropolishing on the oxidation resistance of 304L and 316L stainless steels in PWR primary water [23, 119]. A reduction in oxidation has been reported with electropolishing, as compared to machining or grinding [23, 119]. The grain size of the inner, chromium rich, oxide was also smaller. Beneficial properties of the oxide are attributed to removal of microstrains that are imparted into the material during machining. At short times, only an inner oxide layer is present; the outer oxide is not present until longer exposure times [23].

Surface deformation can have the effect of increasing or decreasing oxidation susceptibility of austenitic stainless steel in high temperature water depending on material state in addition to surface deformation and water chemistry. A fine grain layer up to a few microns in thickness, which is thicker with heavier surface deformation, forms on the deformed surface accompanied by compressive and tensile residual stresses. Deformation bands are found below the fine grained layer. The fine grained layer increases the grain boundary surface area which can act as fast diffusion paths for chromium diffusion. Most authors found that a thinner fine grained layer led to a thinner oxide layer formed in PWR water, although some authors found the opposite to be true. When a material is promoted to behave in a

passivating manner, the environment promotes better oxidation resistance.

2.5.2 Plastic Strain

Studies have shown that oxide crystals formed on cold worked material are larger than those formed on material that have not been cold worked [120]. Oxidation effects between varying surface preparations also lead to differences in stress corrosion cracking and fatigue susceptibility. Surface deformation, particularly grinding and machining, can also result in deformation induced martensite in some austenitic stainless steel grades and can extend beyond the deformed layer [16]. Deformation induced martensite will be discussed in the following section.

2.5.3 Near Surface Martensite

As discussed previously, oxidation behavior is dependent on material, environment, processing, and material conditions. Differences in alloying additions also change between heats due to the liberal requirements for different austenitic alloys. As a result, differences in austenite stability are readily apparent within a specific grade. Oxidation behavior of a metastable austenitic stainless steel with varying martensite content has not been studied in high temperature water, but studies in air and aqueous environments do exist.

As required by a martensitic transformation, the martensite formed in the austenitic stainless steel is finer grained than the parent FCC austenite matrix, since many martensite grains can be nucleated within each parent austenite grain. The finer grains result in a larger overall grain boundary surface area, which act as fast diffusion paths for chromium and oxygen within the metal.

BCC martensite has faster chromium and carbon diffusion kinetics than FCC austenite [33], although FCC iron has a larger carbon solubility than BCC iron with a maximum solubility of 2.14 wt.% and 0.022 wt.% respectively [34, 35].

The diffusivity of carbon and chromium in FCC (γ) and BCC (α) iron is plotted against the inverse of temperature in Figure 2.6 [7–9]. Lower temperature values are extrapolated from values measured at higher temperatures. Carbon diffusivity in both FCC and BCC iron is higher than the chromium diffusivity. The diffusivity of carbon is higher in BCC

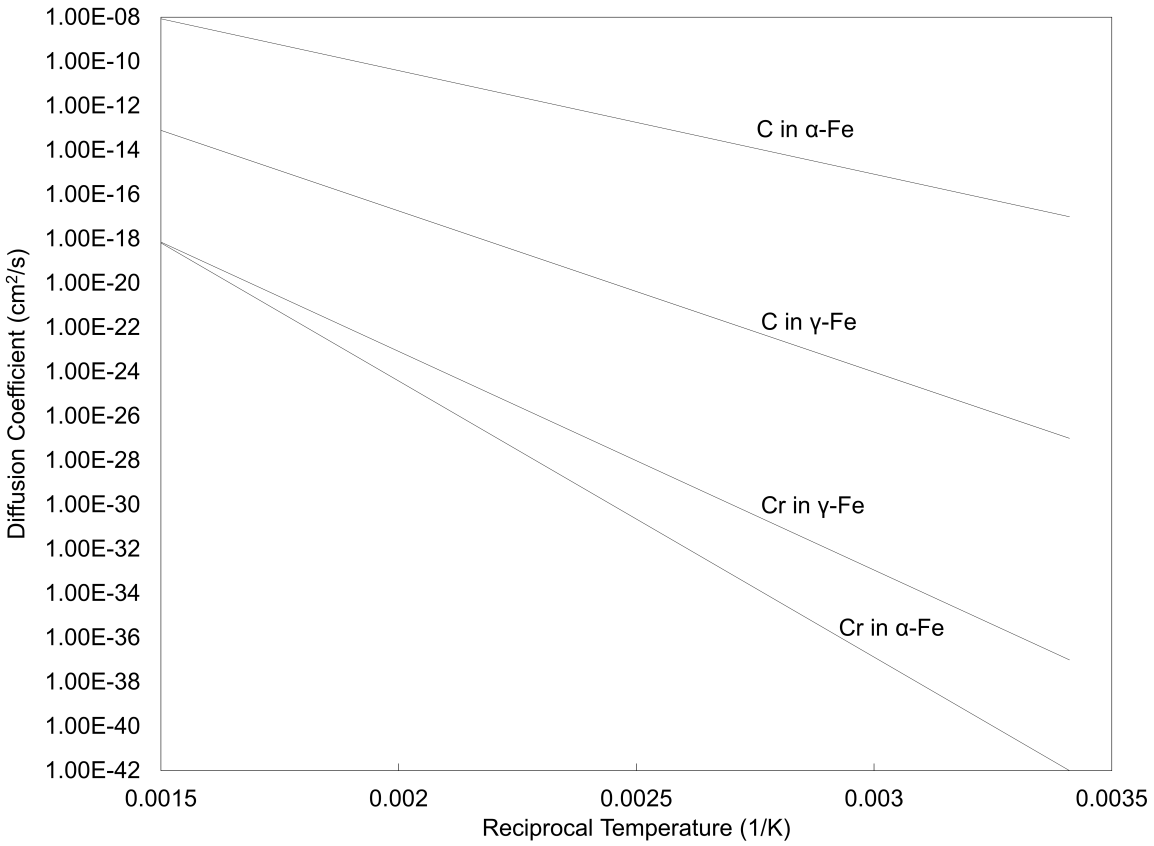

Figure 2.6: Plot of the logarithm of the diffusion coefficient for chromium and carbon in FCC and BCC iron [7–9].

iron than FCC iron, while the opposite trend is seen for diffusivity of chromium in BCC iron and FCC iron.

Although carbon diffusion is faster in BCC martensite, carbon is more soluble in FCC austenite than BCC martensite, so there is a larger driving force for precipitation of carbides in the martensite phase and at the martensite grain boundaries [34]. Sensitization, or chromium depletion, has been reported to be sensitive to martensite in the material and precipitation of carbides at the martensite grain boundaries and inside martensite lathes can promote intergranular and transgranular oxidation, respectively [82, 121]. Precipitation of carbides in the martensite phase has also been attributed to promoting further martensitic transformation [122], exacerbating the effect of martensite in the austenitic matrix.

As reported previously, increased grain boundaries from the martensite formation can act as fast chromium diffusion pathways in the material. This increase in chromium diffusion leads to a thinner, more protective oxide layer forming over the α' martensite phase resulting

in a thicker oxide over the austenite phase [81,123] in air environments. The overall effect of deformation induced martensite has been shown to decrease oxide thickness when compared to samples that contained no martensite [123].

As with oxidation of the austenitic stainless steels in various environments, the effect of deformation induced martensite on the oxidation behavior is sensitive to environment. The protective promoting nature of martensite in air environments does not extend to aqueous environments. Martensite has been shown to selectively dissolve in chloride and bromide containing solutions leading to initiation sites for fatigue cracking and SCC [68,124]. Martensite has also been shown to increase the porosity of the passive film on 304L [125].

Martensite formed at the surface of austenitic stainless steels increases the grain boundary area since martensite has smaller grains than the prior austenite grains. The increased grain boundary area can act as fast diffusion paths for elements such as chromium or oxygen. Studies on the direct effect of surface martensite on the oxidation behavior of austenitic stainless steels are not widely available, although a small number of studies have been performed. These studies can provide insight on the possible effect that surface martensite has on oxidation behavior in high temperature water. Austenite has slower carbon but faster chromium diffusion at low temperature, although a higher carbon solubility than BCC martensite. Effects of near surface martensite are highly sensitive to the environmental conditions of exposure.

CHAPTER III

Objective and Hypotheses

The overall objective of this work is to determine the effect of material condition and environment on the short term oxidation behavior of 304, a metastable grade of austenitic stainless steel.

The deformation states considered are:

1. Tensile pre-straining
2. Cold working
3. Fully annealed
4. Surface condition preparation
    (a) Ground
    (b) Polished
    (c) Machined

Environmental conditions are:

1. Synthetic air (80% nitrogen and 20% oxygen) at 280, 400, and 700 °C
2. Pressurized water at 280 °C

Both plastic strain and residual martensite, because of strain, are known to affect the oxidation behavior of these materials when subject to different environments [81, 114]. Interaction of a material and environment is a combination of both the material and the

environment of interest. The goal is to understand specific material condition and environmental couplings, which can help to better inform the general understanding, with the ultimate goal of future incorporation into computational materials models.

This work is partitioned into four components.

1. The effect of plastic strain on uniaxial tensile deformation and cold rolling on Knoop hardness and microstructure. A standardized way to accurately and quickly quantify plastic strain, imparted through various deformation mechanisms, does not exist; the aim is to determine a relationship between plastic strain and another measurable material property to be used as a proxy for plastic strain. A relationship between axial and lateral engineering strain is studied to determine the plastic axial strain in broken tensile specimens. Beyond necking, strain throughout the gauge length is not easily determined with conventional methods; relating lateral strain to axial strain provides a quick way to determine plastic strain at any point during deformation. The relationship may also be used as a quick test for mechanical anisotropy.

2. The effect of tensile temperature and starting material condition on deformation induced martensite. Predictive modelling suggests that martensite may not be able to transform via a deformation induced martensite mechanism at elevated temperature, such as that which would be present in high temperature water.

3. Observations on short time oxidation in low to moderate temperature, synthetic air. The effect of surface finish, through mechanical preparation, and martensite content is studied using thermogravimetric analysis. Characterization is performed using a scanning electron microscope after exposure. This work aims to relate subsurface deformation with oxidation kinetics; effect of martensite content on oxidation behavior is also considered.

4. The effect of plastic strain and surface finish on short time oxidation behavior is studied in pressurized water. Tensile specimens in the as machined and mechanically polished surface conditions, with a range of strain induced through uniaxial tension and cold rolling, were exposed to 280 °C water for 10, 50, and 100 hours. Surface

finish and short time oxidation was studied on a range of mechanically ground and polished specimens exposed for 100 hours. Oxide thickness was studied with SEM cross sections and composition was studied with TEM liftouts of select exposures. Subsurface deformation from surface finish was studied using electron channeling contrast imaging. Short time oxidation behavior in a loop system and a relationship between strain and oxide thickness is studied. The effect of plastic strain and near surface deformation on short term oxidation behavior can be used to inform cracking models.

The principal hypotheses of this work are as follows:

1. A relationship exists between lateral and axial engineering strain, which will be derived in a later section, within the uniform elongation regime:

$$\varepsilon_a = \left(\frac{1}{(1-|\varepsilon_l|)^{1+x}}\right) - 1$$

   Where x=1 for an isotropic material and x≠1 for an anisotropic material

2. Increasing plastic strain through uniaxial tension and cold rolling will result in thicker oxide layers for a given exposure time; oxide thickness will follow a linear relationship with uniform axial strain when exposed to high temperature, high pressure water.

3. Increasing martensite content will result in an increase of overall oxidation rate due to the increase in grain boundaries. A thicker oxide will exist over martensite, where oxide thickness is proportional to the difference in a diffusion kinetics between the austenite and martensite phases.

4. A coarser surface finish will result in a deeper deformation zone with a thicker oxide due to more fast oxidation pathways. Oxide thickness will be proportional to the finishing particle size.

CHAPTER IV

Strain in the Three Principal Directions

4.1 Introduction

Plastic anisotropy in polycrystalline metals results in differences in plastic mechanical behavior in different material loading directions and can be induced during directional solidification in casting along with heat treatment, forming, and thermo-mechanical processing. Texture, or preferred crystallographic orientation, and dislocations that are a result of the solidification and processing are common sources of anisotropy.

Anisotropy can result in changes in ductility, yield strength and work hardening; anisotropic failure can also occur where a material fails at different strains in different directions [126–128]. Ductile failure may also be promoted through plastic anisotropy at lower strain values than would otherwise be expected [129]. Variations in mechanical properties can add complexity to material behavior predictions.

Anisotropy is often measured in metal sheet as the R-value, which was developed independently and simultaneously by Krupkowski and Kawinski and Lankford, Snyder, and Bauscher [130, 131]. The R-value or Lankford coefficient for a sheet metal is defined from a tensile test as:

$$R = \frac{{e_l}^p}{{e_t}^p} \tag{4.1}$$

Where ${e_l}^p$ and ${e_t}^p$ are the lateral plastic strain and through thickness plastic strain, respectively and is used exclusively for rolled sheet metal. Similar determinations of mate-

rial anisotropy do not exist for other material starting conditions other than rolled sheet. Anisotropic behavior in bulk materials is often determined by uniaxial tension in orthogonal directions, requiring multiple specimens to be tested for each material condition. Crystal plasticity models also exist to model the behavior of known anisotropic materials, although the material's anisotropic behavior must be known prior to creating the models.

4.2 Principal strains during plastic deformation

When a tensile specimen is pulled to a value below the ultimate tensile strength (UTS), a uniform engineering strain exists along the gauge length that can be defined as:

$$\varepsilon = \frac{l_f - l_0}{l_0} \tag{4.2}$$

Where ε is the engineering strain, l_f is the final gauge length, and l_0 is the initial gauge length. Changes in the cross sectional dimension, often measured in reduction in area, can be related to true strain, given in Equation 4.2; Equation 4.3 is then used to relate true strain to engineering strain.

$$e = ln(\frac{A_0}{A}) \tag{4.3}$$

$$e = ln(1 + \varepsilon) \tag{4.4}$$

Where e is the true strain of the sample, A_0 is the original cross sectional area, and A is the final cross sectional area. During plastic deformation, the volume is conserved and the sum of the components of true strain in the three principal axes is zero, as shown in Equation 4.5 [77, 132, 133]. Also, in an isotropic material, true strain in the thickness and lateral directions are equal up to the point of necking at the UTS. Beyond the UTS, localized deformation occurs in the necked region resulting in difference in strains of the two

directions. The value along the gauge length is no longer uniform, and the highest value of strain exists in the necked region [134]. Strain outside the neck is no longer easily calculated and is often assumed to be close in value to the strain before the onset of necking [135]:

$$e_l + e_t + e_a = 0 \tag{4.5}$$

Where the subscript l, t, and a are lateral, thickness, and axial directions, respectively. For any material, a ratio between lateral and thickness strain will exist, such that Equation 4.5 can be written as:

$$e_a = -(1 + x)e_l \tag{4.6}$$

Combining Equations 4.4 and 4.6 yields the relationship between axial and lateral strain for a material with any degree of anisotropy:

$$\varepsilon_a = \frac{1}{(1 - |\varepsilon_l|)^{1+x}} - 1 \tag{4.7}$$

Where x is the ratio of the thickness strain to the lateral stain, has a minimum value of zero, and describes a material's mechanical anisotropic behavior.

In this form, the value,

$$x = \frac{1}{R} \tag{4.8}$$

So, the Lankford coefficient can be easily calculated from the lateral and axial engineering strains as

$$R = \frac{1}{-\ln(1 + \varepsilon_l)/\ln(1 + \varepsilon_a) - 1} \tag{4.9}$$

4.2.1 Isotropic materials

A special case exists for isotropic materials where the ratio between the axial and lateral strain is equal to one. When x is equal to one and the material behaves in a mechanically isotropic way, Equation 4.7 and can be rewritten as

$$\varepsilon_a = \frac{1}{(1 - |\varepsilon_l|)^2} - 1 \tag{4.10}$$

Equation 4.10 will be used as a basis to test a materials isotropic behavior. Materials that are isotropic will follow the relationship derived in Equation 4.10 while materials that have a lateral and axial engineering strain response that deviates from Equation 4.10, following Equation 4.7 with $x \neq 1$, will be assumed to be mechanically anisotropic.

4.3 Experimental methods

4.3.1 Material

A 6061-6511T aluminum alloy and 304 stainless steel (304) tensile specimen, shown in Figure 4.1, in the mill annealed and cold rolled conditions were studied. T6511 is a 6061 aluminum alloy that has been solution heat treated, stress relieved using processes such as stretching, followed by artificial aging. This temper treatment is aimed to tailor the mechanical properties of the material but can also result in mechanical anisotropy [136]. The cold rolled 304 was rolled to a 20% reduction in thickness and also has mechanically anisotropic behavior created through the rolling process, while the annealed condition 304 has mechanically isotropic behavior. The tensile axis was oriented perpendicular to the rolling direction for the cold rolled 304 sample.

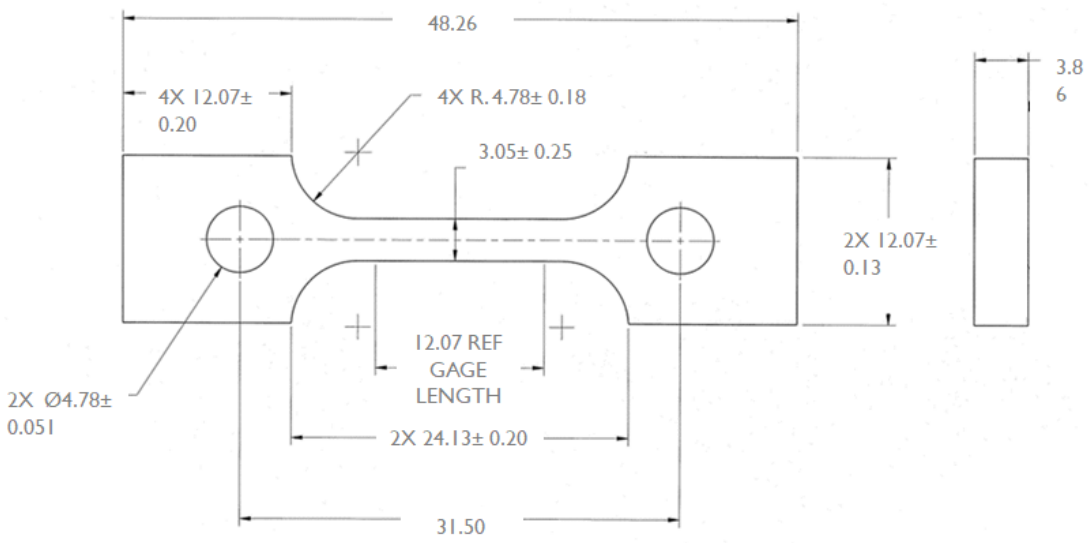

Figure 4.1: Tensile specimen geometry.

4.3.2 Uniaxial tension

Rectangular dog bone tensile specimens of as machined 6061-T6511 aluminum, cold rolled 304, and as machined 304 were pulled in uniaxial tension using DIC in room temperature air. The aluminum and cold rolled 304 display mechanical anisotropic behavior while the as machined 304 is mechanically isotropic. The aluminum was pulled to failure, the as machined 304 was strained to 60% engineering strain and the cold rolled 304 was strained to 35% engineering strain. Straining parameters to analyze each specimen material are given in Table 4.1. A speckle pattern was painted onto the sample surface for recognition points used by Instron's DIC Replay software [137]. A minimum of five virtual strain gauges of varied sizes were used for each sample throughout the gage length. The elastic strain was removed prior to determining the axial and lateral strain components.

Table 4.1: Tensile parameters for dog bone specimens pulled to failure.

Specimen Material	Displacement Rate
6061-T6511 Aluminum	0.0083 mm/s
304	0.0036 mm/s up to 4% engineering strain 0.042 mm/s to failure

4.4 Results and discussion

Lateral and axial engineering strains were measured using the DIC analysis and the three principal true strains were calculated from Equations 4.4 and 4.5. The results of the DIC experiments along with Equation 4.10 for each material condition are shown in Figure 4.2. The mill annealed 304 followed Equation 4.10 well; both the cold rolled 304 and 6061-T6511 aluminum samples deviated from Equation 4.10 at axial engineering strains greater than 15%. The deviations for each condition are reported as MSE in Table 4.2, the larger the MSE, the greater the measured data deviates from the isotropic material curve. The 6061-T6511 aluminum had the greatest deviation, followed by the cold rolled 304 with the mill annealed 304 having the smallest deviation.

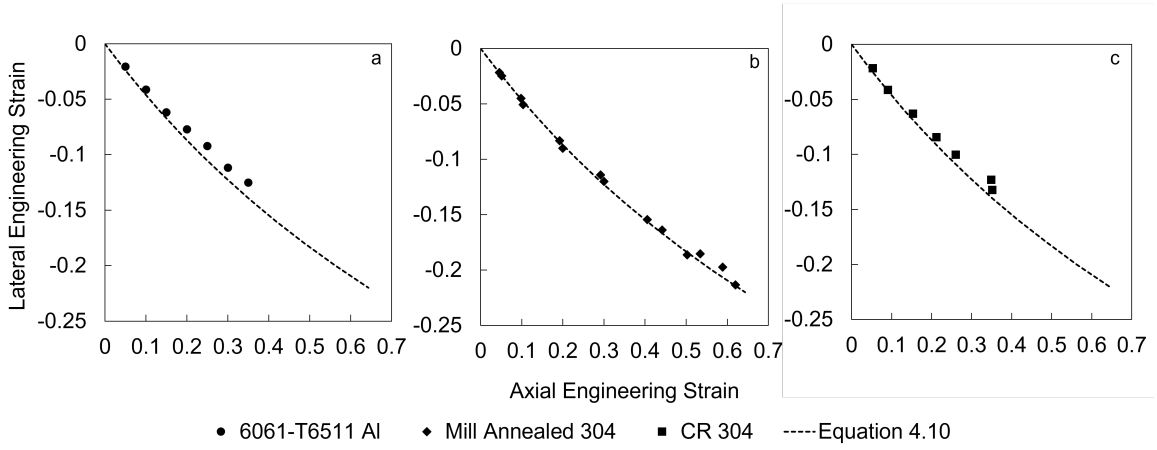

Figure 4.2: Axial vs. lateral engineering strain measured by DIC for a) 6061-T6511 Al, b) Mill annealed 304, and c) cold rolled 304; relationship between axial and lateral engineering strain calculated from Equation 4.10 for an isotropic material is given as the dashed line in each plot.

Table 4.2: Mean squared error for each condition plotted in Figure 4.2.

6061-T6511 Aluminum	Mill Annealed 304	Cold Rolled 304
$7.55x10^{-3}$	$1.97x10^{-3}$	$5.97x10^{-3}$

The value of x in Equation 4.7 was determined for each sample condition and is given in Table 4.3 by minimization of the residual sum of squares. The isotropic 304 is closest to the expected value for an isotropic material ($x = 1$), while the cold rolled 304 and aluminum alloy have higher values of x.

Table 4.3: Value of x in Equation 4.7 calculated for each sample condition.

6061-T6511 Aluminum	Mill Annealed 304	Cold Rolled 304
1.25	1.08	1.19

The relationship between lateral and thickness true strain, calculated from Equation 4.5 is plotted in Figure 4.3. The slope of the line in this plot is equal to the Lankford coefficient. For an isotropic material, the slope of the line of these two true strains should be equal to one. The slope of the mill annealed 304 is closest to one, indicating that this material is more mechanically isotropic than either the cold rolled 304 or the aluminum alloy. Both of these alloys, which deviated from the isotropic behavior given by Equation 4.10 and shown by Figure 4.2, have a slope less than one, which is expected for a mechanically anisotropic behavior. All three materials have a R^2 value of close to one indicating that a linear fit fits the data well. Equation 4.10 is only valid for isotropic materials, which is evident from the deviation of both anisotropic materials and the value of the slope of thickness vs lateral engineering strain.

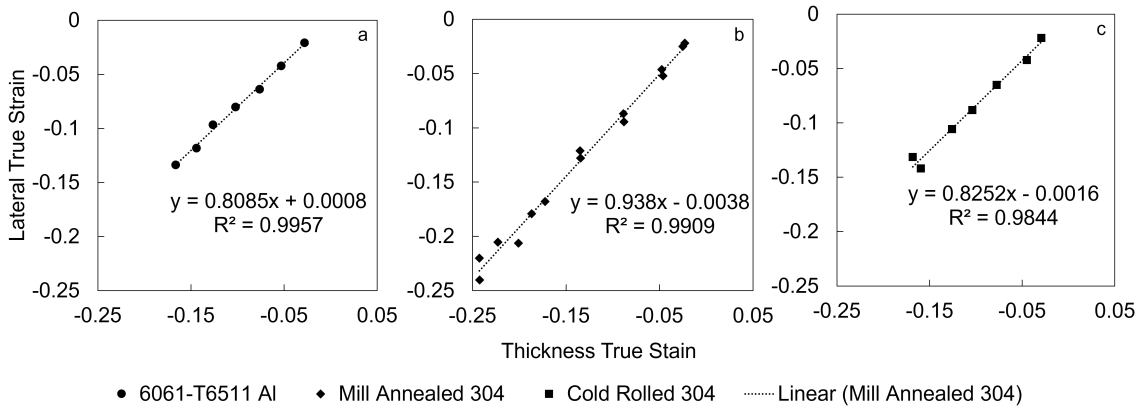

Figure 4.3: Thickness vs. lateral true strain for a) 6061-T6511 Al, b) Mill annealed 304, and c) cold rolled 304. A linear best fit is shown for each material condition.

The slope of the plots is also equal to the Lankford coefficient for sheet materials. The value of Lankford coefficients reported in literature are specific to the material and exact processing procedures. Values for 304 are reported around 1 with a range of 0.8 - 1.2, and

6061-T6511 values are anisotropic with a range of 0.6 - 0.8 [138, 139]. While the Lankford coefficient determined here is within values reported in literature, the major use is to show that the cold rolled 304 and aluminum behaved in an anisotropic way. Quantification of anisotropy is not considered here.

Virtual strain gages located at various locations within the gage outside of the neck also show that the strain outside the neck is not uniform, as is often assumed due to lack of experimental data. Strain outside the necked region after necking can be calculated for isotropic materials using Equation 4.10 for isotropic materials.

4.5 Conclusions

A relationship between lateral and axial engineering strain during uniform elongation has been derived in Equation 4.7. and verified with an isotropic material. The relationship was developed using the equation relating true strain to engineering strain, along with the notion of plastic strain incompressibility. DIC measurements to specified strain levels were used to verify the relationship. The mill annealed samples were modeled quite well with x=1 for an isotropic material and the cold worked samples were modeled with x≠1, as expected for an anisotropic material.

DIC has shown to be a quick, effective way to quickly determine whether a material displays mechanical anisotropy. Two known anisotropic metals, 6061-T6511 aluminum and cold rolled 304 stainless steel, deviated from the derived relationship for isotropic materials at high values of axial engineering strain. Mechanical behavior and plastic strain due to deformation of an anisotropic material is harder to predict than that of an isotropic material. Simple relationships between deformation induced martensite and plastic strain, as will be presented in the following chapters will be complicated by a material's mechanical anisotropy.

Calculation of the third principal engineering strain is possible from DIC and gives deviation of the thickness and lateral directions from an isotropic material.

Quantification of strain using DIC has not been completed but would be possible to determine using this setup. Equation 4.10 can be used to estimate the strain outside the necked region after necking has occurred as well, since the value of strain is not uniform

throughout the gage length. Quantification of residual strain within the gage length after failure will be completed in future sections.

CHAPTER V

Characterization of Uniaxial Deformation and plastic strain

5.1 Introduction

The 304 grade stainless steel is an extensively used material in the primary loop due to its corrosion resistance, low cost, and excellent formability [11]. Forming processes often result in cold work, residual stress and strain, and phase changes, which may affect oxidation behavior in different environments. Oxidation kinetics of austenitic stainless steels in PWR conditions change as starting material changes: as cold work and residual stress increase, the oxidation kinetics in the PWR primary water increases [14]. There are a number of different cold working techniques; this work will focus on cold rolling and uniaxial tensile straining.

A standardized way to represent cold work in a material does not exist; when cold rolling is considered, the percent cold work is the percent reduction in original thickness. In tensile cold working, the percent cold work is equivalent to the percent elongation. Due to these differences in definitions, it is possible to have an excess of 100% cold work imparted by tension, but not by cold rolling. Measures such as dislocation density can be used to quantify cold work, although large scale quantification of dislocation density is often not practical. Standardizing the effect of these cold working techniques, by using an easy to measure metric such as plastic strain, allows a direct comparison of material strain state between these two processing techniques.

A number of analytical techniques are used to measure plastic strain in a material. Hardness can be used as a proxy to plastic strain up to about 30% strain [140, 141]. Above 30% strain, further deformation can result in the formation of deformation twins and strain

induced martensite [140, 141]. Both twins and martensite result in a hardness value that predicts a lower value of strain in the material than is present, making hardness as a proxy for plastic strain very limiting.

Other techniques such as XRD and EBSD can be used to determine plastic strain present in a material along with phases present. Residual stress in a material has components of both elastic and plastic plastic strains, which can both be determined by XRD. Broadening of diffraction peaks can be used to estimate local plastic strain, also referred to as microstrain, while peak location can be used to determine elastic strain along with phases present in the material [142, 143]. Error in peak broadening calculations makes obtaining quantitative information not possible through XRD.

plastic strain can determined using EBSD by using misorientation as a proxy for plastic strain. Misorientation between points can be determined by collecting backscattered electrons and analyzing the Kikuchi bands using computer algorithms to assign lattice group and orientation at each point scanned. The misorientation can then be related to the strain, although this technique is sensitive to deformation mechanism and microscope parameters [142]. Other information, such as phases and grain orientation, can be determined from EBSD as well.

As discussed in the technical background, beyond the UTS, localized deformation occurs in the necked region. The value of strain along the gauge length is no longer uniform, and the highest value of strain exists in the necked region [134]. Without using strain gauges at multiple places along the gauge length or digital image correlation (DIC), the strain within the gauge is no longer easily calculated. The value of strain outside the necked region is usually still assumed to be uniform.

The aim of this work is to create a relationship between strain, imparted through cold rolling and uniaxial tensile straining with parameters measured by hardness, XRD, and EBSD for 304 SS.

5.2 Technical Approach

5.2.1 Material

Three heats of 304 SS were investigated in this work. One flat, pin loaded tensile specimen, shown schematically in Figure 4.1, was tested from each heat. Chemical composition of the three heats is shown in Table 5.1. Heat 1 has low sulfur content, while heats 2 and 3 have high sulfur levels. Other alloying additions are similar between the three heats except heat 1, which has a higher nitrogen content than the other two heats. Differences in chemistry are not expected to have a significant influence on the mechanical properties of the material, although chemistry differences may influence oxidation kinetics. All three heats lie on the boundary between austenite with no ferrite and austenite with 5% ferrite on the Schaeffler Diagram in Figure 2.1. The average grain size of each heat was determined using the three concentric circle method, outlined in the ASTM E112 standard, on optical micrographs of each heat [144]. Average grain size of heat 1, 170 μm, is slightly larger than that for heat 2, 130 μm, and heat 3, 120 μm, and small amounts of δ ferrite were present in every heat. Heat 1 and 2 have a mill annealed starting material condition and heat 3 was tested in the mill annealed and cold rolled to 20% reduction in thickness prior to tensile testing. Both cold work and temperature are known to influence mechanical properties and are expected to influence strain measurements performed in this study as well.

Table 5.1: Condition and compositional specifications (wt.%) for 304 heats characterized in uniaxial tension.

Heat	Condition	C	Mn	P	S	Si	Cr	Ni	Mo	N	Cu
1	Mill annealed	0.042	1.70	0.026	0.006	0.045	18.39	8.72	0.26	0.07	0.17
2	Mill annealed	0.040	1.46	0.002	0.015	0.045	18.39	9.13	0.26	0.03	0.10
3	Cold rolled	0.040	1.45	0.021	0.016	0.045	18.36	9.28	0.26	0.03	0.10

5.2.2 Tensile Testing to Failure

One dog bone sample of heat 1 and 2 in the mill annealed condition and heat 3 in the 20% cold rolled condition were tested in uniaxial tension to failure in air at 21, 250, and 338 °C at a rate of 0.0036 mm/s up to 4% strain. After 4% strain, the rate was increased to 0.042 mm/s until failure. Straining to failure was completed by the Naval Nuclear Laboratory. Mechanical properties including yield strength and ultimate tensile strength were determined from the stress strain curve, while total elongation and reduction in area were determined by measuring the sample before and after the test was completed.

5.2.3 Digital Image Correlation

Samples of heat 3 in the mill annealed condition were pulled in uniaxial tension to target values of engineering strain, up to 60%, in room temperature air (21 °C). A constant displacement rate of 0.0036 mm/s was used up to 4% strain, after which the rate was increased to 0.042 mm/s to the final desired strain level before unloading to zero load. A speckle pattern was painted onto the sample surface for recognition points used by Instron's DIC Replay software [137]. All DIC was completed by the Naval Nuclear Laboratory. Eight strain levels were obtained and a minimum of five virtual strain gauges of random sizes were used per sample at various places throughout the gauge length. The elastic strain was removed from each sample prior to determining the axial and lateral strain components.

5.2.4 Microhardness

Microhardness was measured using 500g Knoop indenter along the gauge length from the pin grips to the fracture on all samples pulled to failure. Half of the thickness was removed through mechanical grinding, and the surface was mechanically polished prior to microhardness measurements. Two rows of microhardness measurements were completed along the centerline of the gauge length, as shown in Figure 5.1. Sample preparation and hardness measurements were performed by the Naval Nuclear Laboratory with hardness locations specified to the Naval Nuclear Laboratory . lmageJ was used to determine the width at each measurement as well as the distance from the measurement to the fracture surface [145].

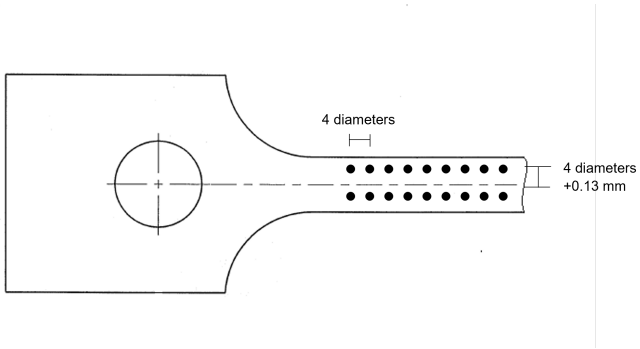

Figure 5.1: Schematic of Knoop hardness indents along the gauge length.

Lateral engineering strain at each indent was determined by dividing the change in width by the initial width of the specimen. Axial engineering strain was calculated from the axial vs. lateral strain relationship developed for isotropic materials in Equation 4.10. The relationship was only used at hardness locations that were greater than one fillet radius from the fillet. Strain values of up to 60% axial engineering strain were considered since the relationship is only valid up until the onset of necking.

5.2.5 X-ray Diffraction

Tensile samples pulled to failure at 21 °C were analyzed using XRD; the samples were repolished after hardness testing to remove all deformation induced by hardness testing. Sample preparation and XRD was completed by the Naval Nuclear Laboratory with provided parameters. Optical micrographs showing the locations of XRD analysis are shown in Figure 5.2, where location 1 is closest to the fracture surface and location 10 is furthest from the fracture surface on the gauge length. Location 10 is at a distance no less than one radius away from the fillet. Three locations in the grip region were also analyzed using XRD to provide a baseline.

Figure 5.2: Schematic of XRD locations for (a) heat 1, (b) heat 2, and (c) heat 3.

XRD was performed with a Bruker-AXS D8 Discover diffractometer using a Co Ka microfocus X-ray tube; four frames were collected at 54, 74, 94, and 114° 2θ. Diffraction patterns were analyzed using MDI, Inc's JADE Pro software [146]. Phases present were identified by comparing diffraction patterns to reference patterns in the ICDD PDG4+ 2020 database.

Microstrain is calculated by peak broadening through the Williamson-Hall analysis:

$$B(2\theta) = 4\varepsilon\frac{\sin(\theta)}{\cos(\theta)} \tag{5.1}$$

Where B is the peak width, θ is the diffraction angle, and ε is the microstrain. Microstrain is quantified by the root mean square of lattice parameter variation.

5.2.6 Electron Backscatter Diffraction

Electron backscatter diffraction was performed by the Naval Nuclear Laboratory using the Hitachi SU21 3 Field Emission Gun SEM with an Oxford detector for the 21 °C samples pulled to failure and a Thermo-Fisher Scientific Apreo S Field Emission Gun SEM with an EDAX detector was used for the high temperature samples pulled to failure and the DIC

samples. All maps were collected with Oxford Instruments Aztec 4.2 software [147]. Maps were collected on 300 μm x 300 μm areas using a step size of 0.5 μm at locations shown in Figure 5.3; the map closest to the grip section was located no closer than one radius from the fillet.

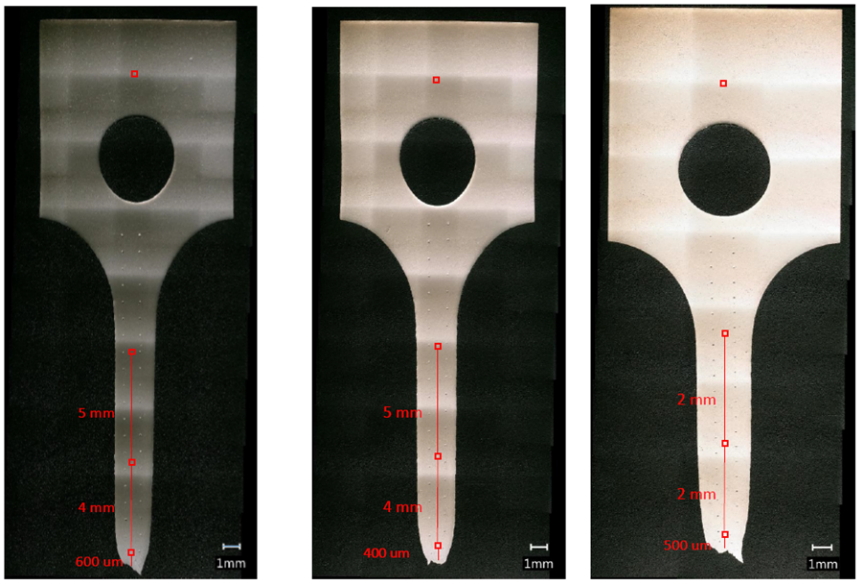

Figure 5.3: Schematic of EBSD locations for (a) heat 1, (b) heat 2, and (c) heat 3.

Channel 5 was used to analyze the maps [148]. All EBSD maps were cleaned according to the noise reduction parameters: wild spikes were eliminated and a standard, iterative, extrapolation of the zero solutions was completed with five neighbors until a minimum of zero solutions was achieved [148]. The mean angular deviation and confidence index were used to determine the quality of the EBSD maps and phase and mean local misorientation were determined for each map.

Mean Angular Deviation/Confidence Index

The two microscopes used for the EBSD analysis use different parameters to assign map quality by likelihood of a correct index. The Oxford Instruments detector determined the quality of the maps after cleaning by a mean angular deviation (MAD). MAD is a number that relates how well the Kikuchi band matches the set of simulated Kikuchi band patterns. The smaller the MAD number, the better the fit. A MAD of less than 1 is acceptable for many systems.

The EDAX detector uses the confidence index (CI), which is a voting based system which votes on the likelihood of a map with the best solution minus the votes that were assigned to the second best solution. A CI of greater than 0.1 means that the solution is likely to be the correct solution. A low confidence index can be a result of high strain or too small of crystallite size, resulting in overlap of patterns.

Phase

Phase maps were created and phase fractions determined by considering both austenite and BCC martensite phases for the samples pulled to failure and austenite, BCC martensite, and HCP martensite for the DIC samples. An input of which phases to consider was entered into the software during the scan to allow indexing and phase identification to run concurrently with scanning.

Local Misorientation

Local misorientation (LM) is a component that calculates the average misorientation between every pixel and its neighboring pixels. LM is a Kernel Average Misorientation, which is defined as:

$$KAM_{i,j} = \frac{1}{|N(i,j))|} \sum_{(k,l) \in N(i,j)))} \omega(o_{i,j}, o_{k,l}) \tag{5.2}$$

Where $|N(i,j)|$ are the neighboring pixels, which is a user defined parameter, and $\omega(o_{i,j}, o_{k,l})$ is the amount of disorientation from the pixel of interest's orientation $o_{i,j}$ and the orientation of neighboring pixels $o_{k,l}$ [149].

LM for each phase was determined with a minimum of 0 and a maximum of 10; values with an orientation above 10 are discarded to exclude grain boundaries from the local misorientation calculations. A filter size of a 3x3 grid was used as the neighboring pixels for the calculation. The value of mean local misorientation is an average of all local misorientation values for all points in the map that did not have a zero solution.

5.3 Results

5.3.1 Tensile Testing

Mechanical properties including yield strength, ultimate tensile strength, total elongation, and reduction in area were measured or calculated from the tensile experiments of the samples pulled to failure and are shown in Table 5.2. The 0.2% yield strength, UTS, total elongation, and reduction in area decreased with increasing temperature except for samples from heat 1 where the reduction in area increased from 21 to 250 °C with a slight decrease in reduction in area from 250 to 338 °C. Heat 3 had a higher 0.2% yield strength and UTS than the other two heats for each temperature tested and started with lower total elongation and reduction in area. With the exception of the increase in reduction in area of heat 1 with increasing temperature, the mechanical properties for heats 1 and 2 are similar.

Table 5.2: Mechanical properties for each heat tested to failure at 21, 250, and 338 °C.

Heat	Temperature (°C)	0.2% yield (MPa)	UTS (MPa)	Total Elongation (%)	Reduction in Area (%)
1	21	242.7	604.7	97.8	84.4
	250	157.9	428.9	63.8	88.9
	338	149.6	430.9	63.7	87.5
2	21	246.8	595.7	93.2	84.1
	250	159.3	410.2	56.2	77.4
	338	142.7	399.9	53.3	69.7
3	21	671.5	825.3	50.5	69.9
	250	590.9	650.2	19.1	52.4
	338	546.8	635.7	20.9	48.0

5.3.2 Microhardness

Hardness values in the gauge section are plotted against the axial engineering strain, calculated from Equation 4.10, for each heat in Figure 5.4. With the exception of the cold worked starting condition at high temperatures, the minimum value of axial engineering

strain was about 30% for all points.

The data was separated into four subsets: low temperature with and without cold work and high temperature with and without cold work. Low temperature, 21 °C, resulted in higher hardness values for the same material heats with cold worked samples having higher hardness and lower strain values than the materials that were in the mill annealed condition. The same relationship holds true for higher temperatures: cold worked samples have higher hardness at lower strains than the mill annealed samples.

There is little difference in the hardness and strain relationship between samples tested at the two higher temperatures. The higher temperature tests resulted in lower engineering strain and hardness than the low temperature tests. No clear relationship between strain and hardness is evident for any of the samples tested.

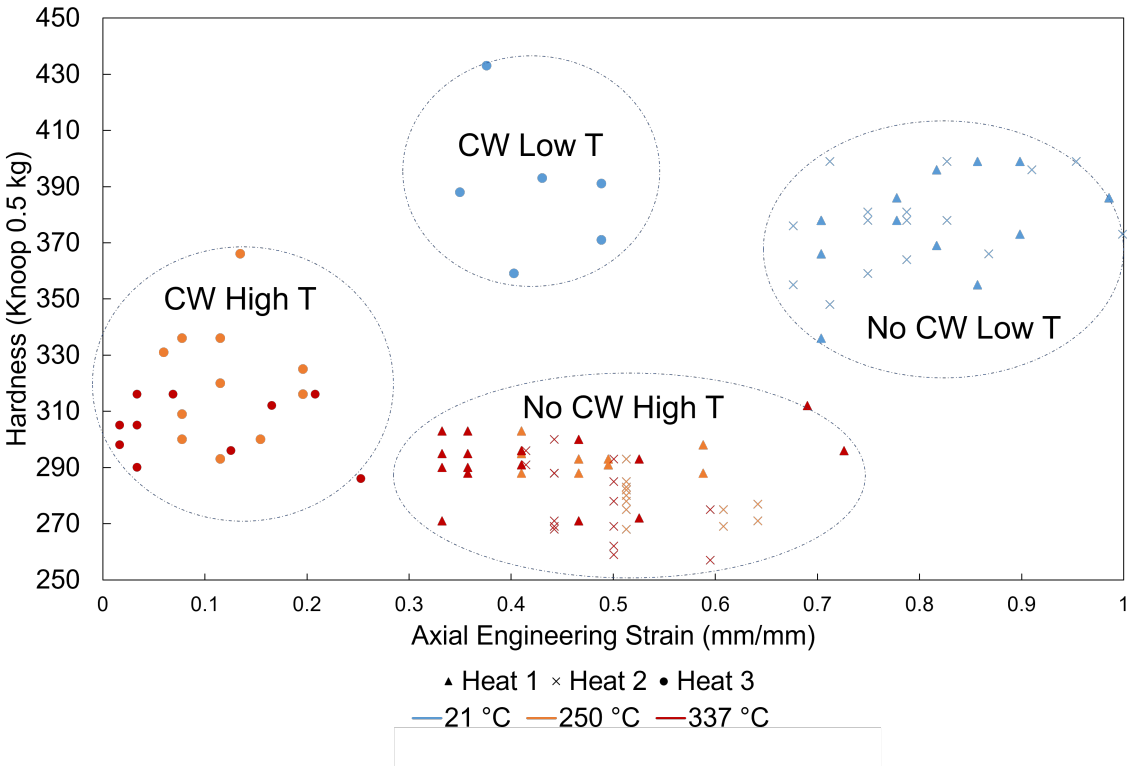

Figure 5.4: Hardness vs axial engineering strain for heats 1, 2, and 3 at 21, 250, and 338 °C.

5.3.3 X-ray Diffraction

The average percent microstrain of austenite in the 21 °C sample pulled to failure, as a function of location, is shown in Figure 5.5. There is a general trend of the microstrain

decreasing when moving away from the fracture surface on the gauge length. The microstrain drops to nearly 0% in the grip sections of both heats 1 and 2 but only to about 0.25% in heat 3. This is consistent with the mill annealed microstructure found in heats 1 and 2 and the cold work present in 3, as the grip region is not expected to deform during tensile pulling.

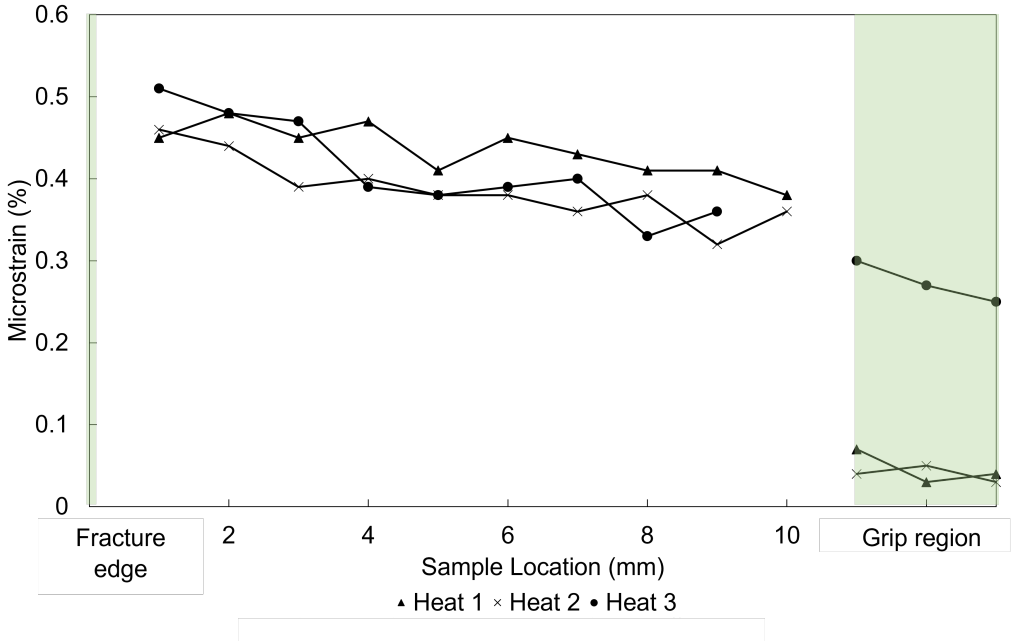

Figure 5.5: Microstrain in austenite at each location within the gauge section for heats 1, 2, and 3 at 21 °C.

The phase fraction, in volume percent, of transformed martensite at each location for the 21 °C samples pulled to failure is shown in Figure 5.6. The phase fraction of martensite is highest near the fracture surface where the microstrain values are the highest and decreases along the entire gauge length for heats 1 and 2. The phase fraction of martensite in heat 3 decreases when moving away from the fracture surface before increasing again; martensite was also detected in the grip region of heat 3 but not detected in the grip region of heat 1 or 2.

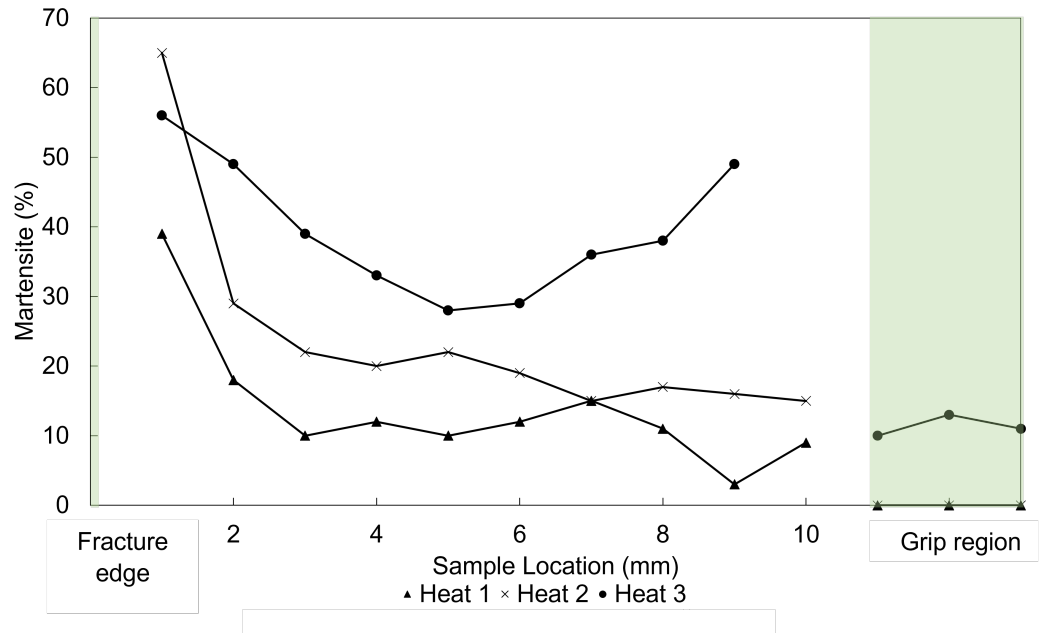

Figure 5.6: Phase fraction, (vol %), martensite as a function of location for the heats 1, 2, and 3 at 21 °C.

5.3.4 Electron Backscatter Diffraction

Specimens Pulled to Failure

The forescatter diode (FSD) image, phase map, and local misorientation for heat 1 strained to failure at 21 °C at the fracture, two other locations in the gauge length, and in the grip region are shown in Figures 5.7, 5.8-5.9, and 5.10, respectively. In the FSD image near the fracture, there is banding evident in the microstructure. This banding correlates with areas of higher local misorientation, as shown in green in the local misorientation map. There is also martensite that is detected at this point in the sample, which is colored blue in the phase map.

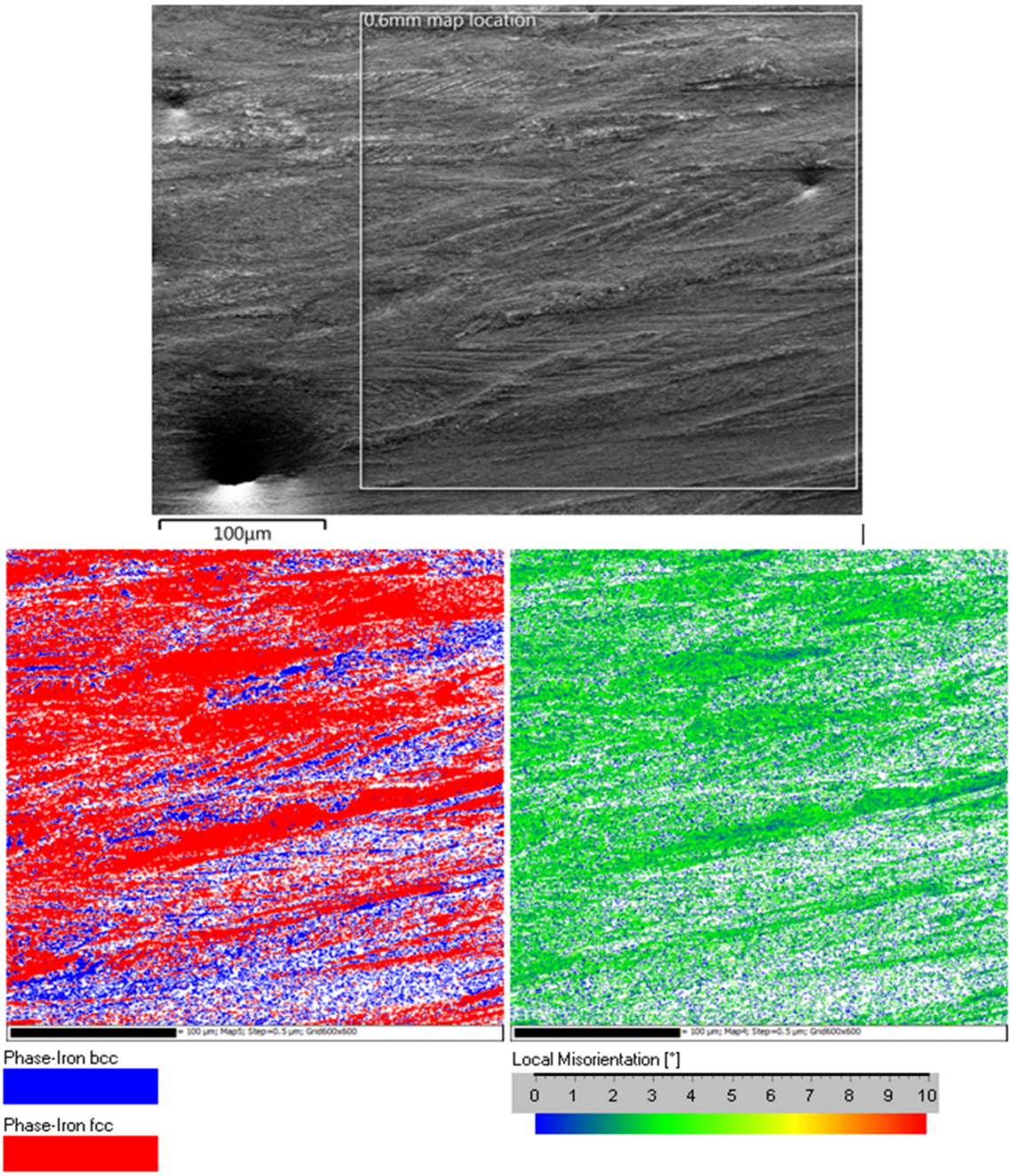

Figure 5.7: FSD image, phase, and local misorientation maps for heat 1 at the fracture.

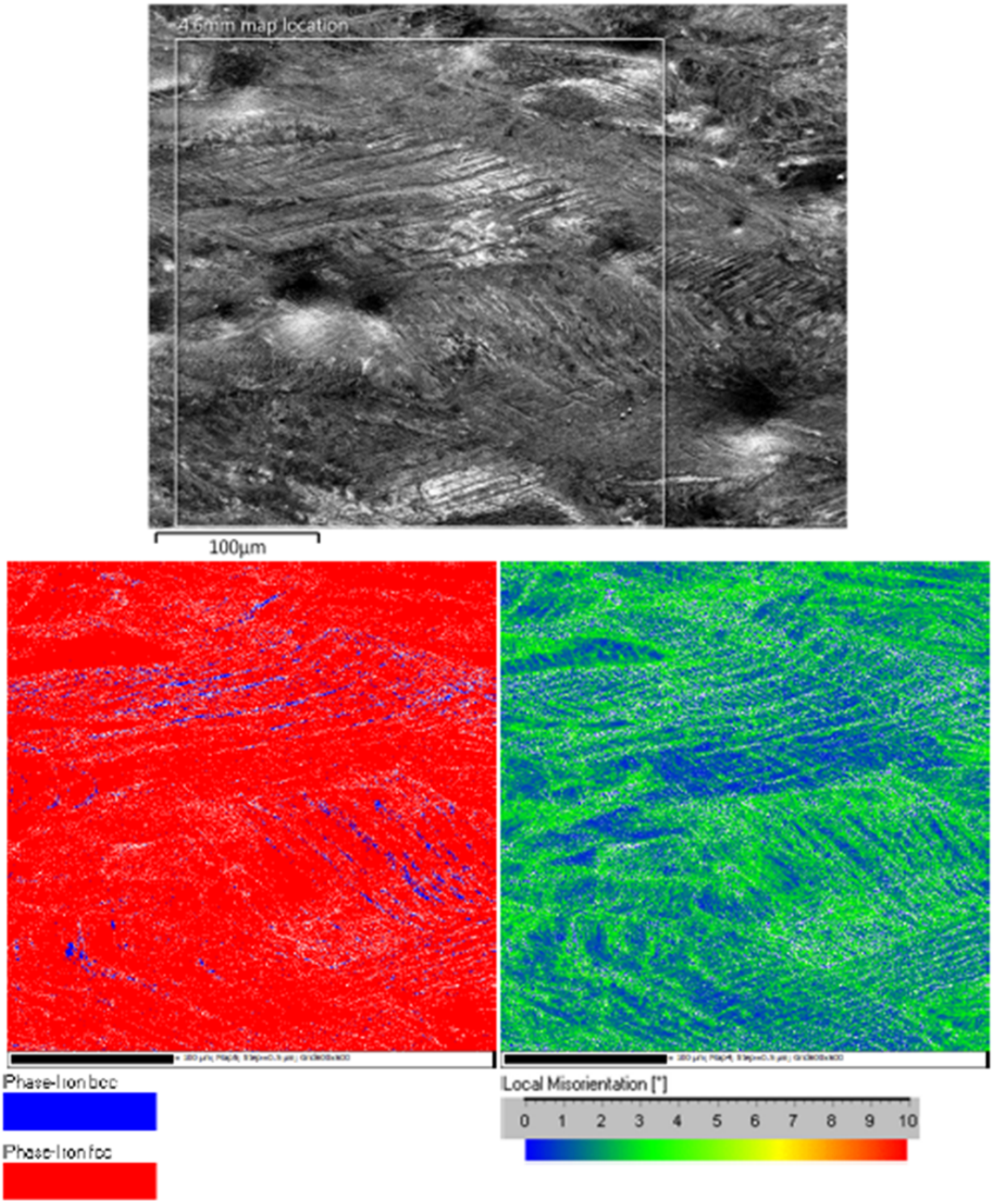

Figure 5.8: FSD image, phase, and local misorientation maps for heat 1, 4.6 mm from the fracture.

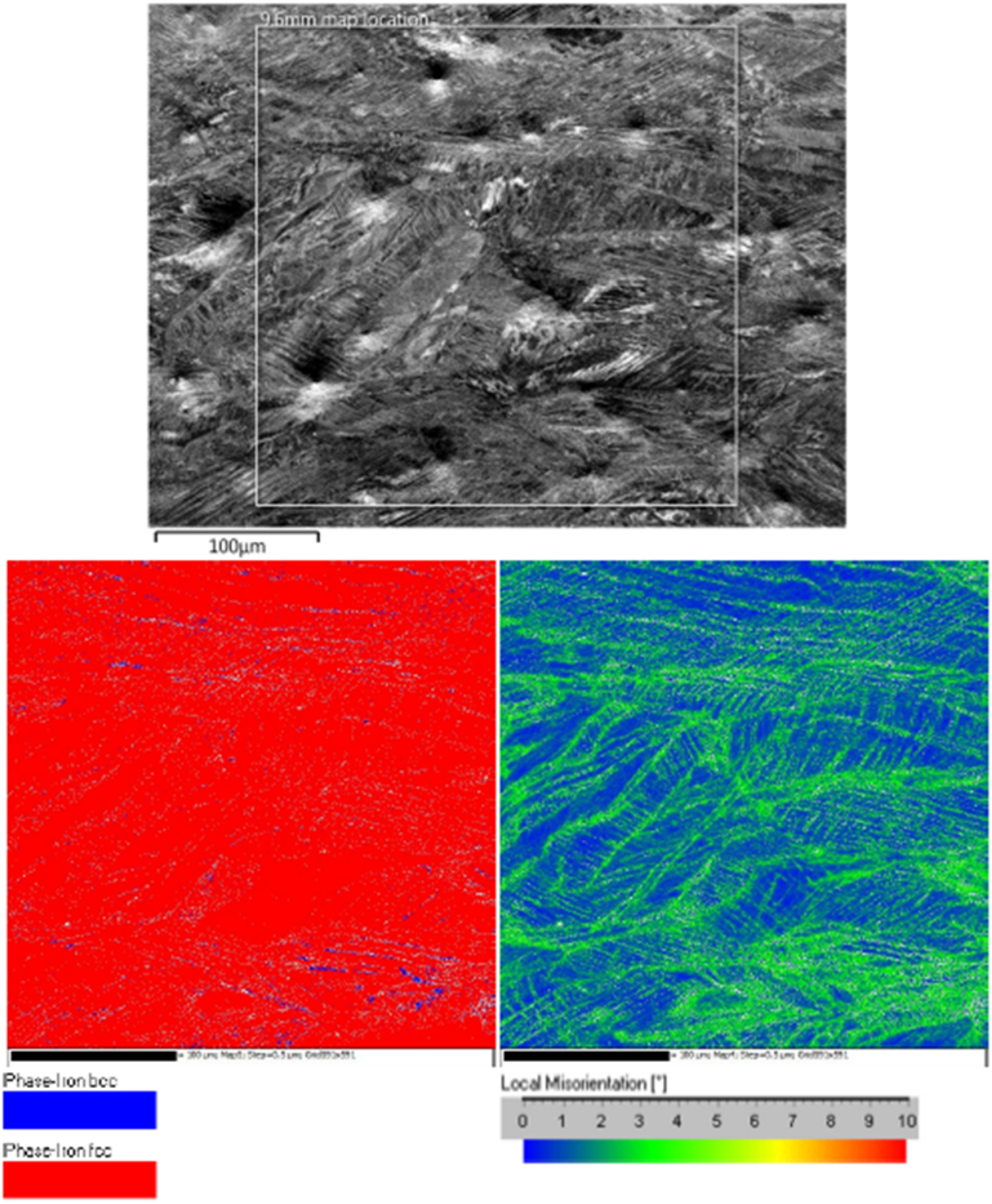

Figure 5.9: FSD image, phase, and local misorientation maps for heat 1, 9.6 mm from the fracture.

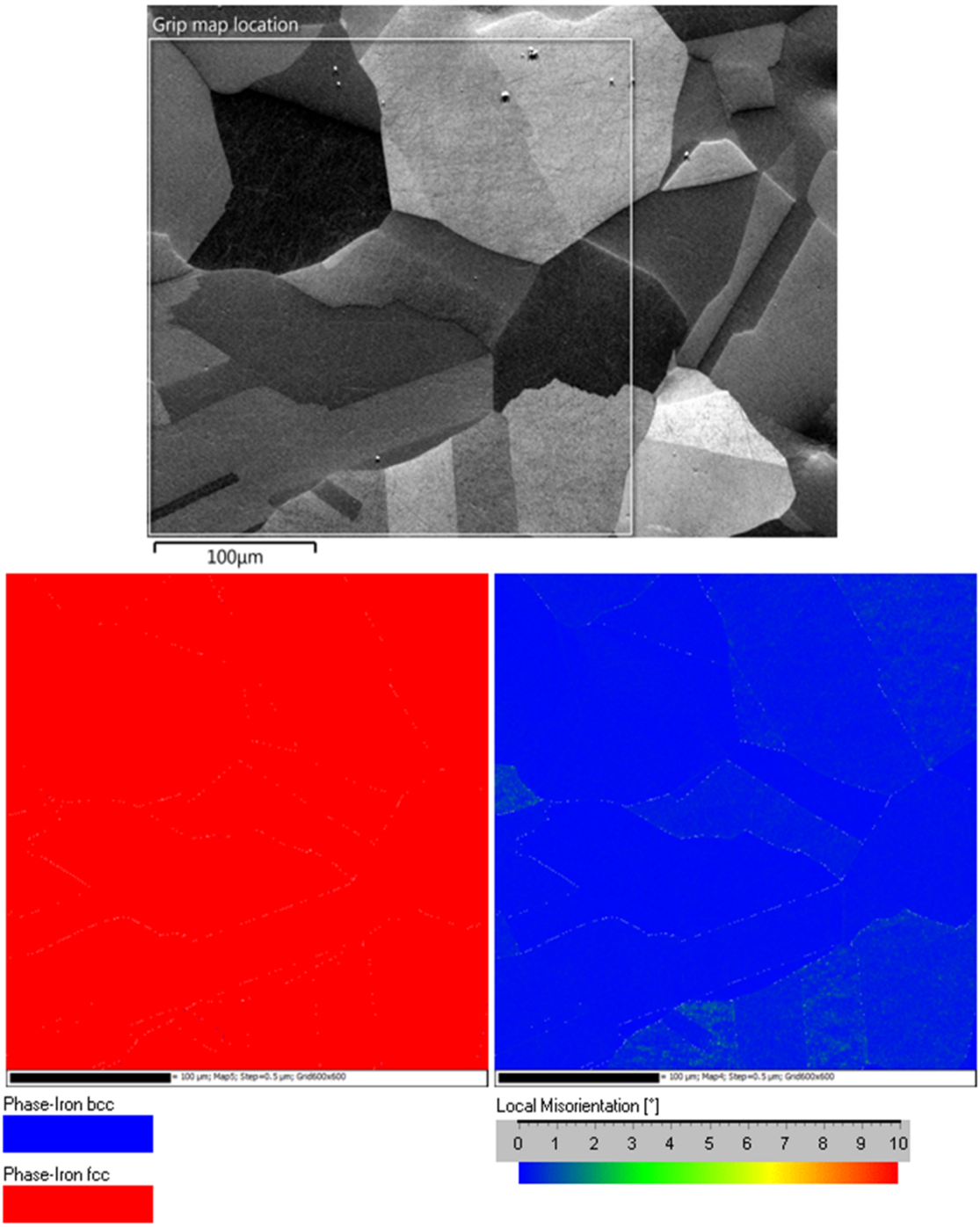

Figure 5.10: FSD image, phase, and local misorientation maps for heat 1 in the grip region.

The white regions in both the phase and local misorientation maps are points of zero solutions. Cleaning of the data decreases the zero solutions present in the map by comparing points in the map to their neighbors, attempting to index points that were not indexed.

The FSD in Figure 5.10 shows the undeformed microstructure located in the grip section

of heat. Large grains with twins present are apparent. The phase map indicates that there is no martensite present in the grip region, which is in agreement with the results of the XRD phase analysis. The local misorientation present in the grip region is mostly concentrated around the grain boundaries and in the twins and twin boundaries. There is much less white, or zero solutions, present in Figure 5.10, which indicates that a larger fraction of points were able to be indexed.

Table 5.3 shows the results of the EBSD analysis after cleaning the data to decrease zero solutions. The percent zero solutions are the highest near the break and decreases along the gauge length moving away from the break; the percent zero solutions are the lowest in the grip region. As the percent of zero solutions decreases, the total mean MAD/CI also tends to decrease/increase, which means there is a better match between the detected Kikuchi bands and the simulation used to index the bands. The local misorientation also decreases from the fractured surface to the gauge length and is the lowest in the grip regions. As the local misorientation decreases, so does the vol% BCC, which is α' martensite or δ ferrite. The highest value of martensite exists at the fracture and decreases to nearly zero in the grip region.

The mean local misorientation is plotted against the lateral engineering strain for all of the broken specimens in Figure 5.11. The top graph, (a), includes mill annealed and cold rolled starting conditions, and the bottom graph, (b), excludes the cold worked samples. A linear correlation with more scatter is present for all samples and becomes stronger when the cold worked samples are removed. Distinct groups of data points are present in (b). The low strain values correspond to the grip region; the grips are assumed to not strain upon loading and are taken to be zero axial strain. The group of data points around 0.2 are the high temperature tensile tests, the group around 0.3 are the low temperature tests, and the two highest groups are the high temperature and low temperature neck regions, respectively.

Table 5.3: EBSD results after cleaning data.

Heat	Temperature ($^{\circ}C$)	Starting Condition	Distance from Break (mm)	% Zero Solutions	% FCC	% BCC	Mean MAD/ CI	Mean LM
1	21	As machined	0.6	17.62	61.77	20.62	0.874	2.8057
			4.6	0.2739	98	1.727	0.6792	2.1436
			9.6	0.06241	99.3	0.6327	0.6314	1.7003
			grip	0	100	0	0.4657	0.2514
1	250	As machined	0.5	0.05177	99.89	0.06118	0.4697	2.2382
			5.5	0	99.95	0.04956	0.6193	1.0899
			10.5	0	99.97	0.02879	0.619	0.9896
			grip	0	99.96	0.04374	0.5553	0.8048
1	338	As machined	0.5	0	99.92	0.07835	0.4651	1.9429
			5.5	0.002215	99.96	0.03461	0.6635	0.9961
			9.5	0	99.97	0.02575	0.6085	1.0464
			grip	0.007198	99.86	0.134	0.6265	0.7527
2	21	As machined	0.4	20.22	31.45	48.33	0.9178	2.626
			4.4	4.831	78.56	16.61	0.9304	1.9809
			9.4	1.416	87.44	11.14	0.7584	1.9181
			grip	0.005833	99.96	0.03639	0.4958	0.3793
			grip	0.02194	99.81	0.1728	0.6311	0.4092
2	250	As machined	0.5	0.01633	99.93	0.05399	0.5804	1.7409
			3.4	0.04319	99.89	0.06395	0.6422	1.0667
			7.5	0.0005537	100	0.00443	0.6649	1.1448
			grip	0	99.95	0.049	0.696	0.7228
2	338	As machined	0.5	0.09718	99.82	0.08389	0.51	1.9863
			4.5	0.004707	99.96	0.03904	0.6351	0.8973
			9.5	0.02132	99.93	0.05094	0.6042	1.151
			grip	0.001384	99.89	0.1058	0.6483	0.853
3	21	20% Cold Rolled	0.5	27.35	44.39	28.26	0.9708	2.1472
			2.5	3.862	56.58	39.56	0.7327	2.0063
			4.5	0.9403	85.98	13.08	0.6983	1.9881
			grip	0.1344	97.61	2.251	0.4532	0.8511
3	250	20% Cold Rolled	0.5	0.3654	97.86	1.776	0.4687	2.0481
			3.5	0.04374	97.57	2.39	0.6284	1.1351
			7.5	0.2349	93.65	6.085	0.5251	1.2683
			grip	0.03267	99.33	0.6384	0.5606	1.241
3	338	20% Cold Rolled	0.5	1.967	93.63	4.399	0.3917	2.2673
			3.5	0.1002	67.86	32.04	0.3027	1.3381
			6.5	0.0144	98.42	1.563	0.5825	1.0926
			grip	0.0191	99.49	0.4898	0.5537	1.2233

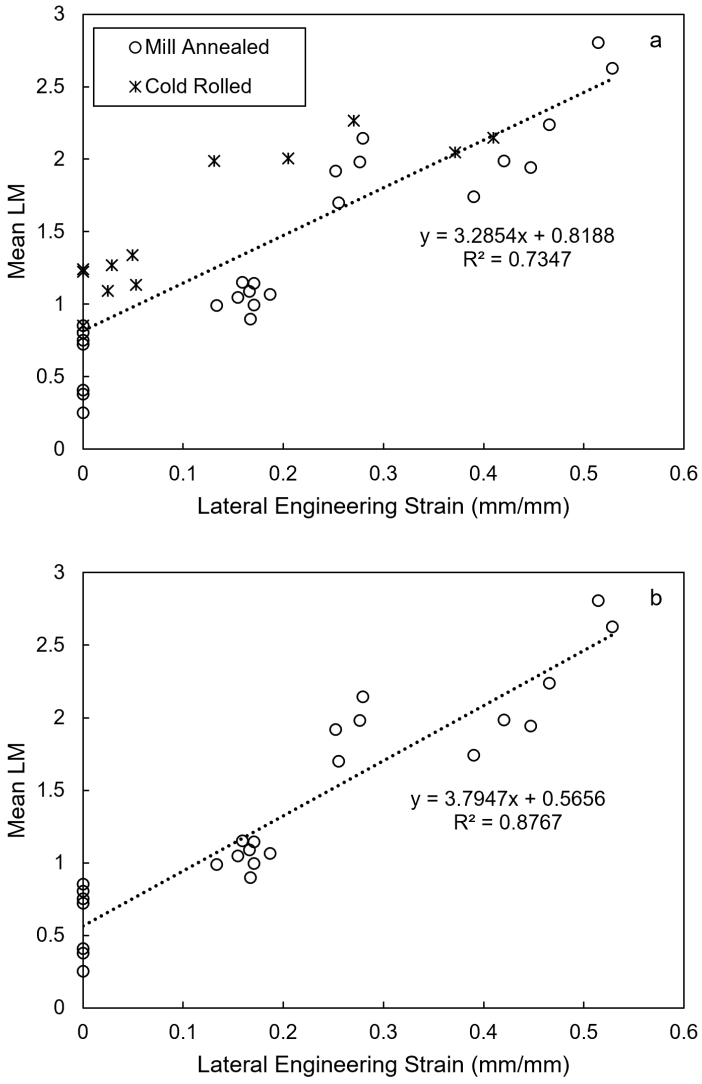

Figure 5.11: Relationship between axial engineering strain and mean local misorientation for all samples (a) and for samples without cold work (b).

Specimens Strained Using DIC

Local misorientation in the gauge for one EBSD location at each strain level is shown in Figure 5.12, and a plot of the values for the average local misorientation is shown in Figure 5.13. The local misorientation is low at the low levels of strains and increases linearly with increasing strain. Formation of deformation induced martensite is also apparent as the red in the local misorientation maps. Areas of high dislocation density are consumed by the formation of martensite, as is evident by the decrease in large green areas (local misorientation) and increase in martensite between 45%-55% strain.

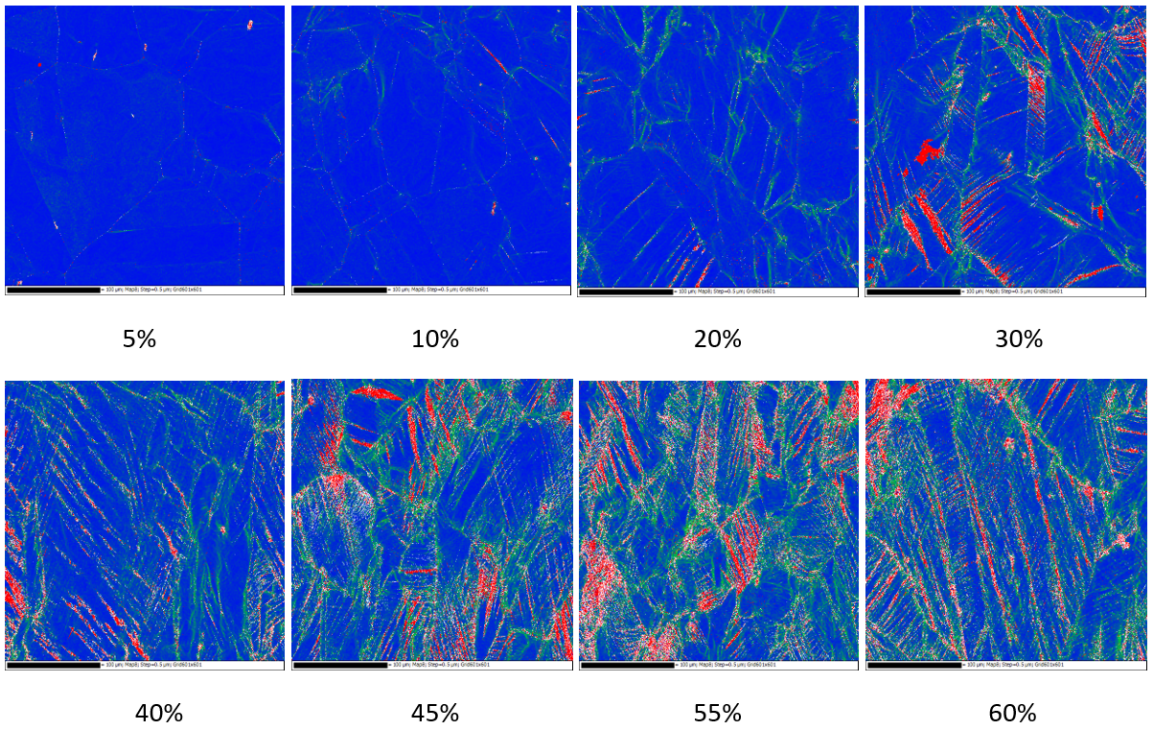

Figure 5.12: Local misorientation (green) and engineering strain as produced during uniaxial straining. Red areas in the maps are α' martensite.

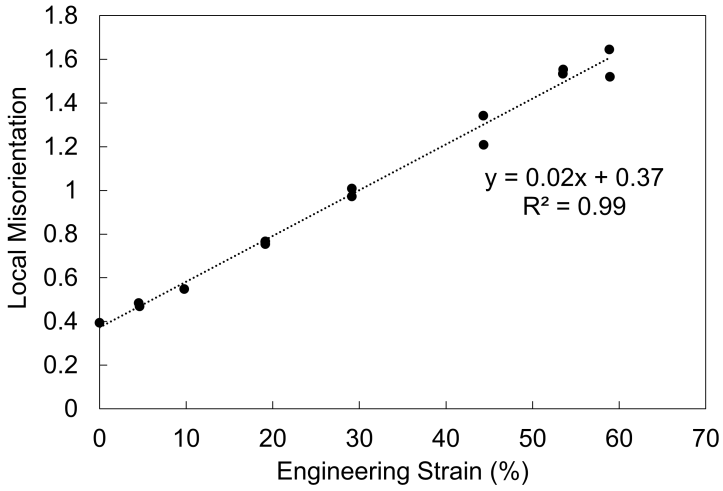

Figure 5.13: Local misorientation and plastic strain as produced during uniaxial straining

Martensite phase fraction is plotted against residual axial engineering strain for the samples with controlled strain levels in Figure 5.14. As is consistent with the local misorientation maps, the martensite is low at low levels of plastic strain and experiences rapid increase around 30 % plastic strain.

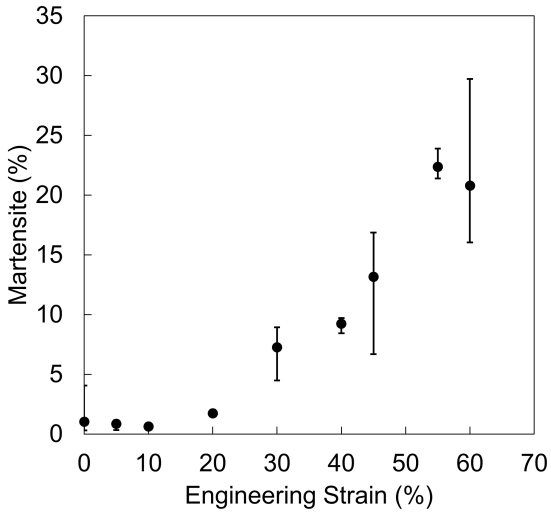

Figure 5.14: Martensite content and plastic strain as produced during uniaxial straining

5.4 Discussion

5.4.1 Mechanical Properties

Differences are seen in mechanical properties between heat 3 and heats 1 and 2; heat 3 has a notably higher yield strength, UTS, and hardness with lower total elongation and reduction in area. The differences are due to heat 3 being cold rolled to 20% reduction in thickness prior to the tensile samples being machined and tested. Cold working results in an increase in dislocation density, thereby increasing mechanical properties when testing in uniaxial tension.

Decreases in mechanical properties, such as yield strength and UTS, with increasing temperature have been reported by others and have been explained by increasing stacking fault energy with increasing temperature [9]. At lower temperatures and low SFE, strain induced martensite, which is a harder phase than austenite, can form, but its formation is suppressed at higher temperatures and higher SFE where mechanical twinning and dislocation glide are the dominant deformation mechanisms [58,60,150]. The relationship between temperature and mechanical properties will be discussed in more detail in the following chapter.

5.4.2 Hardness

Strain across the width of the gauge section is not uniform at distances closer than one fillet radius to the fillet and is more difficult to obtain through traditional testing [134]. Therefore, this region was not considered in the analysis. All temperatures tested resulted in a large range of hardness values for the same level of strain; differences of over 200 HK existed between samples tested at different temperatures. The higher average hardness in the samples strained at 21 °C may be partly due to strain induced martensite, which has a higher hardness than austenite. Similar hardness behavior for the two higher temperatures suggests that the deformation mechanisms active at both high temperatures were the same.

Cold rolled samples had a higher hardness for the same temperature than the mill annealed samples, the cold rolled samples contain dislocations and martensite in the starting microstructure which both act to increase hardness. No clear relationship is evident between hardness and axial engineering strain, as shown by the scatter in the data in Figure 5.4. However, there are similar axial engineering strain and hardness ranges for each group, shown by the dashed ovals. The majority of the data collected for each sample had a narrow hardness range suggesting that much of the gauge length had a more uniform strain behavior with the exception of the area closest to the fracture.

As shown in other studies, above 30% strain, hardness values underestimate strain present in the material [140, 141]. Minimum strain values for heat 3 are around 5% strain, which is below the 30% strain threshold; many of the strain values determined in heat 3 maintained near 20% suggesting that deformation behavior in tensile testing is affected by material condition before testing. Deformation induced by cold rolling was present in samples, resulting in a plastic strain greater than that measured by axial strain alone. Both heats 1 and 2 have minimum strain values of around 40% making the use of hardness as measurement of strain invalid with a need for other parameters to relate to strain present.

5.4.3 XRD and EBSD

plastic strain

Similar results can be seen between the XRD and EBSD for the 21 °C samples, although XRD measurements can only provide qualitative results since error in measurement may

be as high as 50%. Strain is left in the material after plastic deformation that contains both elastic and plastic plastic strain components [142]. Shifting of an XRD peak can inform the elastic strain left in the material since small changes in d-spacings are due to the nonconservative volume change that accompanies elastic strain. Plastic strain from dislocations, stacking faults and lattice distortions can be quantified by the peak broadening in a quantity referred to as microstrain [142, 143].

Microstrain values, as determined by XRD, do not vary much between heats, although heat 3 had a much lower range between the grip region and fracture than the other two heats. Microstrain measured in the grip region, which is the microstrain present in the sample before tensile testing, for heat 3 is about 0.25%. Since microstrain is measured on the microlevel, the values reported are not the same as macro plastic strain levels and are used for general trend comparisons in this work.

The trends in local misorientation, determined by EBSD, follow the trends in microstrain, although the relationship between strain and local misorientation can be used to predict the bulk plastic strain level in the sample. Local misorientation and lateral strain follow a linear relationship quite well with a better fit resulting when only considering the mill annealed conditions. A linear relationship between plastic strain and misorientation is reported for many material systems [66, 71–73]. The amount of measured lateral strain in cold worked samples would not only be due to straining to failure but also the plastic strain induced by cold working.

Local misorientation of the DIC samples also show a linear trend between local misorientation and lateral strain, although, as discussed previously, this relationship is specific to material, deformation path and microscope parameters [71, 74]. Care must be used when trying to extend this relationship to other materials and deformation modes.

Phase

Deformation induced martensite can be quantified from the XRD and EBSD data, although neither technique has the ability to differentiate between α' martensite and δ ferrite, as they are both BCC iron phases. Some of the martensite reported by these analyses is due to the δ ferrite that was in the starting microstructure. Results from XRD and EBSD of the samples

pulled to failure at 21 °C both showed that heat 3 in the cold rolled condition had the highest martensite content followed by heat 2 and heat 1. The deformation microstructure formed by cold rolling may also increase the martensite nucleation sites, resulting in more martensite formed in the cold rolled samples [43, 151]. The low content of martensite found in the grip region, as compared to the gauge region, suggests that strain induced martensite formed in each sample. Only the 21 °C samples were tested with XRD, although all temperatures were tested with EBSD to determine the effect of temperature on strain induced martensite.

Martensite, quantified using EBSD, for the high temperature samples show that martensitic transformation is suppressed at the high temperatures; no martensite forms for heat 1 or 2 in the gauge length at elevated temperature. However, heat 3 shows martensite present in the gauge length of the samples tested at higher temperatures. The grip region of all samples show that the starting martensite content was similar to that found in the low temperature tests, so martensite present in that heat is likely a result of strain. The deformation microstructure formed by cold rolling may create martensite nucleation sites that are able to be activated at high temperatures, while the nucleation sites are not present in the mill annealed samples. At elevated temperatures, the mill annealed samples do not create martensite nucleation sites and therefore no high temperature deformation induced martensite is formed in the high temperature, mill annealed samples. The formation of high temperature deformation induced martensite will be discussed in detail in the following chapter.

The samples pulled to controlled levels of strain using DIC shows little martensite transformation at low strain levels followed by a sharp increase in martensite at higher levels of engineering strain. Martensite forms in areas of high local misorientation, consuming the deformation microstructures present during transformation as was evident in the maps in Figure 5.12. The relationship between martensite and strain is consistent with room temperature deformation induced martensite created by uniaxial tension [10, 152, 153].

5.5 Conclusions

Material condition (cold work) before tensile testing affects the behavior of the material tested during uniaxial tension. Prior cold work results in higher yield strength and ultimate

tensile strength with lower total elongation. Smaller variations between microstrain, local misorientation, and phase fraction of martensite were found between the grip section and along the gauge length for the samples that had been cold worked. On average, the sample with cold work showed lower local misorientation and phase fraction of martensite at the fracture surface. Cold work may change the deformation mechanism on tensile straining.

The strain levels present in the samples pulled in tension to failure are too large to use hardness as a proxy for strain. Above about 30% strain, the hardness values predict a lower value of strain than is present in the sample; this is evident in the graph of engineering strain versus hardness, where there is a large amount of scatter in the hardness values at high strain values. Hardness was not able to be used as a proxy for strain because the samples had over 30% strain at the point of fracture.

A linear relationship exists between local misorientation and lateral engineering strain. Known anisotropy is required to relate lateral engineering strain to the normally reported axial engineering strain.

A relationship between local misorientation residual axial strain has been created for 304 pulled in uniaxial tension. The relationship is specific to this grade and these testing conditions as well as the microscope EBSD collection parameters. With proper calibration to individual materials and starting conditions, unknown plastic strain levels can be determined in components through measurement of local misorientation.

Deformation induced martensite formed in all samples pulled in tension to failure at room temperature. Both XRD and EBSD were used to determine phase fraction of austenite and martensite at various points in the gauge length and grip region. Martensite was detected in the gauge length of all samples, while only the sample cold worked prior to tensile testing had martensite present in the grip region. The martensite in the samples not cold worked was induced during tensile testing. Components present in a reactor may contain deformation induced martensite from the finishing procedures, many of which take place near room temperature, where martensite is shown to form. The effect of martensite on oxidation will be considered in more detail in a following chapter.

Deformation induced martensite was suppressed at high temperatures, with the exception of the cold rolled samples. EBSD analysis of the high temperature tensile samples

showed that the mill annealed samples did not contain any martensite in the samples, although the cold worked samples showed martensite present in the gauge that exceed that in the grip region. High temperature deformation induced martensite will be discussed in more detail in the following chapter.

CHAPTER VI

High Temperature Deformation Induced Martensite

6.1 Introduction

The 300 series austenitic stainless steels are extensively used in the primary circuit of pressurized water reactors (PWR) due to their low cost, wide availability, ease in manufacturing, and good resistance to oxidation in the environment present in the reactors [11]. As discussed in detail in the Technical Background, 304 stainless steel is metastable, where the austenite, normally an FCC crystal structure, can transform to martensite upon deformation or cooling [154, 155]. A requirement accompanying martensitic transformations is an orientation relationship between the austenite and martensite, this prevents martensite from transforming across grain boundaries [155]. The two forms of martensite that can be transformed in 304 are ε, which has a HCP crystal structure, and α', which has a BCC crystal structure. Proposed nucleation sites include shear band intersections, grain boundary triple points, twin boundaries, and twin intersections [156–159], resulting in fine martensite grains, increasing the grain boundary density in the material.

The temperature at which martensite spontaneously transforms upon cooling is a function of the alloying content and can be above room temperature for some 300 series alloy compositions. Eichelmann and Hull, Monkman, and Pickering independently created empirical equations to calculate the temperature that marks the start of martensite transformation (M_s) for cooling induced martensite transformations [3, 160, 161]. These equations are dependent upon alloying content of carbon, chromium, nickel, nitrogen along with other minor alloying additions.

Deformation-induced martensite can occur above the temperature for spontaneous trans-

formation upon cooling and is related to the dominant deformation mode present during deformation. Dominant deformation mode is related to the stacking fault energy (SFE), which is the energy required for partial dislocations to form and associated with the distance between partial dislocations. The stacking fault energy is concomitant with cross slip on glide planes and dislocation climb. Materials with low stacking fault energies promote martensite transformation via austenite to ε martensite and subsequent transformation of ε martensite to α' martensite at higher levels of strain [41, 162]. Low stacking fault energy materials also promote deformation microstructures which act as martensite nucleation sites [49].

Alloying content and temperature have an effect on the stacking fault energy in austenitic stainless steels; SFE increases as temperature increases [162]. Increasing nickel, molybdenum, and carbon increases the stacking fault energy while increasing chromium, manganese, silicon, and nitrogen decreases the stacking fault energy [163]. Regression analysis was used to determine a relationship between stacking fault energy and the major alloying content for austenitic stainless steels as follows [163]:

$$SFE = -53 + 6.2(\%\text{Ni}) + 0.7(\%\text{Cr}) + 3.2(\%\text{Mn}) + 9.3(\%\text{Mo})\frac{\text{mJ}}{\text{m}^2} \tag{6.1}$$

While the 304 grade along with some other 300 series austenitic stainless steels are metastable, not all grades in the 300 series are metastable and can be transformed to martensite due to differences in alloying compositions. Increasing temperature also increases the stacking fault energy, changing the dominant mode of material deformation, suppressing deformation-induced martensite [41, 162].

Extensive studies have considered the effect of temperature on the deformation-induced martensite transformation in annealed 304 [10, 152, 153]. Martensite transformation extent was modeled by Olson and Cohen by determining the shear band creation rate and number of shear band intersections as a function of true strain and temperature [10]. The model created by Olson and Cohen to predict the fraction of deformation-induced α' martensite is given in Equation 6.2 [10].

$$f^{\alpha'} = 1 - exp\{-\beta[1 - exp(-\alpha\epsilon)]^n\} \quad (6.2)$$

Where β is the probability of martensitic embryo formation, accounting for temperature and geometry, α is a strain dependent constant that is related to shear band formation at low strain rates, and ϵ is true strain. Both α and β parameters are dependent on temperature, and the value of martensite saturation is determined by β. Both α and β control the rate of approach to the saturation level. The shape of Equation 6.2 when martensite is plotted against true strain is sigmoidal in shape. Martensite forms the fastest with increasing strain at the lowest temperatures, while martensite saturation fraction decreases with increasing temperature. Martensite is not predicted to transform above 50 °C according to the Olson and Cohen shear band formation model.

Shear band intersections were considered to be exclusive martensite nucleation sites in the model. As mentioned previously, shear band intersections are not the only martensite nucleation sites that can be activated. A study by Abrassart on stress-induced martensite transformation in carbon steel considered the effect of activation of other potential nucleation sites [164]. The effect of prestraining at elevated temperature on the dominant deformation structures created along with the martensitic transformation upon cooling was studied. Prestraining at lower temperatures resulted in enhanced martensitic transformation upon cooling compared to samples that were not prestrained. The deformation structures created by prestraining at low temperatures promoted further transformation of martensite upon cooling.

Another limitation of the Olson and Cohen model and the experimental work on deformation-induced martensite is that only the annealed starting condition was studied. Forming and finishing processes on components in service often leave a deformed microstructure different to that found in annealed material. Although deformation-induced martensite is not predicted to form above 50 °C for an annealed starting condition, this temperature may shift with other material starting conditions. Results from Chapter 5 indicate that deformation-induced martensite forms at room temperature for mill annealed and cold rolled starting

conditions, while deformation of the cold rolled starting condition at elevated temperatures also results in deformation induced martensite.

Mode of deformation and deformation mechanisms have been shown to change the amount of deformation-induced martensite. Hecker et. al. have shown that biaxial tension resulted in higher transformation than uniaxial tension [152], and cold rolling and cold drawing have also been studied and have shown different transformation amounts between the mechanisms [165]. Most studies have focused on the low temperature transformation, within the temperature limits of the model created by Olson and Cohen. An instance of high temperature strain induced martensite transformation has been reported in duplex stainless steels [166]. Little information exists in the open literature on deformation-induced martensite at high temperatures similar to those that may be present in a nuclear reactor.

This study will consider strain induced martensite at high temperature with a focus on starting material conditions of cold rolled and annealed. Mechanical behavior of annealed and cold rolled conditions is studied at room temperature and elevated temperatures. Strain induced martensite is studied using electron backscattered diffraction to identify phase fractions of austenite and martensite. High temperature deformation-induced martensite can have important implications in environments present in PWRs, which are also susceptible to EAC. Martensite has been shown to display different oxidation behavior in some environments, compared to austenite [88]. Martensite transformation, which has been shown to occur at a crack tip of an EAC [167], may change the crack oxidation and propagation behavior in corrosion fatigue or stress corrosion cracking.

6.2 Experimental Procedure

6.2.1 Material

Three heats of a 304 stainless steel were studied with composition and stacking fault energies calculated using Equation 6.1 are given in Table 6.1. The average grain size of heat 1, 170 μm, is slightly larger than that for heat 2, 130 μm, and heat 3, 120 μm, and small amounts of δ ferrite were present in every heat. Dog bone specimens with rectangular cross sections were machined from each heat according to Figure 6.1. A section of material from heat 3 was cold rolled to 20% reduction in thickness with one rolling pass before machining dog

bone specimens.

Table 6.1: Composition and stacking fault energy of the 304 stainless steel heats.

Heat	C	Mn	P	S	Si	Cr	Ni	Mo	N	Cu	SFE (mJ/m^2)
1	0.042	1.70	0.026	0.006	0.045	18.39	8.72	0.26	0.07	0.17	19.4
2	0.040	1.46	0.002	0.015	0.045	18.39	9.13	0.26	0.03	0.10	21.2
3	0.040	1.45	0.021	0.016	0.045	18.36	9.28	0.26	0.03	0.10	22.0

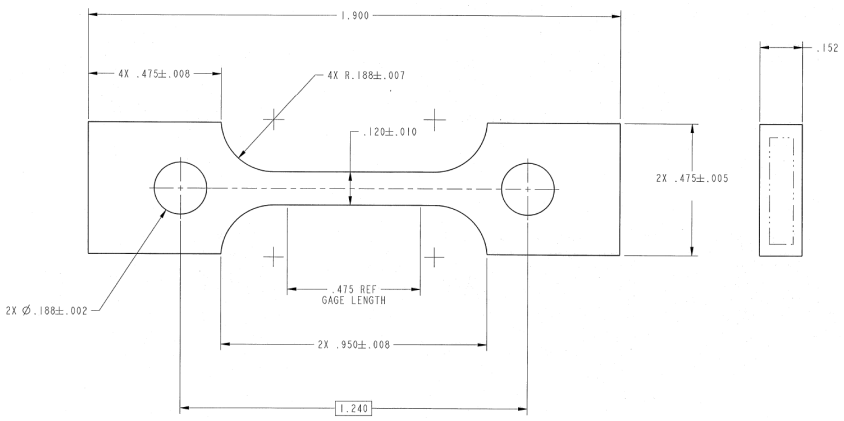

Figure 6.1: Tensile specimen used for uniaxial straining.

6.2.2 Uniaxial Tension

The test matrix for the specimens investigated is compiled in Table 6.2. One dog bone specimen of heat 1 and heat 2 in the mill annealed condition and one from heat 3 in the 20% cold rolled condition were pulled in uniaxial tension to failure at 21, 250, and 338 °C and air cooled at room temperature after failure. Dog bone specimens of the mill annealed condition of heat 3 were pulled in uniaxial tension in room temperature air using Digital Image Correlation (DIC) to specified amounts of plastic strain from 10-60% axial engineering strain before unloading to zero load. All samples were pulled in uniaxial tension at a rate of 0.0036 mm/s up to 4% strain after which the rate was increased to 0.042 mm/s to the final desired strain level or failure.

Table 6.2: Test matrix for all specimens.

Heat	Starting Material Condition	Temperature (°C)	Final State/ plastic strain (%)
1	Mill Annealed	21 250 338	Failure
2	Mill Annealed	21 250 338	Failure
3	20 % Cold Rolled	21 250 338	Failure
	Mill Annealed	21	5, 10, 20, 30, 40, 55, 60

6.2.3 Microstructural Characterization

The starting microstructure of each heat was determined through optical microscopy. Polished samples were electrolytically etched using 10% by volume oxalic acid in water at 6V. Optical microscopy with polarized light was used to image the microstructure.

6.2.4 Electron Backscatter Diffraction

Electron backscatter diffraction (EBSD) was performed using a Thermo-Fisher Scientific Apreo S Field Emission Gun SEM with an EDAX detector for 21 °C specimens pulled to plastic strain values using DIC and a Hitachi SU21 3 Field Emission Gun SEM with an Oxford detector for the specimens pulled to failure at all temperatures. All maps were collected with Oxford Instruments Aztec 4.2 software [147]. Maps were collected on 300 µm x 300 µm areas using a step size of 0.5 µm at 3 points in the gauge length and one point in the grip on each specimen. Random EBSD map locations in the gauge were collected for the specified strain samples, while the EBSD map locations for the fractured samples were evenly spaced in the gauge from the fracture towards the grip.

Phase maps were created for each EBSD map using FCC austenite and BCC martensite

for the samples pulled to failure and FCC austenite, BCC and HCP martensite for the samples pulled to specified value of strain using Oxford's HKL Channel 5 software [148]. Successive maps were created moving from the fracture to toward the grip on the fractured specimen while three locations at random points in the grip were created for the controlled strain samples and average phase fractions were determined.

6.3 Results

6.3.1 Mechanical Properties

Stress vs. strain plots are shown in Figure 6.2 for the samples pulled in uniaxial tension to failure in air at all three test temperatures, and the yield strength as a function of temperature is shown in Figure 6.3. The highest yield strength, ultimate tensile strength, and elongation at failure is evident with the lowest temperature test. Similar mechanical property values are apparent between the two higher temperatures, although the highest temperature results in a slight decrease in total elongation and ultimate tensile strength. Heats 1 and 2 display similar behavior at all temperatures tested while heat 3, which was cold rolled prior to uniaxial tension, shows a pronounced increase in yield strength and ultimate tensile strength while also having a lower total elongation and lower strain at failure. The negative correlation, given by the slope of a linear fit in Figure 6.3, between yield strength and temperature is consistent for each heat.

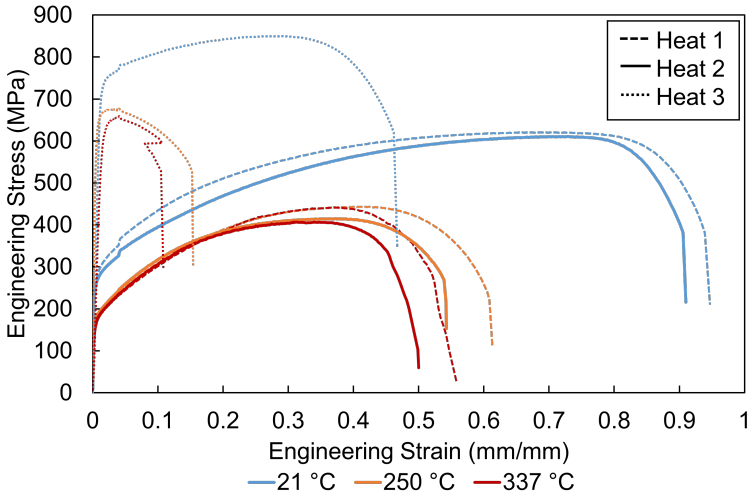

Figure 6.2: Stress vs strain curves for all three heats at the three temperatures tested in uniaxial tension to failure.

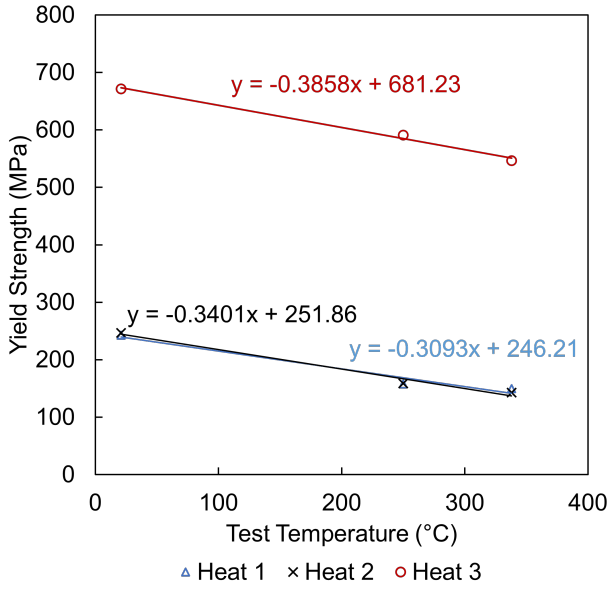

Figure 6.3: Yield stress for all heats pulled to failure for each temperature.

6.3.2 Microstructure

Starting microstructure for heats 1 and 2 in the mill annealed condition and heat 3 in the 20% cold rolled condition is shown in Figure 6.4. All three heats have similar microstructure, with heat 1 having a slightly larger average grain size than heat 2 and heat 3, and annealing twins are present in all heats. Deformation from cold rolling, as indicated by the yellow arrow, can be seen in the grip microstructure in heat 3, while no deformation is apparent in starting condition of either heat 1 or heat 2. Deformation twins were also present in the microstructure at all values of residual engineering strain in the samples pulled to controlled strain levels in room temperature air.

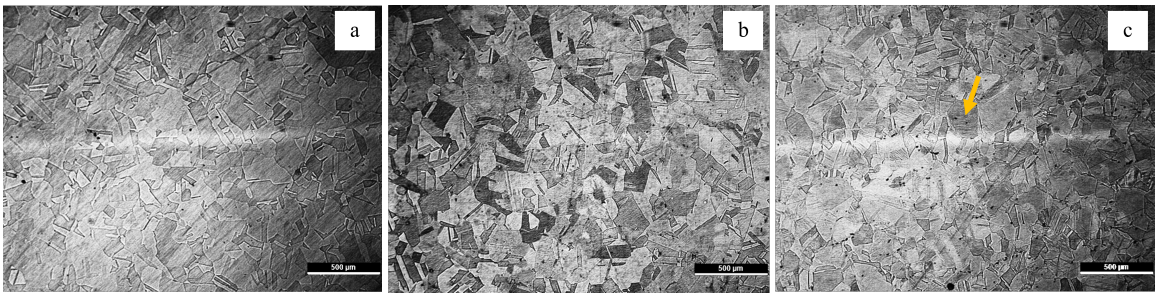

Figure 6.4: Light optical microscopy for heats a) 1 and b) 2 in the annealed starting condition and c) 3 in the 20% cold rolled starting condition. The yellow arrow in c) highlights deformation created by cold rolling.

6.3.3 Deformation induced martensite

Controlled Strain Levels of Uniaxial Tension

Martensite volume percent, as determined by EBSD at three separate regions in the gauge region of each sample, is plotted against residual engineering strain in Figure 6.5 for heat 3 in the mill annealed condition pulled in uniaxial tension in room temperature air. The small amount of δ ferrite present in the starting microstructure is included in this fraction. The minimum and maximum values are given by the error bars. The percent martensite remains low and fairly constant below 10% engineering strain, after which, it steadily increases with increasing strain. The relationship between strain and martensite created by Olson and Cohen is overlaid onto the data as the dotted line; a value of n = 4.5 in Equation 6.2, consistent with what Olson and Cohen used for experimental data, fits the collected data well [10].

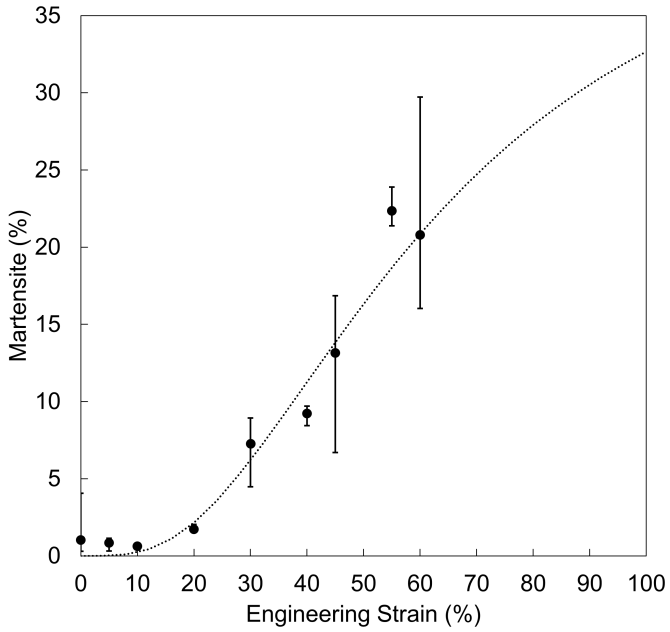

Figure 6.5: Total martensite volume percent, determined by EBSD phase maps, vs engineering strain in the gauge region The dashed line is the relationship between martensite and plastic strain created by Olson and Cohen (Equation 6.2) [10].

EBSD phase maps for one location in the gauge of all of the samples pulled to various levels of plastic strain are shown in Figure 6.6. Both ε (yellow) and α' (red) martensite were indexed on these specimens. ε is not present below 20% engineering strain, and the

ε is exclusively located adjacent to α' martensite at the higher strain levels. Martensite remains low at low levels of plastic strain until it begins to form across austenite grains. Fine grains of martensite are seen formed across austenite grains above 20% plastic strain and martensite grains are formed between other martensite grains above 40% strain.

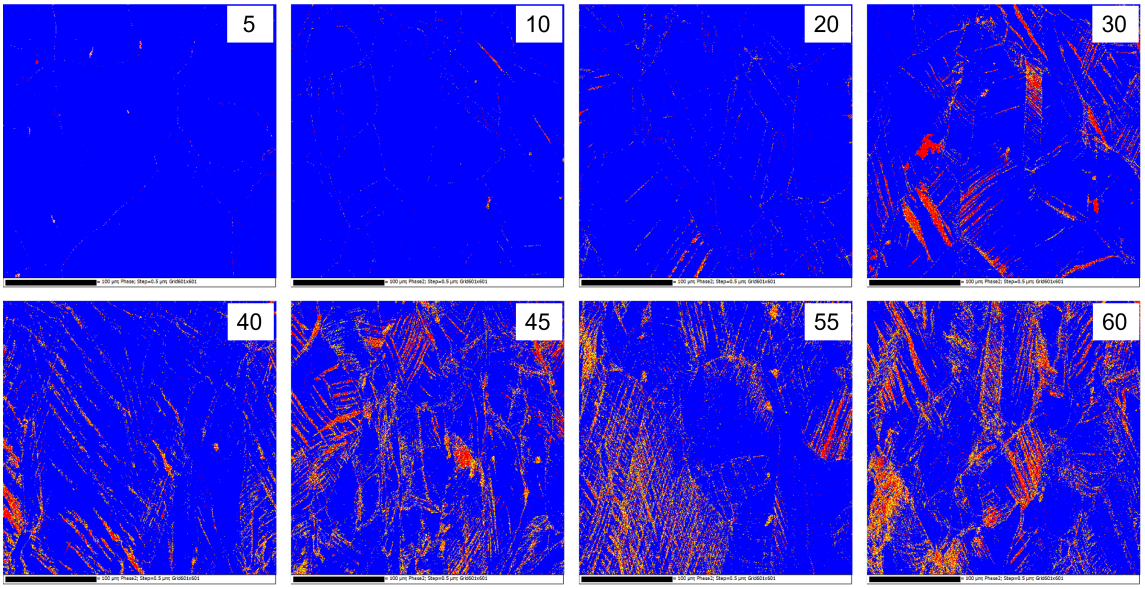

Figure 6.6: EBSD phase maps of austenite (blue), ε martensite (yellow), and α' martensite (red) for plastic strain samples: 5%, 10%, 20%, 30%, 40%, 45%, 55%, and 60%. Black scale bar for each map is 100 μm.

Uniaxial Tension to Failure

The volume percent of martensite was determined for each specimen pulled to failure at each temperature and is plotted against the lateral strain determined by post test measurements in Figure 6.7, with heat 1 represented by triangles, heat 2 by x's, and heat 3 by circles. The low temperature tests are in (a), and the two elevated temperatures are plotted together in (b). No martensite was found to be present in the grip region for each sample; although, a small, nonzero, amount of martensite is present in the grip of the cold rolled starting condition at all temperatures tested. δ ferrite was found to be present in the starting material condition for all heats and is indistinguishable from α' martensite using EBSD since they are both BCC phases. The grip region is assumed to be close to the starting microstructure of the material, incurring minimal deformation during uniaxial tension. Deformation-induced martensite transformed in all heats at 21 °C. Martensite also formed

in the gauge region of the cold rolled starting condition at the two higher temperatures, although no martensite was detected at elevated temperatures for the annealed starting condition. Deformation twins were present in the gauge region at all temperatures for all heats.

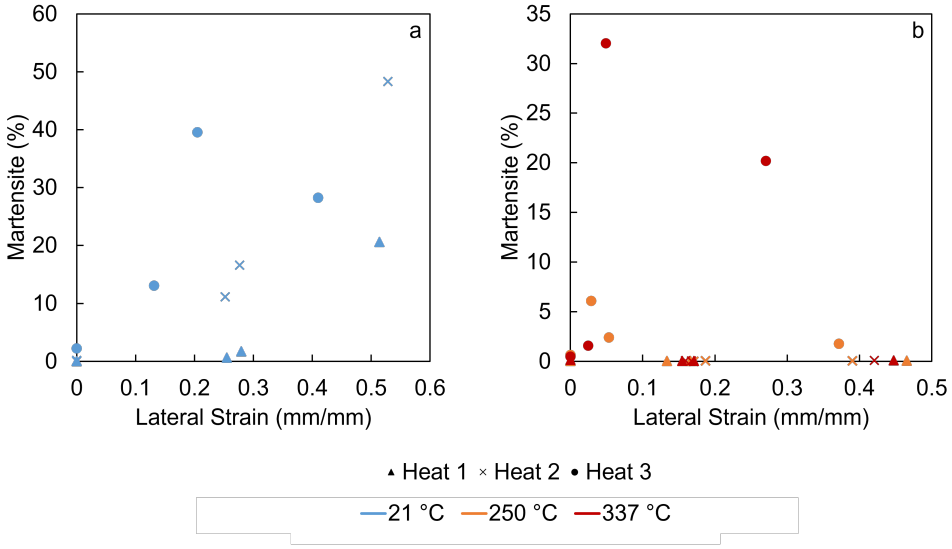

Figure 6.7: Phase fraction of martensite as a function of lateral strain, measured by EBSD, for the room temperature specimens pulled to failure a) and the high temperature specimens b) pulled to failure.

EBSD phase maps for three locations in the gauge and one in the grip of the heat 3 specimen pulled to failure at 338 °C are shown in Figure 6.8 with approximate locations given on the broken tensile specimen. Martensite was formed at all locations on the specimen, including in the grip, indicating the starting condition contained a small amount of martensite. The maximum martensite fraction is seen at the location second closest to the fracture. Parallel bands of martensite, or laths, are seen at all locations except the map within the necked region. The map in the neck shows approximately parallel bands formed at the point closest to the fracture, although the martensite is seen to be curved, unlike martensite formed in the other areas. Martensite did not form between other martensite grains, as was seen in the room temperature tests in Figure 6.6. Martensite observed at each location is sensitive to the grain orientation of each map and may not be representative of the sample as a whole on relatively small map sizes.

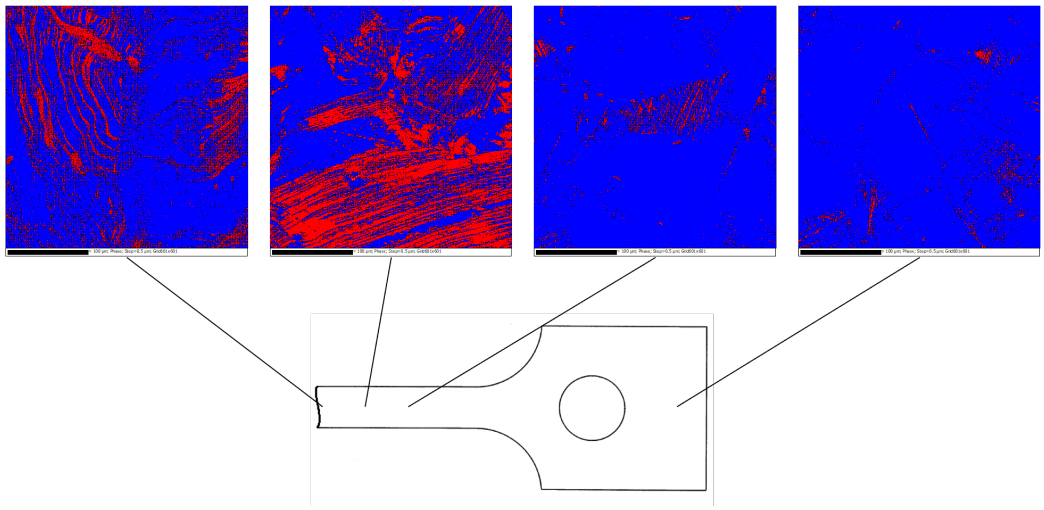

Figure 6.8: EBSD phase maps for 338 °C cold rolled specimen. Black scale bar for each map is 100 μm.

6.4 Discussion

6.4.1 Mechanical Behavior

Heat 3 displays markedly different mechanical behavior than heats 1 and 2 at all temperatures; this is expected for a cold rolled material condition which contains a large amount of deformation structures from its starting condition. The effect of dislocation pile ups, such as would be present in a cold worked sample, on Hall-Petch strengthening is proposed by Li [168] to increase the yield stress and subsequent UTS, as is seen in the stress vs. strain curves for the cold worked specimens.

Both the annealed and cold rolled conditions exhibit similar changes in mechanical behavior with increasing temperature. The mechanical properties decrease with increasing temperature owing to the change in stacking fault energy and subsequent changes in the dominant deformation mode [58, 150, 162]. Although cold rolling changes the general shape of the stress vs. strain curve, cold rolling does not change the temperature dependent mechanical properties of the material.

6.4.2 Martensite Transformation in Room Temperature Air

plastic strain

A sigmoidal increase in martensite with increasing engineering strain in Figure 6.5 is consistent with results compiled from Hecker et al and Angel and is modelled well by the Olson and Cohen model in Equation 6.2 [10, 152, 153, 169]. Saturation of deformation-induced martensite is not evident at 60% engineering strain, as predicted by the fit from Olson and Cohen. The grips, which were labeled as 0% engineering strain, show some martensite, or BCC phase from the EBSD analysis. As discussed previously, both α' martensite and δ ferrite are BCC phase and indistinguishable using EBSD. A small amount of δ ferrite was found to be present in the starting material condition and can account for the α' martensite indexed in the grip region.

Variation in martensite content in Figure 6.5 at each strain level is likely due to the small map size relative to the grain size. As mentioned previously, an orientation relationship exists between the austenite and deformation-induced martensite. Only grains with a favorable orientation to the axis of loading will transform to martensite. No specific austenite orientation was found to preferentially transform to martensite in this work.

The EBSD phase maps in Figure 6.6 shows mainly austenite present at low levels of strain. Increasing levels of strain results in martensite grains forming across austenite grains along with martensite grains forming between martensite grains at higher levels of strain. This is also consistent with the orientation relationship requirements between austenite and martensite, martensite grains terminate at grain boundaries.

Both ε and α' martensite were indexed on the EBSD phase maps. A maximum of ε martensite around 15% strain, as reported in literature, was not apparent [170]; rather, ε was not present until 20% strain. ε at high levels of strain is an unexpected result, as ε martensite should be thermodynamically unstable at the large values of strain present in the sample. Few reference Kikuchi patterns exist for low temperature HCP iron, so the pattern used to index the ε phase is found at very high pressures. The location of the ε martensite indexed is almost exclusively next to α' martensite. As discussed previously, α' martensite can directly transform from austenite, or ε martensite can be an intermediate

phase in the transformation of austenite to α; martensite. The small amount of ε indexed may be un-transformed ε martensite during the $\varepsilon \rightarrow \alpha$' transformation.

Strain to Failure

As with the samples pulled to various levels of plastic strain, the mill annealed samples pulled to failure in room temperature air (Figure 6.7) have a roughly a sigmoidal relationship between plastic strain and martensite fraction formed. The relationship between strain and percent martensite is less obvious for the cold rolled starting condition. The mill annealed conditions are expected to behave similarly to those modeled by Olson and Cohen [10], although similar studies have not considered cold rolled starting conditions. The cold rolled starting condition contained deformation in the starting microstructure, as shown in Figure 6.4 and confirmed in EBSD analysis. Nucleation sites, in addition to those proposed by Olson and Cohen, may be activated or created upon deformation resulting in a deviation from sigmoidal behavior [10].

6.4.3 Martensite Transformation at Elevated Temperature

The M_s temperature for each heat, as determined by alloy composition using the Pickering equation is shown in Table 2 [3]. Heat 1 requires the coldest temperature for cooling induced martensite transformation, followed by heat 2, which is close to the temperature required from heat 3. The specific values determined for Ms temperature are not of particular interest for this study, although it confirms that these heats will not spontaneously transform to martensite upon cooling unless cooled to a very low temperature. The temperature needed to achieve spontaneous transformation is unlikely for many commercial applications.

Table 6.3: Ms temperature (°C) for each heat using the Pickering empirical formula. [3]

Heat	Pickering
1	-205
2	-128
3	-99

Because the low temperature required to spontaneously transform martensite was not

reached during processing or the experiments, martensite transformed in all samples studied was due to deformation-induced martensite mechanisms. Cold rolling can cause deformation-induced martensite, which was seen in the grip of all of the heat 3 samples [165]. Heat 3 specimens underwent strain induced martensite at all temperatures tested, resulting in a much higher temperature at deformation-induced martensite transformation than predicted by Olson and Cohen [10]. Olson and Cohen and others who studied deformation-induced martensite considered an annealed material starting condition and based their prediction on creation of intersecting shear bands as nucleation sites for martensite.

As discussed previously, martensite nucleation sites have been proposed to include more sites than shear band intersections alone. Martensite has also been proposed to nucleate at grain boundary triple points, twin boundaries, and twin intersections [164]. A large amount of deformation twins can result from cold rolling and were confirmed to be present in the EBSD results, that may act as martensite nucleation sites at high temperatures.

Nucleation sites must be created and then activated for deformation-induced martensite transformation. In the room temperature tested samples, where the stacking fault energy of these alloys remains low, nucleation sites are created and activated during deformation. At higher temperatures, the stacking fault energy increases, causing a change in the dominant deformation mechanism, preventing deformation-induced martensite [41, 162].

The effect of cold rolling and cold drawing on deformation-induced martensite has been studied in a 316 grade stainless steel, which has a higher stacking fault energy due to additional alloying requirements and is more resistant to deformation-induced martensite than 304. Cold rolling creates a deformation microstructure that can contain martensite nucleation sites that remain in the material at high temperature [169, 171], although deformation can also result in mechanical stabilization preventing martensite transformation [158]. Deformation-induced martensite mechanisms can proceed at higher temperatures when the martensite nucleation sites are present because deformation only needs to activate the nucleation sites.

Cold rolled starting material condition resulted in deformation-induced martensite at all of the temperatures tested. During deformation, microscopic stress/strain states seen at the grain level vary from grain to grain. Grains that are favorably oriented with the

direction of loading will see larger total strain and experience further deformation-induced martensite. The relatively small size of the EBSD map compared to the grain size of the material means that the location of the EBSD map can have a large effect on the amount of martensite determined.

With the exception of the map closest to the fracture, the martensite morphology formed in all of the maps of the cold rolled sample pulled to failure at 338 °C show nearly parallel, alternating austenite and martensite grains. The map closest to the failure surface has similar features, although the martensite and austenite no longer have linear features, but the grains are curved. This suggests that the martensite found in this map was formed before necking, and subsequently changed shape during necking. The stress state inside the neck is triaxial, which is not specifically investigated in this study.

High temperature martensitic transformation in 304 has important implications for the nuclear power industry in PWRs, where 304 components are exposed to high temperature water. Under the right starting material conditions, the complex stress states present in EAC can lead to high temperature deformation-induced martensite [167]. Computational models used to predict EAC do not consider the possibility of high temperature deformation-induced martensite, which can change the mechanical properties of the material along with the oxidation resistance [172, 173].

6.5 Conclusions

Stress vs. strain behavior differed between the annealed and cold rolled starting conditions. The stress vs. strain curve for the annealed and cold rolled conditions showed different behaviors at all temperatures. Cold rolling results in an increase in yield strength and ultimate tensile strength with a reduction in uniform elongation compared to the annealed condition. Deformation from cold rolling is responsible for the differences in mechanical properties between the two starting material conditions.

The dominant deformation mode active at room temperature differs from that at the two elevated temperatures studied. The stress vs. strain curve shows a decrease in yield strength, ultimate tensile strength, and reduction in uniform elongation at elevated temperatures. Increase in stacking fault energy at elevated temperatures results in a change in the

dominant deformation mode along with a change in mechanical properties. The dominant deformation mode active at each temperature was not directly studied.

Cold rolling creates a deformation microstructure that promotes deformation-induced martensite at high temperature. Deformation-induced martensite was observed to form in specimens subjected to cold rolling prior to testing regardless of the test temperature. The annealed material condition transformed to martensite with uniaxial tension at room temperature, but no transformation was detected at the two higher temperatures.

Microstructure of the deformation-induced martensite in the cold rolled samples differs from that of the annealed samples. Martensite is only found to form across an austenite grain in the cold rolled samples, where martensite is also found to form between martensite grains in annealed starting condition. In the region closest to the fracture of the elevated cold rolled sample, martensite grains are no longer parallel. The martensite present in this region formed before necking and curved during necking.

Under the right prior material condition and straining conditions during operation martensite can be formed inside an operating PWR. Martensite has a different crystal structure than austenite and has been shown to have different oxidation behavior than austenite in some environments. Material models may need to account for this phenomenon to obtain more realistic outcomes.

CHAPTER VII

Effect of Surface Condition on Oxidation in Low Temperature Air

7.1 Introduction

Understanding the effect of near surface microstructure on short term oxidation kinetics of austenitic stainless steel in low temperature air is necessary to understand the relationship between material condition and environment. The austenitic grades form an oxide layer(s) when exposed to air, which is accelerated at higher temperatures [80]. The effect of temperature on oxidation often follows an Arrhenius relationship [174]. Kinetic studies of oxidation behavior are commonly performed by thermogravimetric analysis (TGA), which uses a microbalance coupled to a furnace system that simultaneously monitors the mass of the sample while controlling the temperature and atmosphere [174, 175]. Kinetic parameters can be determined by fitting rate constants to mass change, normalized by surface area, per time.

The main objective of this study is to induce different surface microstructures and study the short time oxidation at low temperatures in synthetic air. High sample throughput allowance of a TGA makes this system ideal to study a large range of sample conditions. Two surface conditions, including near surface martensite and surface finish, are of interest; this analysis focuses on machined sample finish at a range of low temperatures. Samples were exposed to synthetic air at 280, 400, and 700 °C for 50 hours. Oxidation kinetics were studied through thermogravimetric analysis during exposure along with mass measurements before and after exposure. The oxide was imaged after exposure with a scanning electron microscope (SEM) and a plasma focused ion beam (PFIB) to image cross sections.

7.2 Technical Approach

7.2.1 Material

The materials of interest for this study include 304; select chemistry of the 304 is shown in Table 7.1. The 304 was in an as machined material condition prior to thermogravimetric specimen preparation.

Table 7.1: Chemistry for the 304 exposed to low temperature air.

Heat	C	Mn	P	S	Si	Cr	Ni	Mo	N	Cu
1	0.042	1.70	0.026	0.006	0.045	18.39	8.72	0.26	0.07	0.17

Thermogravimetric analysis samples of the 304 grade were created with electric discharge machining (EDM) followed by mechanical machining to remove the surface induced through EDM. A hole was drilled into the samples to allow for exposure in the TGA.

7.2.2 Thermogravimetric Analysis

TGA was used to expose machined finish 304 samples to a controlled atmosphere while simultaneously monitoring the mass change. Experiments were performed in a Netzsch STA 449 F1 Jupiter in TGA mode. Samples were exposed to synthetic air (80% nitrogen/20% oxygen) at a flow rate of 50 ml/min. Three exposure temperatures: 280, 400, and 700°C were studied with the sample suspended on an alumina sample hanger. Each exposure was repeated for a total of three exposures at each condition. Samples were heated at a rate of 20 °C/min and held 50 hours at the desired temperature. The sample chamber was evacuated before exposure using one automatic vacuum cycle with an auxiliary vacuum system before filling the chamber with the synthetic air and ramping the temperature. Netzsch Proteus software was used to analyze the results after exposure.

7.2.3 Oxide Analysis

The morphology and thickness of the oxide created was studied using a FEI Helios 6600 Dual Beam PFIB/SEM. The oxide formed on the surface was imaged, and cross sections were created using the PFIB and the oxide and metal interface was imaged with SEM.

7.3 Results and Discussion

7.3.1 Thermogravimetric Analysis

The results of 280, 400, and 700 °C TGA runs of machined 304 at 50 hours each are shown in Figure 7.1. Mass gain during heating, at the beginning of the experiment, is higher as temperature is increased, although the slope of mass change per time is very similar for each of the three runs. The mass change as determined from TGA analysis, after the samples had reached the hold temperature, along with mass change determined by mass measurements before and after exposure are given in Table 7.2. Very little mass change is reported from both the TGA and before and after test measurements. Poor agreement exists for the mass change determined by both techniques.

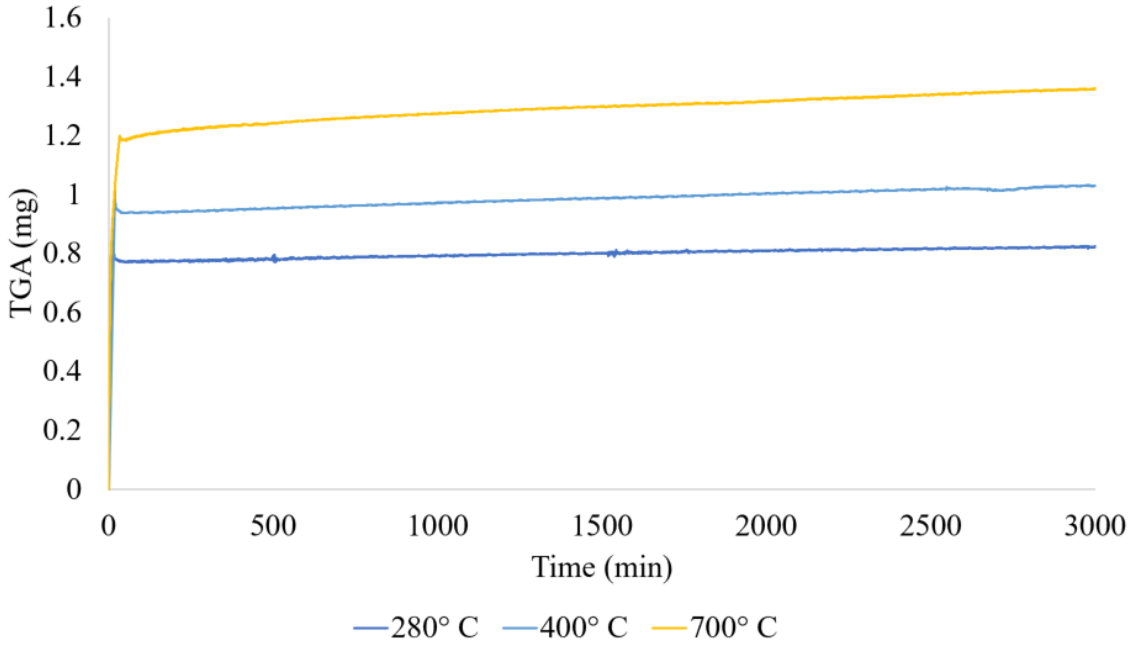

Figure 7.1: TGA results for 304 at 3000 min (50 hour) exposures to synthetic air at 280, 400, 700 °C.

Table 7.2: Mass change for each specimen determined by TGA and pre- and post-test mass measurements with a balance.

Temperature (°C)	TGA (mg)	Balance (mg)
280	0.04	-0.021
400	0.08	-0.003
700	0.17	0.153

The initial large mass gain in the TGA signal is due to the buoyancy effect of the change in air temperature when heating. Buoyancy force can be defined as:

$$F_{buoyancy} = \rho g V \tag{7.1}$$

Where ρ is the density of the fluid, g is the gravitational force, and V is the volume of the fluid displaced. As the temperature increases, the density of the air changes, resulting in a change in buoyancy force. The ideal gas law can be used to calculate the density of dry air at a given pressure and temperature:

$$\rho = \frac{p}{R_{specific} T} \tag{7.2}$$

Where p is the pressure, $R_{specific}$ is the specific gas constant, and T is the temperature. During the heating portion, the density of the air is decreasing resulting in a smaller buoyancy force on the sample which shows up as a mass gain in the TGA signal. Empty TGA runs can be used to determine the effect of buoyancy in the system, although the volume of the displaced air will be different from an empty run and one with a sample.

There is little agreement between the mass change determined by TGA and by pre- and post-test mass measurements. Over the course of 50 hours, there is balance drift that causes the mass measurements to change regardless of sample mass change due to oxidation. The similar slopes of all three temperatures in Figure 7.1 indicates that the mass change detected

by the microbalance may largely be due to balance drift and not oxidation. Differences between the two measurement techniques are likely due to the inability of the instrument to measure the precise mass required by the system.

7.3.2 Oxide Characterization

A SEM image of the 400 °C exposure using the through lens detector is shown in Figure 7.2. The brighter areas are higher than the darker areas. Small, discrete oxides, which appear as bright dots, are seen throughout the surface. Other high and low areas are apparent and are a result of machining.

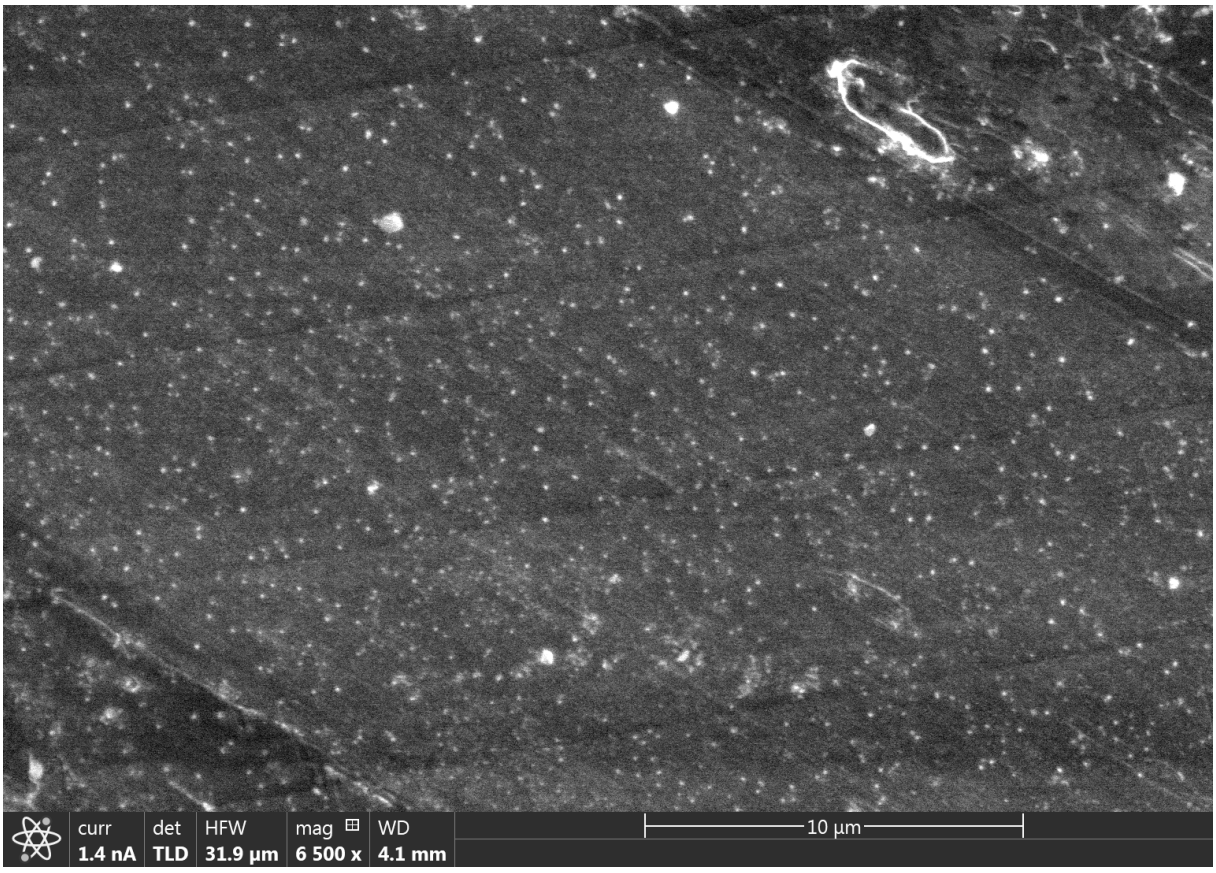

Figure 7.2: SEM image of 400 °C, 50 hour exposure using the through lens detector.

Cross sections were also milled with the PFIB and then imaged with SEM. Figure 8.9 shows a cross section of the metal and oxide, using the Everhart-Thornley detector, with outer oxides or surface deformation on the metal. Two separate platinum layers are visible: the platinum layer deposited with the electron beam is closer to the oxide surface and the

platinum layer deposited with the ion beam is more porous and brighter in the image. Either oxide particles or surface deformation are present as protrusions from the metal surface. The inner oxide is not resolvable with SEM at the low temperature, short time exposures.

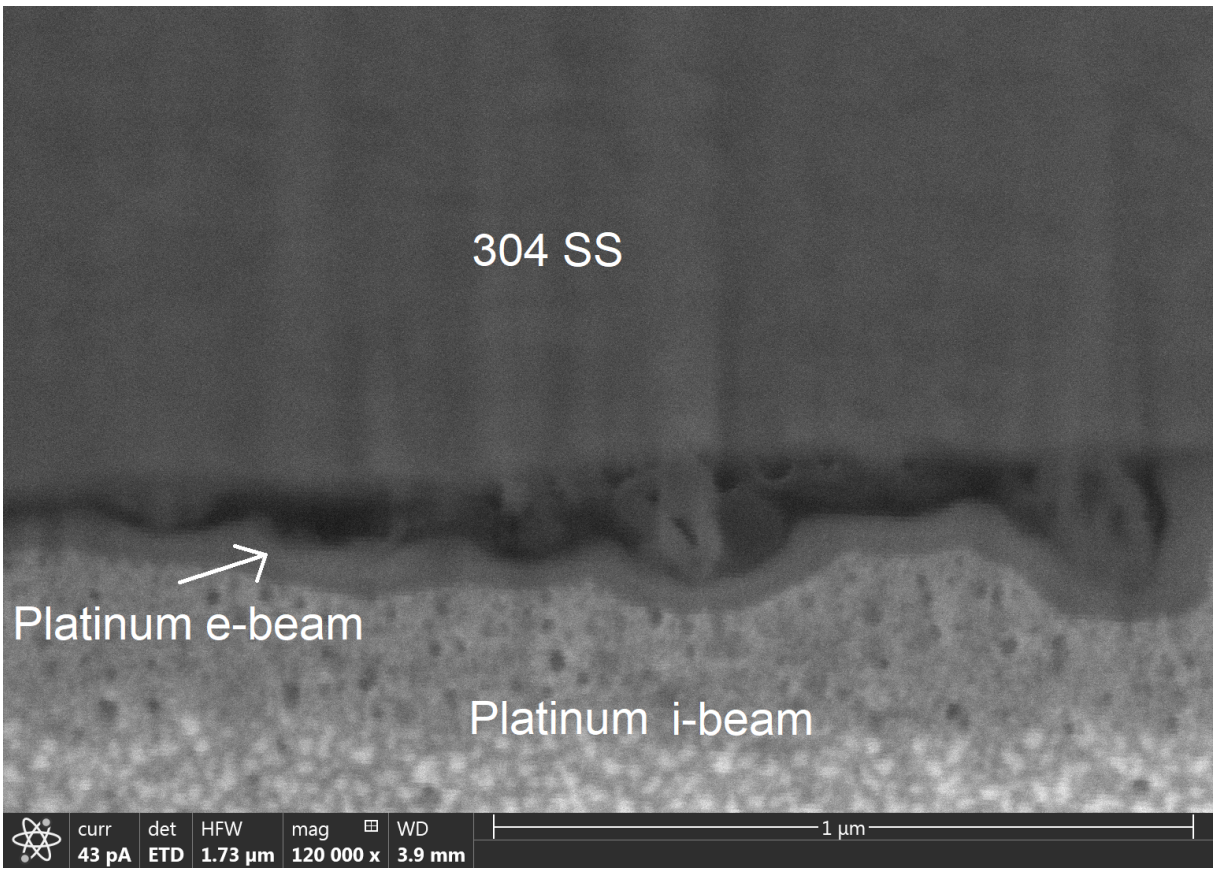

Figure 7.3: SEM image of a cross section through the oxide into the metal substrate.

7.4 Conclusions

The TGA and balance used to monitor the mass change due to oxidation both during and after low temperature exposure to synthetic air do not have high enough resolution to capture the mass change due to oxidation. Mass change in the TGA signal throughout the entirety of the temperature hold may be accounted for by TGA balance drift. The balance used to measure mass before and after experiments reported a negative mass change, although SEM confirmed that an oxide layer formed on the sample surface. The advantage of the TGA allowing high sample throughput, facilitating studies of many sample starting

conditions cannot be capitalized with the environmental conditions studied in the TGA. Rather, further TGA studies on material surface finish were replaced with exposures in high temperature water, and will be addressed in a later chapter.

Discrete oxide particles are present on the sample surface as a result of short time, low temperature exposure. Presence of a separate inner and outer oxide layer and oxide thickness measurements are not able to be determined using SEM for the low temperature, short time exposures.

CHAPTER VIII

Effect of Material Deformation on Short Time Oxidation in High Temperature Water Environments

8.1 Introduction

Type 304 stainless steel is commonly used in pressurized water reactor (PWR) primary circuits, where they are exposed to high temperature, high pressure water [4,17]. Combination of material and environment influence the oxidation behavior in these systems [14,176]. In addition to oxidation of the surface, 304 is also susceptible to stress corrosion cracking and corrosion fatigue, which are both types of environmentally assisted cracking, or EAC [24, 177–179]. EAC is a function of prior material condition, environment, and stress induced during exposure. During EAC, the material will experience increasing deformation due to the stress as a result of thermal fatigue, residual stress from welding, and or vibrational induced stress followed by periods of crack growth, exposing new material to the environment. The newly exposed material in the crack tip will undergo oxidation, cyclically repeating until failure. Short time oxidation behavior and the effect of near surface microstructure on oxidation are essential to characterize oxidation events during crack growth in EACs.

Oxidation of 304 stainless steels in high temperature, high pressure, water environments at long exposure times is a well studied system [14,22,23,105,118,176,180–183]. The literature is unanimous that a dual oxide layer forms on the surface of 304 when exposed to PWR primary water. The outer layer is most commonly accepted to form by a precipitation reaction while the inner layer is formed by a solid state reaction [105,180,183]. The inner/outer oxide interface is the site of the original metal interface [22,183] and oxidation proceeds in-

ward by ingress of oxygen anions through the inner oxide [22, 118, 176, 181, 183–185]. The outer layer is an iron rich oxide, reported as magnetite (Fe_3O_4) [118], nickel enriched magnetite [99, 169, 183, 186], or a ferrite spinel [183] that forms discrete particles that afford no protection to the underlying metal. The inner oxide is a compact chromium rich spinel, close to $FeCr_2O_4$ [169, 182, 183], which protects the underlying metal from further oxidation. The inner layer has been reported as both amorphous [99] and crystalline [178, 179]. A volume change accompanies oxidation: the Pilling-Bedworth ratio or ratio of the volume of the oxide to the volume of the metal is around 2 [104]. Metallic nickel enrichment is often reported at the oxide/metal interface [99, 176] and has also been found to be present as embedded metallic nickel particles within the inner oxide [187]. A schematic of expected oxidation products is shown in Figure 8.1.

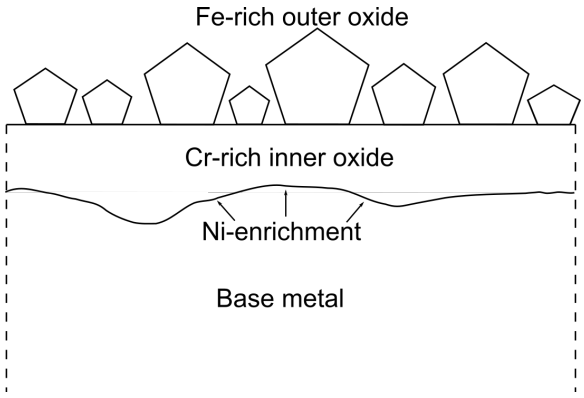

Figure 8.1: Dual layer oxide morphology formed on an austenitic stainless steel in high temperature, high pressure water.

A wide range of parabolic rate constants for 304 in high temperature, high pressure water have been reported in literature: $k_p = 5.23 * 10^{-15} - 4.72 * 10^{-17}$ cm^2/s [118, 186, 188, 189]. Parabolic rate constants are indicative of a diffusion controlled oxidation process, specifically diffusion through the inner oxide. The large range of parabolic rate constants given above is partly due to the effect of near surface deformation.

Surface deformation through surface finishing and plastic strain have both been attributed to altering the oxidation kinetics in this system [16, 116] by creating fast diffusion paths such as dislocation and grain boundaries [15, 24, 115, 117]. Surface finishing is associated with a subsurface deformation zone that can contain nanograins and deformation

bands; the deformation zone depth increasing with increasing deformation induced by surface finishing [16, 22, 24, 116, 117], i.e., a coarser surface finish has a thicker deformation zone depth than a polished surface. The general consensus is that deformation results in faster oxidation [23, 180], although some authors have reported decreased oxidation with more deformation [22, 118]. Increased oxidation with deformation is attributed to deformation features that can provide fast diffusion paths for oxygen anion ingress, while decreased deformation argues that increased diffusion of chromium ions via fast paths and subsequent protective oxide formation is responsible for the decrease in oxide thickness.

Short time oxidation of materials in PWR water is difficult to study as the common testing apparatus contains large water volumes resulting in considerably long heating periods. The transient heating times can exceed the desired exposure time. Due to the difficulty in obtaining controlled short exposure times, results of long exposure times have been extrapolated to short times. In a growing environmentally assisted crack, film rupture results in new material exposure at intervals as low as a few hours, allowing for a large degree of uncertainty in crack behavior.

The work presented in the previous chapters provides insight on the mechanical properties and deformation induced martensite that can occur in 304 at room temperature and at elevated temperatures, as these starting conditions may be present in components when they are placed in service. Air experiments were originally planned to study the effect of surface finish in a high throughput, controlled system, although the low oxide thickness formed in air combined with limitation in quick measurement techniques resulted in abortion of air studies in favor of water studies. Understanding of controlled, short time oxidation behavior, such as that which is present in a growing EAC is necessary to understand the cracking process and form predictive material models of EACs. This study will examine the controlled short time surface oxidation and the effect of material deformation on short time oxidation behavior, similar to conditions that would be present in a growing EAC. Two types of material deformation will be considered: surface finish and plastic strain.

8.2 Experimental Setup

8.2.1 Material

Three heats of 304 SS of composition given in Table 8.1 were investigated in this work. Both heat 2 and heat 3 were investigated in the mill annealed and cold rolled to 20% reduction in thickness starting conditions, and heat 1 was studied only in the mill annealed condition. Uniaxial tension specimens were created after cold rolling a bulk piece of material and prior to exposure to high temperature, high pressure deaerated water.

Table 8.1: Composition of the 304 stainless steel heats.

Heat	C	Mn	P	S	Cr	Ni	N	Fe
1	0.04	1.37	0.023	0.015	18.65	9.37	0.03	Bal
2	0.040	1.46	0.002	0.015	18.39	9.13	0.03	Bal
3	0.040	1.45	0.021	0.016	18.36	9.28	0.03	Bal

8.2.2 Deformation

Plastic Strain

Samples of heat 1 in the mill annealed condition were strained in uniaxial tension to target values of engineering strain, given in Table 8.2, in room temperature air at a rate of 0.0036 mm/s up to 4% strain. After which, the rate was increased to 0.042 mm/s to the final desired strain level before unloading to zero load.

Table 8.2: Plastic strain (%) induced into microstructure.

Plastic Strain %
10, 20, 30, 40, 50, 60

Surface Finish

Two surface finishes were studied on heat 1 with plastic strain given above: machined and mechanically polished. A range of surface finishes were also studied on all three heats. Starting material condition and surface finish studied are given in Table 8.3.

Table 8.3: Surface finishes of the exposed samples.

Heat	Starting Condition	Surface Finish (grit/particle size)
1	Plastic Strain	Machined, 40 nm
	Mill Annealed	Machined, 220, 600, 40 nm
2	Mill Annealed	80, 220, 600, 800, 1200, 40 nm
	20% cold rolled	80, 220, 600, 40 nm
3	Mill Annealed	80, 220, 600, 800, 1200, 40 nm

8.2.3 Exposure

Exposure of all specimens to high temperature, high pressure, hydrogenated water was achieved using a specialized loop system that permits controlled short time exposures; a schematic of the loop is given in Figure 8.2. The water can quickly be changed between a hot water and cold water loop, minimizing the transient heating and cooling times. Samples were exposed in an oxidized zircaloy sample holder to electrically isolate the samples from the components of the loop. Parameters of the exposure are as follows: 290 °C and a volumetric flow rate of $3.6 * 10^{-3}$ m^3/s. The volumetric flow rate present in the loop results in a Reynolds number of $1 * 10^7$, which is in the turbulent flow regime.

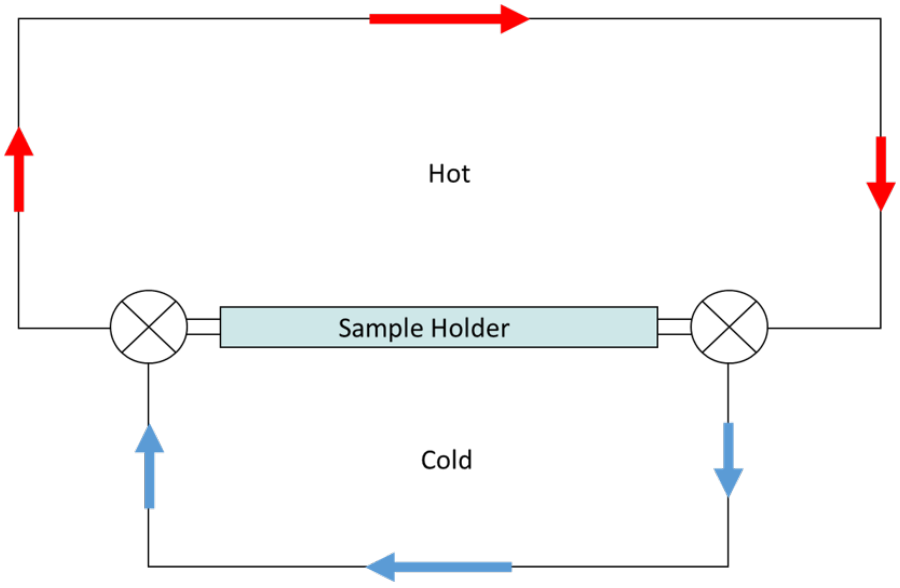

Figure 8.2: Schematic of the specialized loop system at NNL used to expose samples to high temperature, high pressure water.

Tensile specimens of heat 1 with a machined surface finish and plastic strain were exposed for 10, 50, and 100 hours while all other specimens listed in Table 8.3 were exposed for 100 hours.

8.2.4 Characterization

The surface of the exposed samples was imaged using SEM following exposure. A Helios 6600 dual beam PFIB/SEM was used to make cross sections and image the cross sections; analysis of oxides was performed using ImageJ [145]. Oxide thickness measurements were obtained from the cross sections as oxide penetration normal to the inner oxide/solution interface, and TEM and EDS were completed on select exposures to characterize phases present after exposure. Electron channeling contrast imaging using a backscatter electron detector was used to study the subsurface deformation induced by surface finishing procedures after exposure.

8.3 Results

8.3.1 Effects of Plastic Strain

Machined Surface Finish

SEM images of the outer morphology for the machined surface finished samples exposed at 10, 50, and 100 hours are shown in Figure 8.3. Discrete outer particles, present as the bright areas in the SEM image, are apparent for each exposure time. Particle density is non-uniform across the surface; areas of high and low density are present in each exposure. Particle size for the 10 hour exposure in Figure 8.3 is smaller than the 50 or 100 hour exposure; differences between the 50 and 100 hour exposure are not as obvious. A more detailed analysis of particle size is necessary to determine the relationship between particle size and exposure time.

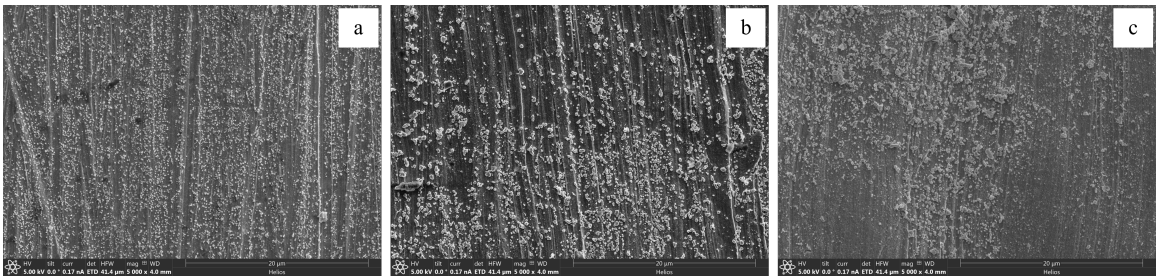

Figure 8.3: Surface SEM images for (a) 10 hours, (b) 50 hours, and (c) 100 hours.

Figure 8.4 shows boxplots of the diameter of the outer surface particles measured for each exposure time with plastic strain, (a), and all of the data for each time combined, (b). No obvious trend is visually evident between plastic strain and particle size at any exposure time. Ordinary least square (OLS) regression for each exposure time confirmed the effect of plastic strain on surface particle diameter is minimal. Increasing exposure time does not always result in an increase in particle diameter; this is readily apparent at 0% plastic strain where the mean particle size decreases with increasing time. Another occurrence can be seen at 20% plastic strain where the majority of the outer particles at 50 hours are larger than the particles present at 100 hours. A large variation in particle diameter is seen at each exposure time, and while the 100 hour exposure had the largest particles measured at any of the three exposure times, the mean particle size is very similar, and slightly less than that at 50 hours.

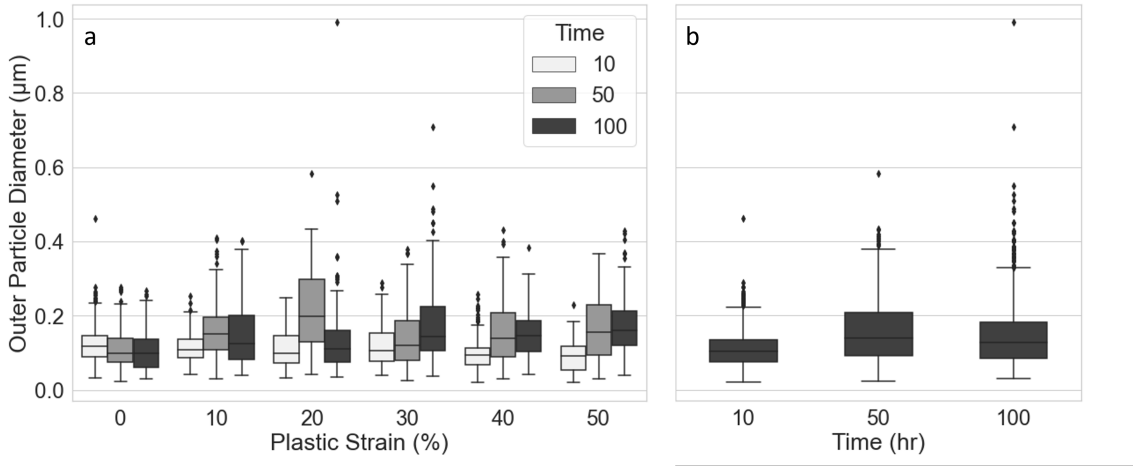

Figure 8.4: Boxplot of outer particle diameter for 10, 50, and 100 hour exposure. Individual exposures for each value of plastic strain are shown in (a) while all the plastic strain values for each time are compiled in (b)

Cross sections created by the PFIB and imaged using SEM for inner oxide thickness analysis are shown in Figure 8.5 for (a) 10, (b) 50, and (c) 100 hours. Two layers of platinum, an inner electron beam and outer ion beam deposited layer, were used to protect the oxide when milling with the ion beam. These two layers are apparent on top of the inner oxide and discrete outer particles as the darker compact and lighter porous layers. The shape of the inner oxide layer mimics that of the machined surface finish, resulting in a curved inner oxide/outer particle or solution interface. The cross sections reveal that the outer particles are similar in gray scale to the platinum, unlikely to be the expected iron-rich oxide which is reported in literature. The dark, inner oxide is mottled with a phase which has a gray scale similar to that of the underlying base metal. The inner oxide does not form a continuous smooth interface with the base metal due to the mottled features. Oxide penetration depth clearly increases with increasing exposure time.

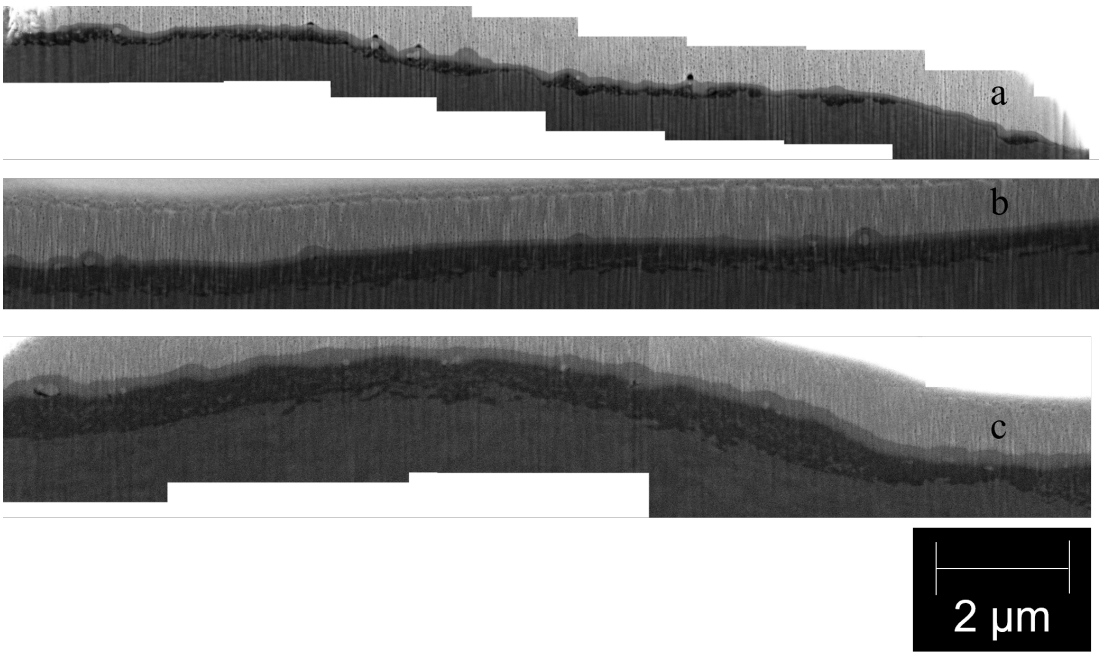

Figure 8.5: Cross sections created with the PFIB and imaged using the SEM at a 52° tilt using the Everhart-Thornley detector at 5 kV and 0.17 nA for (a) 10 hours, (b) 50 hours, and (c) 100 hours.

Boxplots were created for oxide penetration depth measurements normal to the inner oxide/solution interface for (a) each exposure and (b) all of the plastic strain, machined surface finish samples in Figure 8.6. As with the outer surface particles, no obvious trend exists between plastic strain and oxide thickness at any of the times investigated. Unlike the outer particles, there is an increase in oxide thickness/penetration with increasing time. This is evident at each strain level in (a), along with the combined data in (b). OLS regression of the combined data in (b) was used to determine the parabolic rate constant of $7.22 * 10^{-15}$ cm^2/s for inner oxide penetration depth.

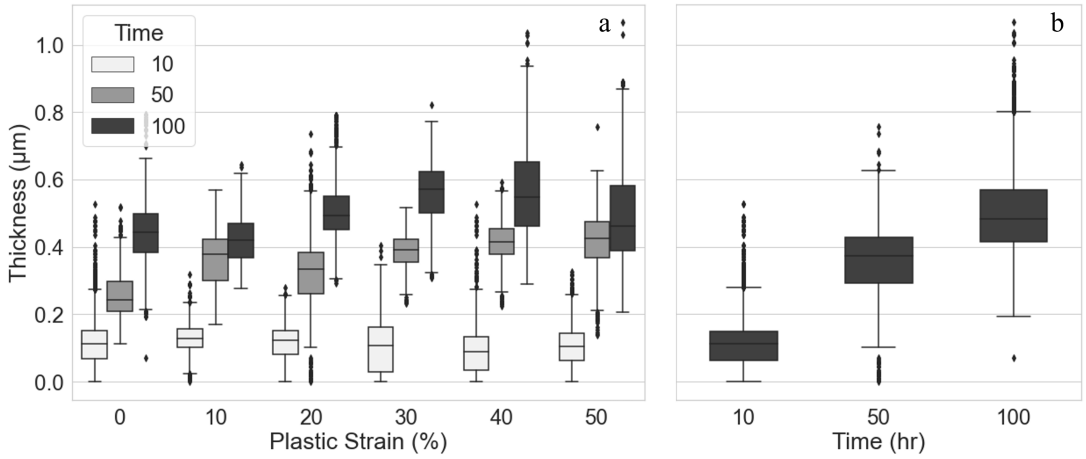

Figure 8.6: Boxplots for all three exposure times with a machined surface finish showing a: all values of plastic strain and b: plastic strain condensed for each time.

TEM of the 30% plastic strain samples at 10, 50, and 100 hours was performed on lift-outs created with the PFIB, using a Themis 200 Probe Cs Super X HRTEM/SETM. EDS phase maps for iron, chromium, nickel, and oxygen were created along with selected area diffraction patterns of the outer particles, inner oxide, and base material in Figure 8.7. EDS phase maps reveal that the outer particles are a nickel rich metallic phase instead of the iron-rich oxide which is reported in literature. The diffraction pattern collected from the nickel-rich particle indicated an FCC microstructure that does not match pure nickel. Small iron rich nodules are present on top of the inner oxide at all exposure times. The diffraction pattern along with composition of the inner oxide suggest a mixed chromium rich spinel phase. The mottled appearance in the inner oxide phase seen in the SEM images is a metallic phase.

Although an outer oxide phase, as is reported in literature, is not present in these exposures, the oxide formed will continue to be referred to as the inner oxide to keep consistency with the inner oxide reported in literature. Inner oxide formed on each exposure time is nano grained and had similar composition that is reported in Table 8.4. The inner oxide is depleted in iron and nickel and has similar chromium composition compared to the base metal.

Table 8.4: Chemical composition (at%) of the outer particles and inner oxide, as determined by EDS.

	Iron	Chromium	Nickel	Oxygen
Outer particles	6.12±1.64	1.78±0.5	87.84±23.97	3.68±1.99
Inner oxide	13.75	20.2	2.14	63.21

At the 10 hour exposure time, the metallic phase forms a connected network which extends through the inner oxide and connects to the underlying base metal. The metallic networks have a similar chemical composition to 304 and retain the morphology of the underlying nanograins that are a result of the machining surface finish. Composition and morphology of the embedded metallic component evolve at longer exposure times. By 50 hours, the metallic components near the inner oxide/solution interface no longer share a similar morphology to nanograins and are potentially entirely embedded within the inner oxide, as connectivity cannot be conclusively determined by TEM. The metallic components near the inner oxide/solution interface have decreased in size and become enriched in nickel compared to the metallic network present at 10 hours. The metallic components near the inner oxide/metal interface continue to have a composition close to 304 with a similar shape and size as the metallic networks present at 10 hours. A similar morphology is present at the 100 hour exposure: the metallic components near the oxide/metal interface are similar in composition to 304 and connected to the base metal while metallic particles rich in nickel are embedded in the oxide moving towards the oxide/solution interface.

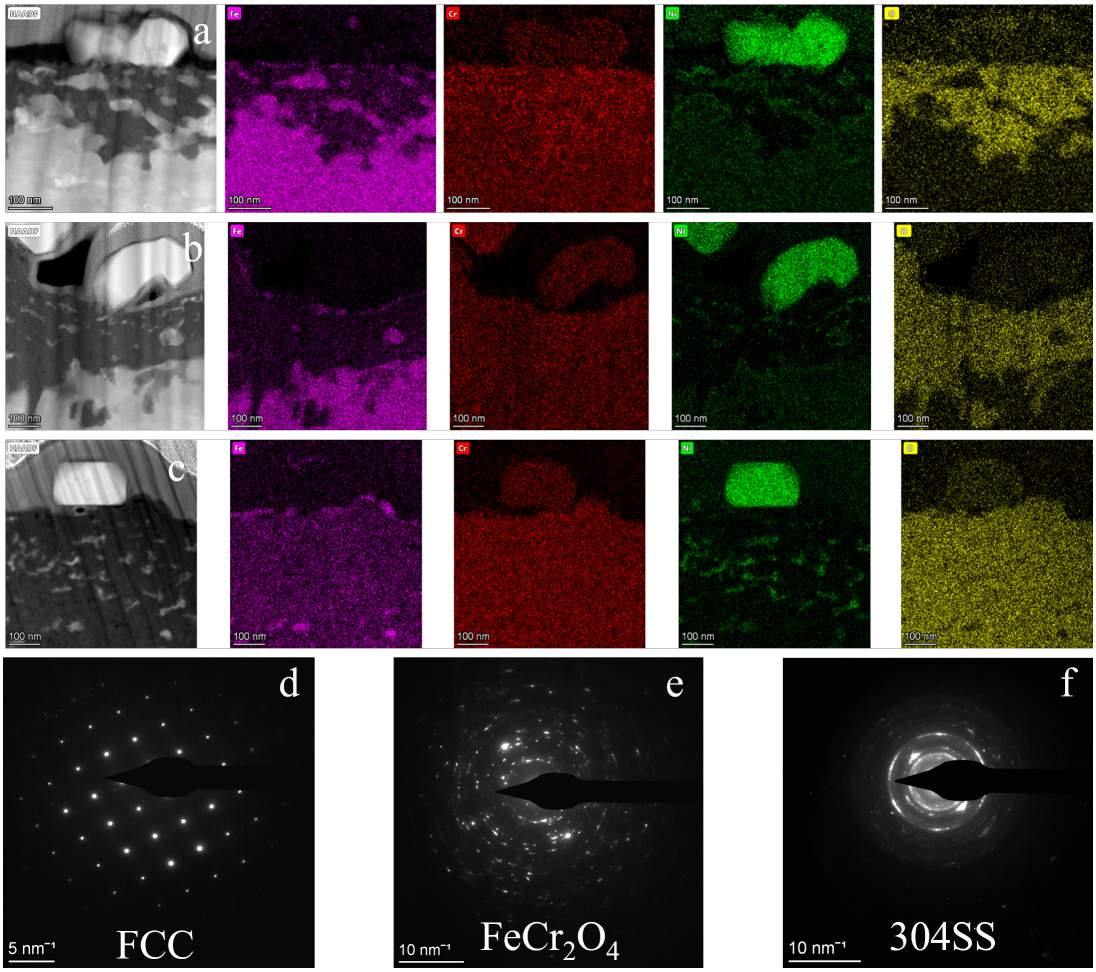

Figure 8.7: TEM EDS of 30% plastic strain exposed for a: 10, b: 50, and c: 100 hours, and selected area diffraction patterns for d: outer particle, e: inner oxide, and f: base metal.

Polished surface finish

SEM images of the outer surface morphology are given in Figure 8.8 at two different magnifications; yellow dashed lines in (a) are at the locations of twin boundaries and a grain boundary is highlighted by the blue dashed line. Discrete particles, similar to those seen in the machined surface finish, are present primarily on top of a semi continuous layer. As with the outer particles present on the machined surface finish, the gray scale of these two layers is lighter than the darker layer on which they formed, which can clearly be seen in the top right corner of Figure 8.8b. The semi-continuous layer morphology is related to the underlying microstructure, as can be seen by the difference in morphology across grain/twin boundaries.

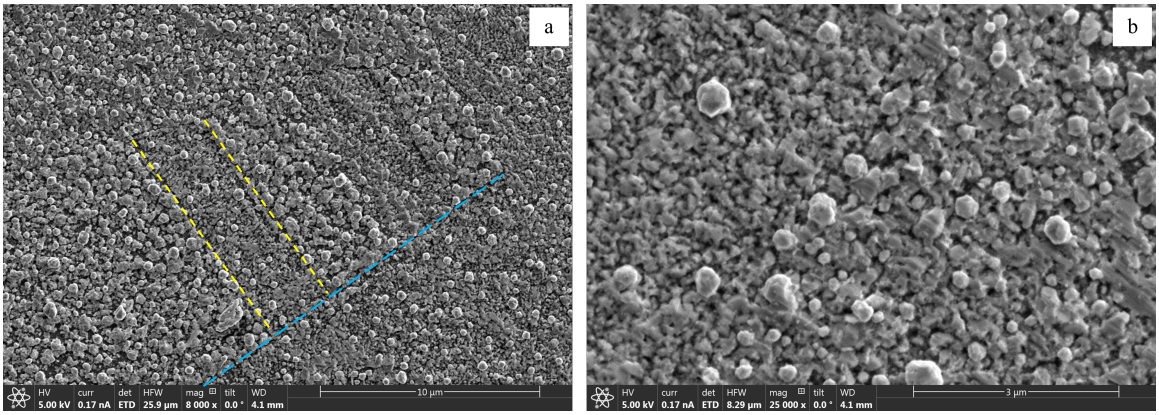

Figure 8.8: Surface after oxidation for 100 hours at (a) 8000x and (b) 25000x. Yellow dashed lines show twin boundaries and the blue dashed line is located at a grain boundary

A cross section of one exposure created with the PFIB and imaged using SEM is shown in Figure 8.9. As before, two layers of platinum are deposited, an inner e-beam deposited and an outer i-beam deposited layer, to protect the surface during the ion milling. The discrete particles and semi-continuous layer seen in Figure 8.8, with gray scales similar to that of the ion deposited platinum layer, are present atop a thick inner oxide layer. Embedded particles, highlighted by arrows in Figure 8.9, with a similar gray scale to the underlying 304, are present in the inner oxide in all cross sections.

The inner oxide/solution/particle interface is much smoother as compared to the machined surface finish. The polished specimens had a planar surface finish resulting in this oxide morphology.

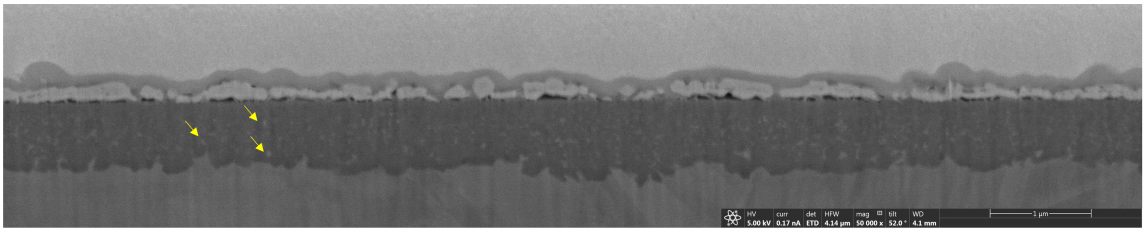

Figure 8.9: Cross section of an exposed specimen using the PFIB and imaged using SEM. Embedded metallic particles in the inner oxide layer are highlighted with arrows

Oxide thickness, which is measured as maximum oxide penetration normal to the inner oxide/solution interface, is plotted in Figure 8.10. Strain has little effect on oxide penetration depths at low strain levels ($\leq$ 30 % plastic strain). Increasing plastic strain beyond 30% plastic strain resulted in a decrease in oxide penetration. The data was split into two

data sets: low strain (< 40%) and high strain (> 40%) to investigate this behavior that is apparent in the boxplot. Ordinary least squares was completed on the low strain and high strain groups. The relationship was confirmed that at low levels of plastic strain, increasing strain led to a small increase in oxide penetration. At high values of strain, the oxide penetration decreased with increasing plastic strain.

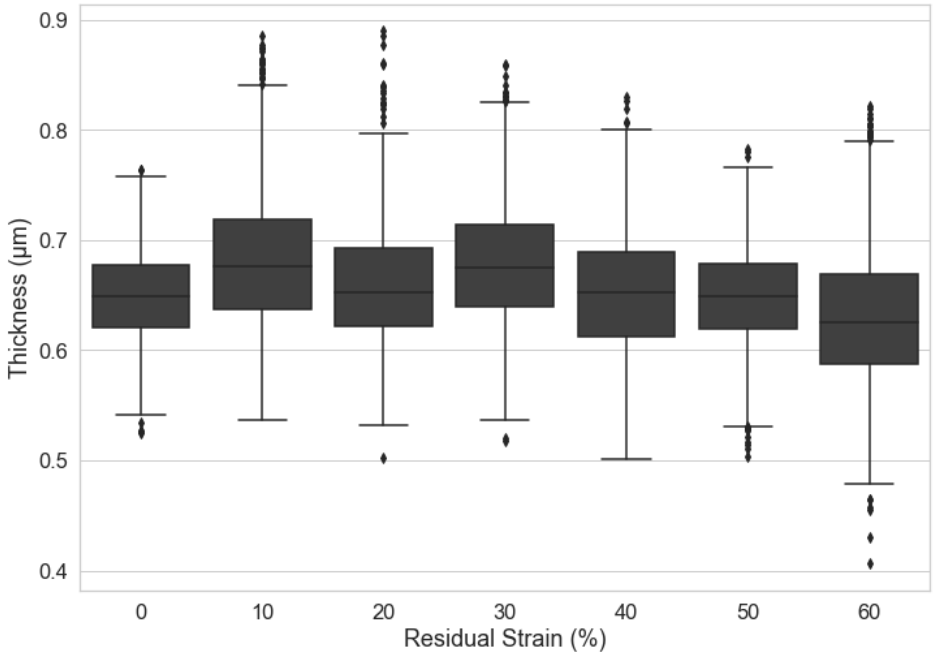

Figure 8.10: Boxplots showing the oxide penetration (inner oxide thickness) for each strain level of the polished surface finish exposed for 100 hours.

TEM of a polished surface exposed for 100 hours is shown in Figure 8.11. Deeper oxide penetrations are protruding down deformation present in the starting material condition. TEM-EDS results are consistent with those reported for the machined surface finish. Both the discrete outer particles and the semi continuous layer are nickel rich metallic layers. The inner oxide is consistent with a chromium rich spinel, and the embedded particles are metallic. As with the 100 hour exposure of the machined surface finish, the embedded particles close to the inner oxide/outer layer interface are more nickel enriched compared to 304 while the particles close to the inner oxide/metal interface have a similar composition to 304. Non-uniformity of grayscale is evident in the inner oxide phase. HAADF is sensitive

to density and atomic weight, suggesting that the inner oxide maybe be inhomogeneous.

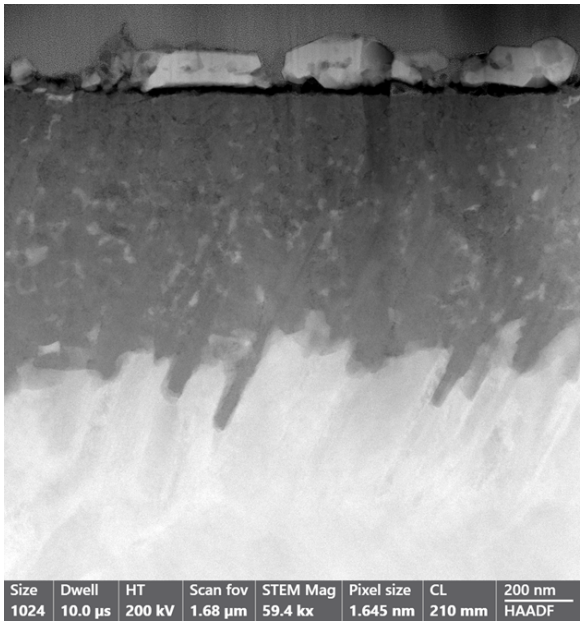

Figure 8.11: HAADF TEM of polished surface exposed for 100 hours.

8.3.2 Effects of Surface Finish

Morphology of outer particles follow a similar trend seen in the machined and polished samples with plastic strain: a finer surface finish promoted a more semi-continuous layer while a coarser surface had more discrete particles. SEM images of the heat 3 surfaces for all surface finishes are given in Figure 8.12. The three coarsest surface finishes, 80 grit, 220 grit, and 600 grit, have mostly discrete particles with some areas of high coverage and other areas (not shown) with little to no outer particles present. At 800 grit, the coverage becomes more continuous; the semi-continuous layer is present in areas of the 1200 grit and fully developed at the 40 nm surface finish.

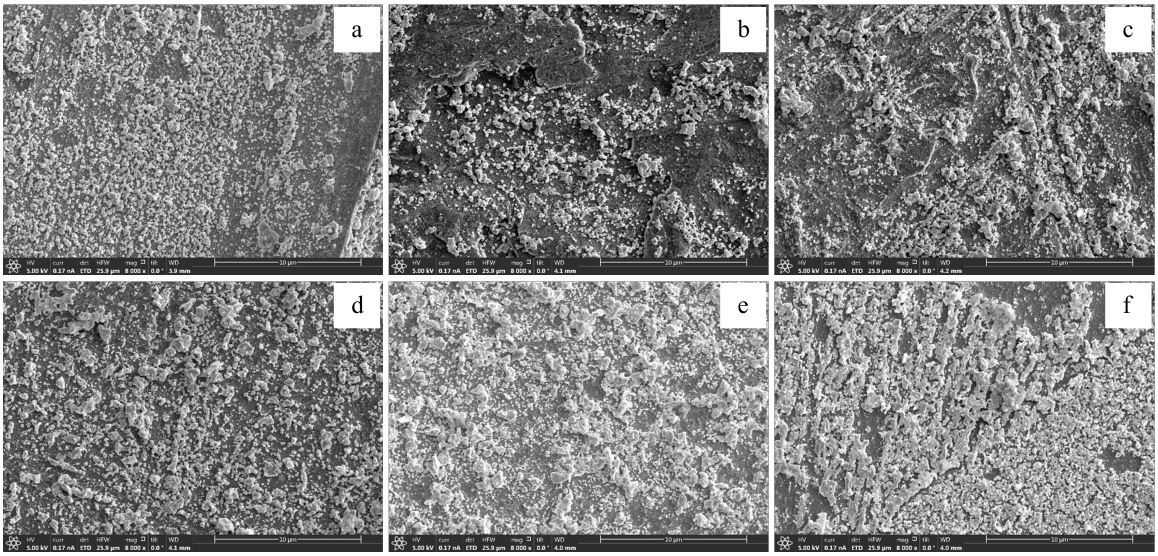

Figure 8.12: Surface morphology with surface finish after 100 hour exposure for (a) 80 grit, (b) 220 grit, (c) 600 grit, (d) 800 grit, (e) 1200 grit, and (f) 40 nm.

A more pronounced effect on surface finish is seen in the inner oxide penetration depth. A boxplot showing inner oxide thickness with the different surface finishes is shown in Figure 8.13, and surface finish, as quantified by finishing particle size, is plotted against the oxide penetration depth in Figure 8.14. Table 8.5 shows the grit size and finishing particle size relationship. Oxide penetration depth increases rapidly at the finer surface finishes and little effect is seen with the coarser finishes. Increasing coarseness above approximately 800 grit has little effect on oxide penetration depth. Cold rolling also does not show a pronounced effect on oxide thickness for these exposures. A power law fits the average oxide thickness versus finishing particle size relationship quite well.

Subsurface deformation was evaluated by cross sections using ECCI. Subsurface deformation after exposure was found to be present on the 80 grit and 220 grit finished samples only at depth of around 6 μm and 3μm, respectively. No evidence of subsurface deformation below the inner oxide layer was present for the mechanically polished surface or the samples ground finer than 220 grit. This is shown as the gray shaded region in Figure 8.14.

Table 8.5: Composition of the 304 stainless steel heats.

Grit Size	Particle Size (μm)
80	180
220	53
600	10.6
800	7.8
1200	3.8
40 nm	0.04

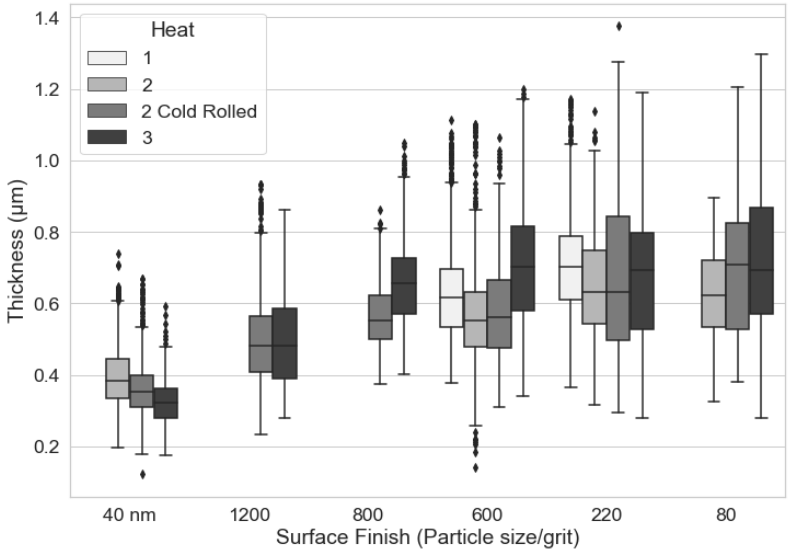

Figure 8.13: Boxplot showing the oxide penetration for each heat starting material condition (mill annealed and cold rolled) and surface finish exposed for 100 hours.

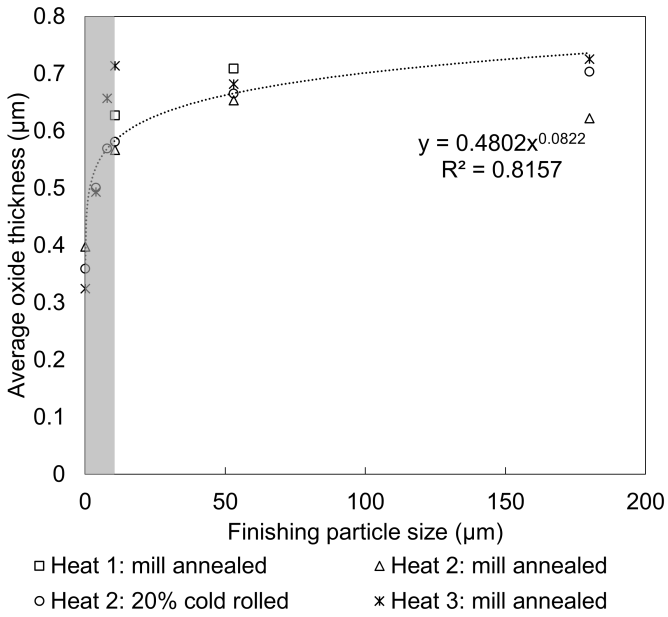

Figure 8.14: Mean oxide thickness plotted against mean particle size for each surface finishing; the area shaded in gray denotes the finishing particle sizes that results in consumption of the deformation layer formed during oxidation.

8.4 Discussion

Oxidation of austenitic stainless steels in high temperature water is extensively studied. A dual oxide layer forms with a non-protective iron-rich outer layer and compact, continuous chromium rich inner oxide that provides protection to further oxidation [169]. The inner layer grows via oxygen ingress while the outer oxide is most commonly accepted to form via precipitation of iron rejected into solution from the growing inner oxide. The current study did not show similar oxidation behavior to that reported in the literature.

An inner, chromium rich oxide, and an outer phase containing nickel rich metallic particles are present at all exposure conditions. A material balance of iron, chromium, nickel, and manganese in the starting 304 and in the inner oxide, where the inner oxide composition is determined from EDS scans, is given in Equation 8.1. All of the chromium in the oxidized metal is incorporated into the inner oxide. Iron and manganese in excess of that contained within the inner oxide is released to solution while the nickel not incorporated into the inner oxide is contained in the outer nickel rich particles.

$$x\mathrm{Fe_{69}Cr_{20}Ni_9Mn_2} + 63x\mathrm{O} \rightarrow x\mathrm{Fe_{14}Cr_{20}Ni_2MnO_{63}} + 55x\mathrm{Fe} + 7x\mathrm{Ni} + x\mathrm{Mn} \quad (8.1)$$

8.4.1 Thermodynamically stable phases

Metallic nickel rich particles are not reported to form in literature, where most of the testing is performed in autoclaves. Nickel, the most stable major alloying element of 304, does not fully oxidize in the environment present, and has been reported to form in the inner oxide as embedded metallic particles [187], although nickel enrichment is normally reported to occur at the inner oxide/metal interface.

As discussed previously, autoclaves contain large volumes of water with slow heating times. Flow in an autoclave system is also nearly static and only enough to maintain temperature and chemistry requirements in the system, while the loop system has a very short heating time with a high flow rate.

A Pourbaix diagram for 304 in water of the desired chemistry at pressure and temperature is evaluated to determine the thermodynamically stable phases in the system. The major alloying elements present in 304: Fe, Cr, and Ni, are considered available to participate in electrochemical reactions. A Pourbaix diagram for all three species reacting on a 304 surface are overlayed and shown in Figure 8.15, with the region of metallic nickel stability shaded. The natural pH of the system is shown by the vertical dashed line and the corrosion potential of the system is given by the open circle on the natural pH line. The system lies at a pH and potential at the water stability line with hydrogen. Only metallic nickel is stable as iron and chromium are only stable in oxidized forms. While not reported in the literature, metallic nickel is a thermodynamically stable phase.

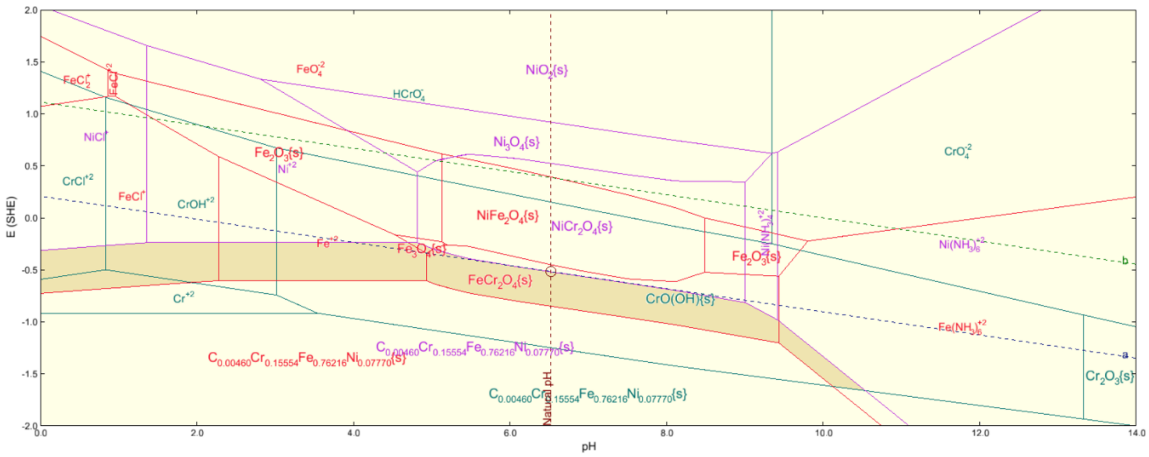

Figure 8.15: Pourbaix diagram for iron, chromium, and nickel on a 304 SS surface.

A few differences are apparent between autoclave systems and the loop system studied in this test. First, the transient heat up time in an autoclave system is much longer; the sample is exposed to a large range of temperatures that may promote formation of a precursor to the formation of the iron rich oxides. Second, controlled short time exposures are difficult to achieve, meaning that exposure time may actually be longer than is reported in literature. Finally, the flow rate in the autoclave is very low, maintaining a nearly static environment near the sample surface while the high flow in the loop is turbulent.

Transient heating time could account for the presence of either the iron rich oxides or the nickel rich particles if there are differences in stability of either product with slow or fast heating profiles. This effect was studied in OLI Systems [190]; starting water chemistry and pressure were held constant while the temperature was increased. Stability of oxidation products showed very little dependency in the temperature range expected in an autoclave system. Presence or absence of the nickel rich particles and the outer iron rich oxide is unlikely to be an effect of the transient heating time.

Large water volumes not only lead to long heat up times, but also long cool down times, making controlled short time exposures very difficult if not impossible to achieve with an autoclave. A small body of literature exists for short time exposures using other testing apparatus [169, 179]. These studies indicate that iron rich oxides form on the surface of the inner oxide. Cracking studies also indicate the presence of an iron rich oxide [15]. In all of these studies, little nickel is present in the inner or outer oxide but found as nickel

enrichment at the inner oxide/metal interface [15, 99]. The short time exposures present in the loop are not likely to be the origin of nickel rich particles on the surface.

The final major difference between autoclave systems and the loop system is flow; the flow in the loop system is very high resulting in a turbulent flow, while the flow present in an autoclave is laminar and nearly static. In laminar flow systems, a thick boundary layer can develop allowing for a buildup of aqueous oxidation products near the metal surface and at distances into the solution. Highly turbulent flow can prevent this buildup by decreasing the boundary layer thickness, quickly removing oxidation products from the near surface. At the flow rates for the system, the iron ions released into solution by the growing inner oxide are quickly removed from the near surface. A critical concentration of iron required for iron precipitation will never be met and the iron rich oxides will not be able to form.

Metallic Nickel Stability

The effect of iron concentration in solution on metallic nickel stability in the environment of interest was studied using OLI Systems [190]. The Pourbaix diagram in Figure 8.15 created for a 304 surface is calculated assuming 10^{-6} M of iron, chromium, and nickel in solution. This is not representative of conditions present in the loop because the high flow prevents a buildup of concentration of any ion in solution, and aqueous chromium ions are not expected to be in a significant concentration since the majority of chromium is expected to be oxidized in the inner oxide. A series of Pourbaix diagrams were calculated to study the effect of aqueous iron on metallic nickel stability, and the Pourbaix diagram is given in Figure 8.16 with a maximum of $8 * 10^{-9}$ M iron ions in solution was determined for metallic nickel stability. Iron ions in excess results in nickel being stable as $NiFe_2O_4$, which is reported to form in autoclave setups [99, 169, 186].

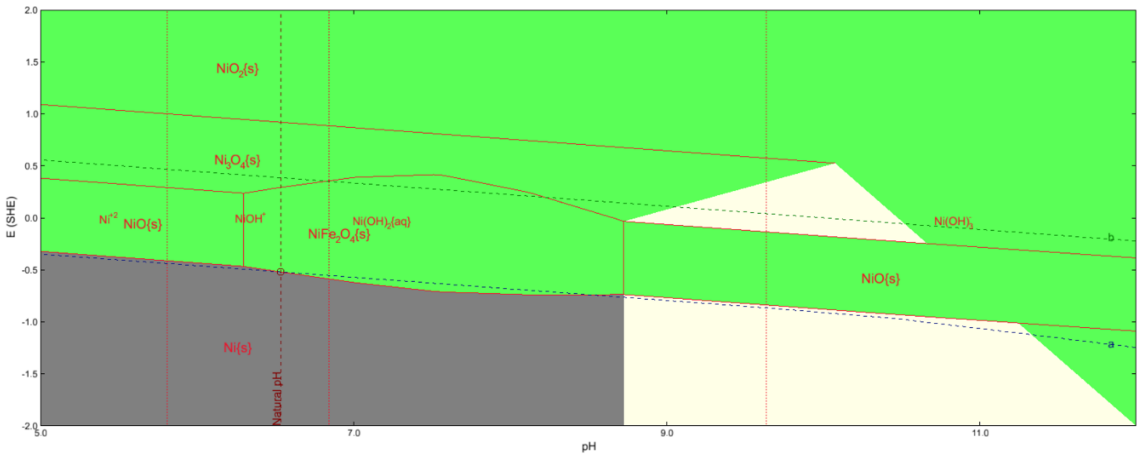

Figure 8.16: Pourbaix diagram for iron, chromium, and nickel on a 304 SS surface.

The low solution flow rate in an autoclave system leads to a large boundary layer thickness thereby allowing a larger ionic concentration near the surface of ions released to solution from oxidized metal. The boundary layer thickness required to ensure the minimum iron concentration for formation of an iron rich oxide is easily met in an autoclave. Absence of nickel rich metallic particles can easily be explained even though metallic nickel is predicted to be stable based on the 304 Pourbaix diagram. In the loop system, which is in the turbulent flow regime and the near surface iron solution concentration is expected to be close to bulk. The low near surface concentration not only prevents iron precipitation to form iron rich outer oxide but also allows for metallic nickel particles in place of the outer oxide. Formation of the nickel rich particles likely occurs via a solid state reaction. Absence of the iron rich oxide and stability of nickel rich metallic phase is a direct result of the flow conditions present in the loop.

8.4.2 Short Time Oxidation Mechanism in a Loop Environment

Grain boundaries and dislocations present in the metal at the surface provide fast diffusion paths for oxygen anion ingress and metal cation egress. Upon exposure, oxidation proceeds down fast diffusion paths, preferentially oxidizing these areas and rejecting iron into solution. The chromium oxidizes in place in the inner oxide, as confirmed by the material balance for the system. Oxygen concentration in the water is very low and oxygen must be supplied by the reduction of water.

Fast diffusion paths are attacked more harshly in the loop setup leaving a similar metallic network morphology and a porous inner oxide that has been reported for dealloying, selective oxidation, and internal oxidation [95, 191–193]. Inner oxide growth requires oxygen anions to diffuse through the inner oxide and iron ions to diffuse out of the inner oxide to maintain the approximately doubling of volume accompanying oxidation [104]. Lateral growth of the oxide leaves a metallic phase embedded in the inner oxide. At short times, the metallic phase forms a continuous network through the entire inner oxide while increasing exposure time results in oxidation of the network near the oxide/solution interface. Surface nickel particles are also present on the inner oxide/solution interface with a notable absence of a continuous outer oxide phase.

Stability of the metallic nickel rich phase in solution was confirmed by the lack of iron ions in solution, although further consideration must be made for the presence of these particles. The majority of nickel in the base 304 is rejected from oxidation, based on the electrochemical stability of nickel and the low nickel content of the inner oxide phase. Coverage of the surface by iron rich oxides provided a constraint to where the nickel could enrich in the low flow system resulting in nickel enrichment at the oxide/metal interface. This constraint is not present in the high flow systems, and nickel particles can now grow into the solution. As with aqueous iron, aqueous nickel would also be removed from the near surface solution due to the high flow in the loop. For the nickel rich particles to grow, growth must be via a solid state reaction, and nickel must be provided to the particles from the base metal for further growth to proceed.

Inner oxide thickness follows a parabolic growth rate, while the outer nickel rich particles have a peak mean size at 50 hours. A parabolic growth rate is indicative of oxidation following diffusion control through the inner oxide. Diffusion controlling mechanisms in the inner oxide can be broken into

1. Lattice diffusion through the oxide via cation/anion defects
2. Diffusion via oxide grain boundaries
3. Diffusion through microstructural features

The high oxide growth rate of the loop samples as compared to the values reported in literature indicate that lattice diffusion is not rate controlling for these oxide growth rates and will not be considered as the rate controlling mechanism.

A number of unique features accompany the short time oxidation behavior of 304 in the loop system: presence of the nickel rich outer oxides with simultaneous absence of iron rich oxide, presence of metallic networks embedded in the inner oxide, and inner oxide porosity. All of these features can enhance oxidation kinetics determined in the loop, as compared to literature autoclave results. Each feature and its effect on enhancement of diffusion kinetics will be considered separately in the following sections along with a mechanism that can explain a number of features.

Increased Oxidation Rates via Grain Boundary Diffusion

Some authors have proposed that oxide grain boundaries can act as fast diffusion paths leading to increased oxidation kinetics [97,104,194]. An epitaxial orientation relationship is reported to exist between the austenite and inner oxide leading to a similar grain size before and after oxidation [22,95,96,195]. Nanograins created by surface finishing procedures would result in nanograined inner oxides. The SAED patterns collected from the inner oxide for the machine finishes at 10, 50 and 100 hour exposures confirm that the inner oxide grain size is less than 100 nm.

Values for cation and anion diffusivities in a chromium rich spinel of the composition that would be formed in high temperature water vary up to 5 orders of magnitude between different reports [196,197]. Little confidence can be placed in the actual values of diffusivity, although grain boundaries are known to have increased diffusion kinetics as compared to bulk [198]. The small oxide grain size combined with the increase in diffusivity in the grain boundaries versus the bulk could explain the increase in oxidation kinetics seen in the loop experiments.

Two complexities arise with the consideration of oxide grain boundaries as rate controlling for enhanced oxidation. The first is that at the relatively low temperatures tested, the diffusivity through the grain boundaries is still expected to be too low to account for oxidation. Second, fine grains have been reported in other studies and have been credited

for lower oxidation by enhanced chromium diffusivity leading to a more protective inner oxide [22, 93].

Increased Oxidation Rates via Metallic Networks

Fast diffusion and oxidation along enhanced diffusion paths followed by slower lateral growth of the oxide results in metallic networks that form a continuous channel that reaches through the inner oxide to the base metal at short exposure times. The metallic networks extend to the base metal effectively reducing the diffusion distance through the inner oxide. In addition to decreasing the effective diffusion distance, the networks simultaneously provide fast diffusion paths relative to oxide lattice diffusion by the oxide/metal interface along with increased diffusion in the metal.

At the 10 hour exposure, the metallic networks are continuous and extend from the base metal to near the oxide/solution interface. The effective diffusion distance through the inner oxide decreases the reach of the metallic networks. Values of diffusivity of cationic and anionic species along the metal/oxide interface are not available, although expected to be closer to grain boundary diffusion than lattice diffusion. Fast diffusion of species along the oxide/metallic network interface can result in increase in oxidation kinetics. These networks are not stable, increasing exposure time results in oxidation of iron and chromium in the networks at locations near the oxide/solution interface. Metallic nickel rich particles are left in the location of the original metallic network after the iron and chromium components are selectively oxidized. This is seen at 50 and 100 hours: the metallic components near the oxide/solution interface are nickel rich and unlikely connected to the base metal. Networks are still present closer to the oxide/metal interface maintaining the decreased effective diffusion distance compared to oxide diffusion.

Enhanced diffusivity within the metallic component also needs to be considered as a contributor to the increased oxidation rate. Metal and oxygen diffusion within the metallic phase are reported to be higher than those in a chromium rich spinel phase [199–201]. A large excess of iron is confirmed to leave the base metal/inner oxide and go into solution. The large amount of iron leaving the system results in iron vacancies left in the metal. Diffusivity in the metallic phase may be further increased by the large iron vacancy concentration in

the metal. This allows fast diffusion within the base metal by means of vacancies injected into the metal by exodus of iron during oxidation. Vacancy injection and faster diffusion that accompanies it may be the means for nickel diffusion to the outer nickel rich particles.

The metallic networks provide nickel to the growing outer nickel rich metallic phase, which are composed entirely from nickel that was originally in the base metal. Nickel does not readily oxidize, nor does it diffuse quickly through either a spinel oxide or the base austenitic microstructure. Enhanced diffusivity of the nickel to the surface by the metallic networks enables the metallic nickel particles to grow.

Mean size of the nickel rich particles peaks at 50 hours, while the inner oxide continues to grow. Growth of the nickel particles necessitates diffusion of nickel out of the base 304 and into the growing particle. The connectivity of the metallic networks embedded in the inner oxide is confirmed only at 10 hours. While the connectivity cannot be excluded with certainty at 50 hours, the number of networks has decreased. The metallic rich networks provide a fast diffusion path for nickel metal from the base 304 to the growing outer particles. When this fast diffusion path of nickel metal out of the base metal is interrupted, the nickel particles will cease to increase in size. A few connected networks may remain at large times leading to individual particles continuing to grow at longer times. The metallic networks not only provide fast diffusion paths for nickel metal, but other diffusing species within the system.

Increased Oxidation Rates via Nickel Rich Particles

A shift in the electrochemical state of the system is expected when forming metallic nickel rich phase instead of the normally formed iron rich oxide. When two dissimilar metals are connected, formation of a galvanic couple can occur. In the loop oxidation, nickel and 304 are separated by the electrically conductive inner oxide. Nickel is more stable than either iron or chromium; nickel rich alloys are more noble than 304 in the system. The nickel will likely behave as the cathode and the 304 the anode in the galvanic couple. This can result in further oxidation of the 304 while protecting the nickel particles from oxidation.

Increased Oxidation Rates via Vacancy Cluster Formation

A recent study of an austenitic steel in a steam environment reported similar behavior with an interpenetrating metal and inner oxide phase [95] cited a vacancy clustering mechanism that may be able to explain the enhanced oxidation behavior in this study [202]. Vacancy clusters promoted via protons created during water dissociation were responsible for formation of pores in the oxide [202]. The mechanism of oxidation was determined to be internal oxidation. Nanopores present in the inner oxide can increase oxidation by increasing the oxygen anion and cation diffusivities in the inner oxide by movement through the pores by water potentially being present in the pores.

The fast diffusion paths present at the surface at the initial exposure time preferentially oxidize. The nickel rich particles on the surface change the electrochemical behavior of the system; the nickel will act as a cathode and the 304 the anode. With the shift in electrochemical behavior of the system, water reduction and thereby formation of protons will be enhanced in the loop system resulting in a higher proton concentration in the inner oxide. Protons have been shown to create and cluster cation and anion vacancies leading to a porous structure.

Examination of the HAADF images of the inner oxide reveal variation in grayscale, which can be inferred as varying density in the inner oxide and the presence of pores. Pores can increase the diffusion by providing an interface which allows faster diffusion of cations/anions than would otherwise be present, or by allowing water diffusion through the pores. Either mechanism has the ability to increase the diffusivity enough to account for the increase in oxide penetration seen in the loop tests.

Large enough pores have been suggested to increase ion transport by water within the pores [95]. The pores, if absent of water could also increase species diffusivity by a surface diffusion mechanism. Presence of pores, with preferential transport will allow the metallic networks to form and remain unoxidized at short exposure times. The metallic networks are important for supplying nickel out of the inner oxide/base metal system.

Selective oxidation/dealloying/internal oxidation could not be determined with these exposures. Similarities are noted between the oxidation behavior observed here and that of

breakaway oxidation of 304 in steam environments.

A schematic including all of the enhanced oxidation mechanisms is given in Figure 8.17. Oxidation begins down fast diffusion paths, followed by lateral growth. Metallic networks are left embedded in the inner oxide at longer times.

8.4.3 Effect of material deformation

As discussed in detail in the previous sections, short time oxidation proceeds down fast diffusion paths present in the metal including grain boundaries and dislocation microstructures, such as dislocation bundles. Grain boundaries, from deformation induced martensite, and dislocation microstructures are a function of prior material condition. Anything that alters the near surface microstructure by increasing the preferential diffusion paths has the ability to alter the oxidation behavior in high temperature, high pressure water. Two types of deformation considered in the study: plastic strain and surface finish both alter the near surface microstructure present and have the ability to produce a combined effect that may not be possible to be entirely separated from one another.

Although not mutually exclusive, the effect of plastic strain and surface finish will be considered separately in the following sections.

Plastic strain

Increasing plastic strain results in an increase in deformation structures such as dislocations, mechanical twins, and deformation induced martensite, which were discussed in detail in previous chapters. These features can increase oxidation by increasing fast diffusion paths in the metal.

No effect of plastic strain was seen in the machine finished samples, so the effect of plastic strain will be constrained to the polished surface finish samples. The boxplots showed a decrease in oxide thickness at high values of strain but any relationship between strain and oxide thickness was not obvious from the boxplot alone. To investigate the relationship between strain and oxide thickness, the data set was separated into two groups: low and high plastic strain (cutoff at 40 % plastic strain) and a linear regression was fit to the data. No correlation between oxide thickness and plastic strain was determined at low levels of

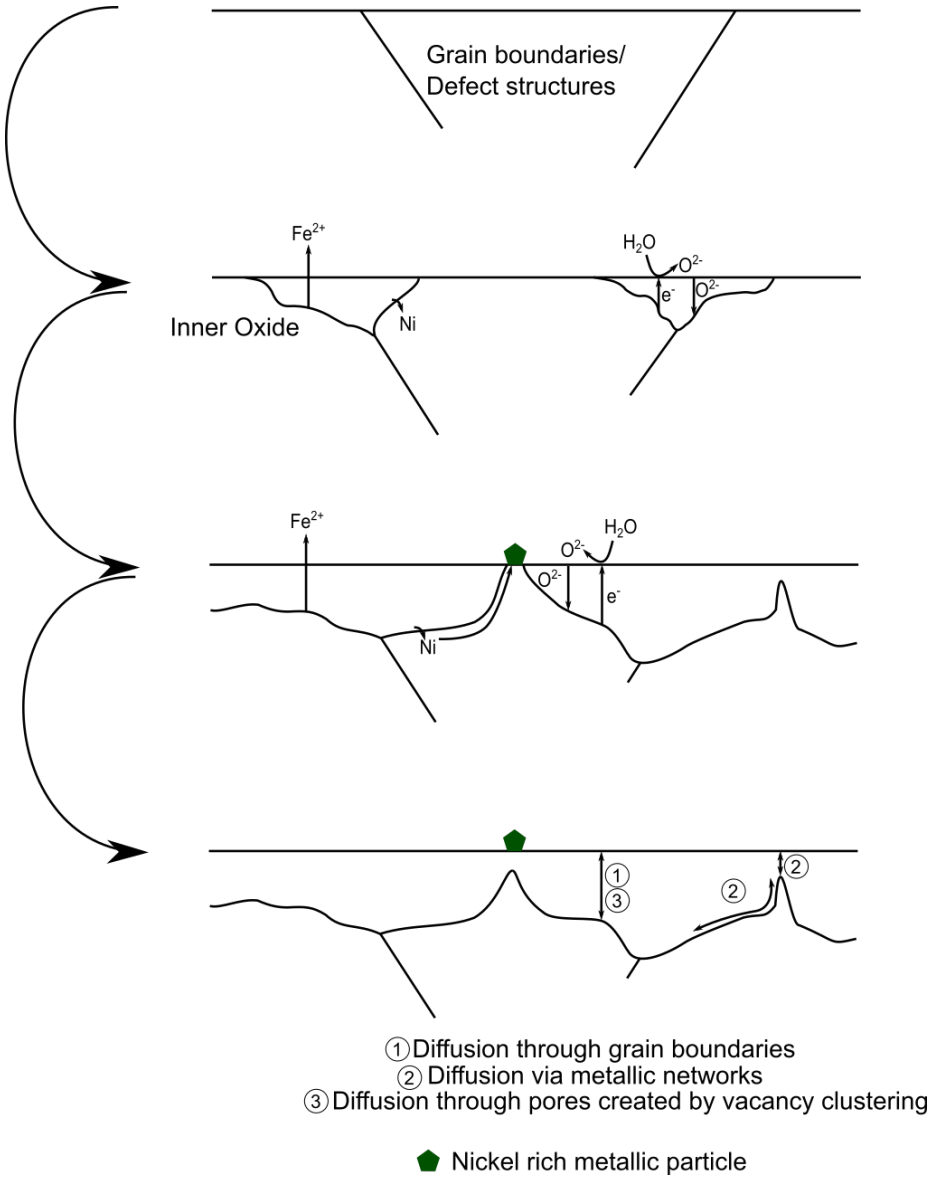

Figure 8.17: Oxidation in a low flow and high flow i.e., loop environments

plastic strain, although a decrease in oxide depth at higher levels of strain was confirmed.

The relationship between strain and oxide penetration depth can be informed by considering the deformation of the steel. Local misorientation, or misorientation between a pixel and its neighboring pixel, measured by EBSD was reported in Chapter 5 in Figure 5.12 and Figure 5.13. A linear relationship between local misorientation and plastic strain is apparent in Figure 5.13. More local misorientation is shown by progressively more green with increasing strain. Around 45 % strain, areas with a high concentration of local misorientation are present, which go away with increasing plastic strain due to martensite consuming the highly deformed areas. Martensite is shown as the solid, light blue areas. Martensite can be nucleated at deformation structures which can then consume the deformation microstructures during formation.

Martensite increases with increasing strain as shown in Figure 5.14, going from a gradual increase to a sharp increase. Oxide penetration depth, as determined by the cross sections, decreased with increasing plastic strain above 40%. This is in the region of sharply increasing deformation induced martensite with increasing strain.

At low levels of plastic strain, the effect of surface finish dominates the oxidation behavior, even though the deformation structures in the microstructure are increasing. At high levels of plastic strain, the oxide penetration depth decreases due to the consumption of the deformation microstructures by formation of deformation induced martensite. Both deformation microstructures created by the straining and surface finishing can act as nucleation sites for martensite formation.

The effect of plastic strain cannot be divorced from that of surface finish as both strain and surface finish have a combined effect by both producing fast diffusion paths near the surface. This is evident from both the machined and mechanically polished surface finish where the effect of plastic strain was not seen at any strain level for the mechanically polished surfaces and the surface finish dominated the effect of plastic strain at low levels of strain for the mechanically polished surface. The effect of surface finish can be studied when the starting material condition is similar among samples.

Surface finish

Oxide penetration depth increases with increasing coarseness of finishing particle size for all heats and starting conditions exposed to high temperature water. The oxide thickness increases most rapidly at the fine surface finishes while increasing coarseness beyond 220 grit results in little effect on oxide thickness. Similar to plastic strain, surface finishing procedures result in an increase in dislocations and other deformation microstructures and can cause deformation induced martensite near the surface [22, 24, 115, 116]. Deformation microstructures and martensite grain boundaries act as fast diffusion paths for oxide penetration while martensite consumes deformation microstructures during transformation [15, 24, 115, 117].

A subsurface deformation zone accompanies all surface finishing procedures, with a thicker subsurface deformation zone created by coarser surface finishing procedures [16, 24, 117]. The deformation induced during surface finishing is at the surface and superficial depths of the microstructure, where oxidation is occurring during exposure.

Subsurface deformation was found to be present on the 80 grit and 220 grit samples after exposure, with the 80 grit sample having a thicker deformed zone than the 220 grit surface. No evidence of a deformed subsurface layer was found for the finer surface finishes after oxidation. The material contained in the deformed layer on the finer surface finishes was completely consumed during oxidation, resulting in no deformed layer present below the inner oxide after oxidation. The rapid increase in oxide penetration at the fine surface finishes is due to the increase in the deformation zone depth. On the fine surface finishes, oxidation proceeds all the way through the deformed layer, slowing as the fast diffusion paths in the metal decrease to the level present in the base metal. On the coarser surface finishes, the deformation zone depth exceeds that of the oxidation penetration depth, the deformed layer is not limiting the oxide penetration depth resulting in a leveling off of the oxide thickness. The coarser surface finishes may also contain martensite which can consume fast diffusion paths during transformation, although this was not directly observed in this study. The deformed layers present likely have enough fast diffusion paths that the consumption of defect structures by deformation induced martensite is unlikely to have a large effect on

the overall oxidation kinetics.

Deformation zone depth beyond the oxidation front is not expected to alter the oxidation behavior in a significant way; for the coarsest surface finishes studied, this appears to hold true: the increase in oxidation depth between 220 and 80 grit surfaces was insignificant. At the finer surface finishes, the oxidation proceeded through the entire deformation zone depth and was highly sensitive to the starting near surface deformation thickness.

Surface finish also affects the nickel rich particle morphology. Fine surface finishes had two distinct nickel particle morphologies: a semi-continuous layer and discrete particles, while the coarser surface finishes only had nickel particles that were discrete in nature. A finer surface finish with less deformation near the surface contains a more uniform surface deformation state, where the coarser surface finishes have areas of high and low deformation states. A more uniform surface energy promotes the more continuous morphology that is seen on the polished surface.

When comparing the plastic strain samples that were machined and mechanically polished, it should be noted that the machined surface finish had a lower mean oxide thickness than the polished finish. The polishing procedure used for the plastic strain samples included grinding steps at much larger forces than were used for the surface finish study. Deformation induced into the subsurface zone from the prior grinding steps altered the oxidation penetration depth in these samples. Separation of procedures that alter near surface microstructure or crystal structure is not possible.

8.4.4 Nickel Enrichment in SCC Cracks

As discussed previously, most oxidation studies of austenitic stainless steels in high temperature water result in a duplex oxide layer composed of a chromium rich inner oxide and an iron rich outer oxide with nickel enrichment present at the inner oxide/metal interface. However, a small body of literature for SCC reports a similar phenomenon as is seen in the loop exposures [176, 178]. Metallic nickel rich particles are occasionally seen at the crack tip and along the crack wall on the inner oxide where the outer oxide would normally be located in a crack. Presence of these nickel metallic nickel particles are not well understood, although the presence of these metallic particles may be able to be explained by

crack chemistry.

Cation depletion inside a growing SCC crack has been suggested to result in lower outer oxide formation and enhanced crack tip oxidation [93]. Metallic nickel has been shown to be thermodynamically stable with the solution when iron ion concentration in solution is very low. Inside a SCC crack that contains a low amount of iron ions in solution, an environment can be present that promotes formation of metallic nickel on the inner oxide surface. Presence of the metallic nickel particles can shift the electrochemical properties of the environment locally in the crack, as discussed earlier, resulting in unexpected SCC crack behavior.

8.5 Conclusions

Exposure to high pressure high temperature water in the loop system results in faster oxidation kinetics than for an autoclave system. The loop system does not emulate the exposure conditions that would be present in a growing crack tip, where flow is expected to be minimal. High flow conditions are however likely to be present in other areas within the primary circuit.

An inner chromium rich oxide formed along with nickel rich metallic particles on the inner oxide/solution interface.

Metallic components are present embedded in the inner oxide. At short exposure times, the metallic components created a connected network that extends from the inner oxide to near the inner oxide/solution interface. At longer exposure times, the connectivity of the metallic network near the oxide/solution interface cannot be confirmed and the components are nickel rich compared to 304. Connected metallic networks are present near the inner oxide/metal interface for all exposure times.

A few mechanisms explaining the enhanced oxidation seen in the loop environment are proposed:

1. Enhanced oxidation occurs via grain boundary diffusion
2. Enhanced oxidation occurs via metallic network formation
3. Enhanced oxidation occurs via nickel rich particles

4. Enhanced oxidation occurs by vacancy clustering promoted by protons created by the reduction of water

Effect of plastic strain on oxidation depth is dependent on the near surface fast oxidation paths. At low levels of plastic strain, there is little effect in oxidation with increasing plastic strain. Above approximately 40% strain, increasing strain results in a decrease in oxidation depth. At high levels of engineering strain, deformation induced martensite forms, consuming dislocation structures. The grain boundary area increase by formation of martensite is not enough to make up for the amount of other fast diffusion paths it consumes, resulting in a decrease in oxide penetration.

Surface finish has a similar effect on oxidation penetration depth as plastic strain. Fine surface finishes result in lower deformation levels than coarser grinding particle sizes. The deformation zone depth into the material is also suggested to be deeper for coarser surface finishes. At fine surface finishes, increasing grinding particle size results in a much deeper oxide penetration. At very coarse surface finishes, there is a competition between increasing deformation structures and consumption of these structures by formation of deformation induced martensite. This results in a much smaller increase of oxide penetration at large particle sizes.

An explanation for nickel enrichment that has been reported in SCC has been proposed. Low iron ion concentration in an SCC crack can shift the local environment to promote metallic nickel formation.

CHAPTER IX

Conclusions and Future Work

9.1 Conclusions

The overall objective of this work is to determine the effect of material condition and environment on the short term oxidation behavior of different grades of metastable austenitic stainless steels. Oxidation behavior results from the combination of material and environmental conditions. Material condition, including surface finish, deformation state, and martensite was studied in air and pressurized water. Plastic strain was studied on uniaxial tension and cold rolled 304 specimens; a relationship between axial and lateral engineering strain during uniaxial tension was investigated for isotropic materials. Low temperature air oxidation behavior was studied on 304 in air at 280, 400, and 700 °C for 50 hours, and the effect of surface finish and plastic strain through uniaxial tension and cold rolling was studied in pressurized water at 280 °C for 10, 50, and 100 hours. These conditions may be present in various locations throughout a PWR; understanding the effect of material condition and environment combinations can help to make reactors safer and lengthen lifespans.

The principal hypotheses tested in this work are as follows:

1. Lateral and axial engineering strain within the uniform elongation regime can be defined for isotropic materials as:

$$\varepsilon_a = \left(\frac{1}{1 - |\varepsilon_l|^{1+x}}\right) - 1$$

2. Increasing plastic strain through uniaxial tension and cold rolling will result in thicker oxide layers for a given exposure time; oxide thickness will follow a linear relationship with uniform axial strain when exposed to high temperature, high pressure water.

3. Increasing martensite content will result in an increase of overall oxidation rate due to the increase in grain boundaries. A thicker oxide will exist over martensite, where oxide thickness is proportional to the difference in diffusion kinetics between the austenite and martensite phases.

4. A coarser surface finish will result in a deeper deformation zone with a thicker oxide due to more fast oxidation pathways. Oxide thickness will be proportional to the finishing particle size.

9.1.1 Strain in the Three Principal Directions

The first hypothesis of this work is that a relationship between axial and lateral engineering strain during uniform elongation of uniaxial tension can be used to predict if a material behaves isotropically or anisotropically. A relationship between lateral and axial engineering strain is derived in Equation 4.7 using the relationship between true and engineering strain as well as assuming plastic incompressibility during plastic deformation. This hypothesis is supported, the relationship between axial and lateral strain has been verified using DIC measurements on isotropic and anisotropic materials. The as-machined samples were modeled quite well with x=1 for an isotropic material, and the cold worked and aluminum samples were modeled with x$\neq$1, as expected for an anisotropic material.

DIC is shown to be a quick, effective way to quickly determine whether a material displays mechanical anisotropy. Calculation of the third principal engineering strain is possible from DIC and gives deviation of the thickness and lateral directions from an isotropic material.

9.1.2 Characterization of Uniaxial Deformation and Strain

Tensile specimens were pulled in uniaxial tension to failure at 21, 250, and 338 °C and to controlled levels of strain using DIC at 21 °C. Two starting material conditions were studied: mill annealed and cold rolled. Hardness, XRD, and EBSD were considered to create a

proxy to determine plastic strain after deformation. Deformation-induced martensite was also studied with the EBSD data.

Hardness does not provide a reliable measure of plastic strain at the high levels of strain present in the samples, and quantitative data for plastic strain from XRD was not possible. Local misorientation, as determined by EBSD, provides a means to quantify plastic strain, although the chemical composition, deformation conditions, and microscope collection parameters need to be consistent to create a relationship between plastic strain and local misorientation.

Mechanical behavior is affected by starting material condition, including cold work. Prior cold work results in higher yield strength and ultimate tensile strength with lower total elongation. On average, the samples with cold work showed lower local misorientation and phase fraction of martensite at the fracture surface. Cold work may change the deformation mechanism on tensile straining.

Prior material condition and testing temperature have a strong effect on deformation-induced martensite. Deformation-induced martensite formed in all samples pulled in tension to failure at room temperature, but only the cold worked samples at the high temperatures.

9.1.3 Effect of Surface Condition on Oxidation in Low Temperature Air

An as machined surface of mill annealed 304 was exposed in a TGA at 280, 400, and 700 °C for 50 hours. These tests were designed to study the relationship between surface condition, near surface martensite, and oxidation kinetics.

The TGA and balance used to monitor the mass change due to oxidation, both during and after low temperature exposure to synthetic air, do not have high enough resolution to capture the mass change. SEM imaging also did not have high enough resolution to image the oxide layer(s). Discrete oxide particles were imaged on the sample surface confirming that the exposure time and temperature did cause oxidation to occur.

9.1.4 High Temperature Deformation-Induced Martensite

Mill annealed and cold rolled 304 tensile specimen were pulled to failure at 21, 250, and 338 °C. The effect of temperature and material starting condition on mechanical properties

and deformation-induced martensite were studied.

Mechanical stress vs. strain behavior was affected by material starting conditions: cold rolling changed the shape of the stress vs. strain curve when compared to an annealed starting condition. Cold rolling results in an increase in yield strength and ultimate tensile strength with a reduction in uniform elongation compared to the annealed condition. Deformation structures that are a result of cold rolling are responsible for the differences in mechanical properties between the two starting material conditions.

The dominant deformation mode active at room temperature differs from that at the two elevated temperatures studied. The stress vs. strain curve shows a decrease in yield strength, ultimate tensile strength, and reduction in uniform elongation at elevated temperatures. Increase in stacking fault energy at elevated temperatures results in a change in the dominant deformation mode along with a change in mechanical properties. The dominant deformation mode active at each temperature was not directly studied.

Cold rolling creates a deformation microstructure that promotes deformation-induced martensite at high temperature. Deformation-induced martensite formed at all temperatures tested for materials that were cold rolled prior to deformation. The annealed material condition transformed to martensite with uniaxial tension at room temperature, but no transformation was detected at the two higher temperatures.

Microstructure of the deformation-induced martensite in the cold rolled samples differs from that of the annealed samples. Martensite is only found to form across an austenite grain in the cold rolled samples, where martensite is also found to form between martensite grains in annealed starting condition. In the region closest to the fracture of the elevated cold rolled sample, martensite grains are no longer parallel. The martensite present in this region formed before necking and curved during necking.

Under the right prior material condition and straining conditions during operation martensite can be formed inside an operating PWR. Martensite has a different crystal structure than austenite and has been shown to have different oxidation behavior than austenite in some environments. Material models may need to account for this phenomenon to obtain more realistic outcomes.

9.1.5 Effect of Material Deformation on Short Time Oxidation in High Temperature Water Environments

Pressurized water exposures of 304 specimens with plastic strain and machined surface finish were completed for 10, 50, and 100 hours at 280 °C. Polished surface finishes with plastic strain, and a range of surface finishes were studied for 100 hour exposures at the same environmental conditions for all exposures. These tests were designed to study the effect of plastic strain and surface finish on the oxidation behavior.

The loop exposure used for environmental exposures of these samples resulted in faster oxidation kinetics than for autoclave systems that are usually used to expose samples. Differences in oxide morphology from those in an autoclave were also present: an inner chromium rich oxide formed along with metallic nickel rich particles on the inner oxide/solution interface. Flow within the loop environment accounts for the presence of nickel rich particles and may result in the increase in oxidation kinetics.

Metallic components are present embedded in the inner oxide. At short exposure times, the metallic components created a connected network that extends from the inner oxide to near the inner oxide/solution interface. At longer exposure times, the connectivity of the metallic network near the oxide/solution interface cannot be confirmed and the components are nickel rich compared to 304. Connected metallic networks are present near the inner oxide/metal interface for all exposure times.

A few mechanisms explaining the enhanced oxidation seen in the loop environment are proposed:

1. Enhanced oxidation occurs via grain boundary diffusion
2. Enhanced oxidation occurs via metallic network formation
3. Enhanced oxidation occurs by vacancy clustering promoted by protons created by the reduction of water

The second hypothesis states that increasing plastic strain through uniaxial tension and cold rolling will result in thicker oxide layers for a given exposure time and that the oxide thickness will follow a linear relationship with strain when exposed to high temperature,

high pressure water. This hypothesis is unsupported. The effect of plastic strain was studied on both machined surface finishes at 10, 50 and 100 hours and polished surface finish at 100 hours. Effect of plastic strain on oxidation depth is dependent on the near surface fast oxidation paths. At low levels of plastic strain, there was little effect on oxidation with increasing plastic strain. Above approximately 40% strain, increasing strain results in a decrease in the oxidation depth.

The third hypothesis states that increasing martensite content will increase the oxidation rate and that the oxide thickness will be larger over the martensite phase. The difference in thickness over austenite and martensite will be proportional to the diffusion kinetics between the two phases. This hypothesis is unsupported. At high levels of engineering strain, deformation-induced martensite forms, consuming dislocation structures. The grain boundary area increases by formation of martensite is not enough to make up for the amount of other fast diffusion paths it consumes, resulting in a decrease in oxide penetration. Increasing martensite content results in a decrease in the oxidation rate.

The final hypothesis is that a coarser surface finish will have a deeper oxidation zone and a thicker oxide due to more fast oxidation pathways, where the oxide thickness is proportional to the finishing particle size. This hypothesis is supported. Coarser surface finishes resulted in a thicker oxide thickness; oxide thickness was related to particle size using a power law relationship. Fine surface finishes result in lower deformation levels than coarser grinding particle sizes. The deformation zone depth into the material is also found to be deeper for coarser surface finishes. At fine surface finishes, increasing grinding particle size results in a much deeper oxide penetration. At very coarse surface finishes, there is a competition between increasing deformation structures and consumption of these structures by formation of deformation-induced martensite. This results in a much smaller increase of oxide penetration at large particle sizes.

Nickel enrichment has been reported in SCC and an explanation for formation has been proposed. Low iron ion concentration in an SCC crack can shift the local environment to promote metallic nickel formation.

9.2 Future Work

This work aims to develop an understanding of the effect of material condition and environment on the short term oxidation behavior of different grades of metastable austenitic stainless steels. The effect of surface condition, plastic strain, and martensite still needs further development.

To allow for local misorientation to be used as a proxy for plastic strain in components removed from service, calibration curves need to be constructed for specific materials of interest along with specified microscope parameters. Calibration curves may not be feasible to create for many material conditions where unknown starting material conditions and deformation pathways may exist.

The formation of high temperature deformation-induced martensite, at temperatures much higher than those predicted in the Olsen and Cohen model, have been confirmed in a cold rolled starting material condition tested in air. The model proposed by Olsen and Cohen does not accurately predict the potential for high temperature deformation induced martensite. This model can be expanded upon through a better understanding of the deformation microstructure present in the cold rolled starting condition along with understanding the transformation mechanisms at high temperature. More extensive TEM studies to characterize deformation structures present before straining that may act as nucleation sites along with a more controlled temperature range study are necessary to understand the deformation structures that are present and how temperature affects transformation. Understanding of these features can help to better predict what conditions can promote deformation-induced martensite including conditions that may be present in a growing environmentally assisted crack leading to high temperature deformation-induced martensite in a PWR environment.

More work on short time exposures in the high temperature water environments are needed to better understand short time oxidation behavior present in PWR reactors. A large amount of oxidation studies have been performed in autoclaves, necessitating understanding the differences in oxidation behavior between autoclave and the loop systems. One major difference between the two systems is the flow regime at which they operate; studies with

varied flow rates can inform differences between the systems due to flow. This may be an important consideration when it comes to exposure of various plant components and their respective exposure conditions in service that has not been accurately captured in literature testing.

A sample could be designed and fabricated with flow channels that allow some areas of the sample to be exposed to turbulent flow while others within the same sample are exposed to laminar flow. Single tests can allow for multiple exposure environments within the same sample in the loop. This will allow study of the effect of flow rate while controlling exposure of the sample to short time oxidation.

The oxide structure that forms in the loop is also different from that which forms in an autoclave. Connectivity of the metallic networks embedded in the inner oxide phase along with inner oxide porosity can help inform the enhanced oxidation present in the loop system. Inclusion of other characterization techniques such as AES or XPS combined with sputtering will provide insight on composition of the inner oxide/metallic networks along with any variations in oxide condition. Atom probe tomography studies could allow direct observation of the metallic structures and allow confirmation of connectivity at different exposure times; 3D EBSD would also allow for all the features to simultaneously be studied at lower resolution than would be possible using atom probe tomography.

The effect of plastic strain on short time oxidation can be isolated by inducing deformation during high temperature straining to suppress deformation-induced martensite transformation. Plastic strain can induce multiple deformation microstructures including dislocations and twins which would be studied jointly.

The effect of near surface martensite on oxidation behavior in high temperature water was not determined by the techniques used in this study. More controlled studies of near surface crystal structure are needed to determine differences in oxidation between austenite and martensite phases. A range of martensite can be induced through cooling to allow for controlled contents of martensite in an austenite matrix. Exposure of these specimen in high temperature, high pressure water followed by cross sectioning and oxide thickness determination over austenite and martensite phases.

BIBLIOGRAPHY

[1] *Chapter 17.0 Plant Operations, Westinghouse Technology Manual*, pages 17–1–20–21. Westinghouse.

[2] Creating innovative steel solutions. *AK Steel*.

[3] F. B. Pickering. *Physical metallurgy and the design of steels*. Applied Science Publ., 1983.

[4] X Ru and R W Staehle. Historical Experience Providing Bases for Predicting Corrosion and Stress Corrosion in Emerging Supercritical Water Nuclear Technology : Part 1 — Review. *Corrosion*, 69(3):211–229, 2013.

[5] Anton L Schaeffler. Constitution diagram for stainless steel weld metal. *Metal progress*, 56(11):680, 1949.

[6] N. Li, Y. D. Wang, W. J. Liu, Z. N. An, J. P. Liu, R. Su, J. Li, and P. K. Liaw. In situ X-ray microdiffraction study of deformation-induced phase transformation in 304 austenitic stainless steel. *Acta Materialia*, 64:12–23, 2014.

[7] Erich Folkhard. *Welding metallurgy of stainless steels*. Springer Science & Business Media, 2012.

[8] Hans-Joachim Eckstein. *Wärmebehandlung von Stahl: metallkundliche Grundlagen*. Dt. Verlag f. Grundstoffindustrie, 1969.

[9] Jan Fridberg, L-E Torndahl, and Mats Hillert. Diffusion in iron. *Jernkontorets Ann*, 153(6):263–276, 1969.

[10] G. B. Olson and Morris Cohen. Kinetics of strain-induced martensitic nucleation. *Metallurgical Transactions A*, 6(4):791–795, 1975.

[11] T. Michler. Austenitic stainless steels. *Reference Module in Materials Science and Materials Engineering*, 2016.

[12] Shimizu K. Nishiyama, Z. and S. Morikawa. *Journal of the Japan Institute of Metals and Materials*, 1964.

[13] Zenji Nishiyama, M. Meshii, C. M. Wayman, and Morris E. Fine. *Martensitic transformation*. Academic Press, 1978.

[14] Sergio Lozano-Perez, Karen Kruska, Ilya Iyengar, Takumi Terachi, and Takuyo Yamada. The role of cold work and applied stress on surface oxidation of 304 stainless steel. *Corrosion Science*, 56:78–85, 2012.

[15] K. Kruska, S. Lozano-Perez, D. W. Saxey, T. Terachi, T. Yamada, and G. D. W. Smith. 3d atom-probe characterization of stress and cold-work in stress corrosion cracking of 304 stainless steel. *Proceedings of the 15th International Conference on Environmental Degradation of Materials in Nuclear Power Systems — Water Reactors*, page 939–951, 2011.

[16] S.g. Acharyya, A. Khandelwal, V. Kain, A. Kumar, and I. Samajdar. Surface working of 304l stainless steel: Impact on microstructure, electrochemical behavior and scc resistance. *Materials Characterization*, 72:68–76, 2012.

[17] M Ashbya and M Smidmana. *Materials for Nuclear Power Systems*. 2011.

[18] EPRI. *PWR Primary Water Chemistry Guidelines*, volume 1. 1999.

[19] P J Cunat. Alloying elements in stainless steel and other chromium-containing allpys. *International Chromium Development Association*, 45(6):122–131, 2004.

[20] Reshift Media. The difference between 304 and 316 stainless steel, Dec 2019.

[21] S.e. Ziemniak and M. Hanson. Corrosion behavior of 304 stainless steel in high temperature, hydrogenated water. *Corrosion Science*, 44(10):2209–2230, 2002.

[22] Sarata Cissé, Lydia Laffont, Benoit Tanguy, Marie Christine Lafont, and Eric Andrieu. Effect of surface preparation on the corrosion of austenitic stainless steel 304L in high temperature steam and simulated PWR primary water. *Corrosion Science*, 56:209–216, 2012.

[23] Guangdong Han, Zhanpeng Lu, Xiangkun Ru, Junjie Chen, Qian Xiao, and Yongwu Tian. Improving the oxidation resistance of 316l stainless steel in simulated pressurized water reactor primary water by electropolishing treatment. *Journal of Nuclear Materials*, 467:194–204, 2015.

[24] L Chang, J Duff, M G Burke, and F Scenini. *SCC Initiation in the Machined Austenitic Stainless Steel 316L in Simulated PWR Primary Water*, page 811–827. 2017.

[25] Amar K. De, John G. Speer, David K. Matlock, David C. Murdock, Martin C. Mataya, and Robert J. Comstock. Deformation-induced phase transformation and strain hardening in type 304 austenitic stainless steel. *Metallurgical and Materials Transactions A: Physical Metallurgy and Materials Science*, 37(6):1875–1886, 2006.

[26] SJ Pawlak. Austenite stability in the high strength metastable stainless steels. *Journal of Achievements in Materials and Manufacturing Engineering*, 22(2):2–5, 2007.

[27] Zeng Wu and Yuan Huang. Characterization of a Metastable Austenitic Stainless Steel with Severe Plastic Distortions. *Procedia Engineering*, 99:1323–1329, 2015.

[28] G H Eichelman and F C Hull. The effects of composition on the temperature of spontaneous transformation of austenite to martensite in 18-8 type stainless steels. *Transactions: American Society for Metals*, page 77–104, 1953.

[29] F C Monkman, F B Cuff, and N J Grant. Computation of ms for stainless steels. *Metal Progress*, 71(4):94, 1957.

[30] W. F. Gale, T. C. Totemeier, and Colin J. Smithells. *Smithells metals reference book*. Elsevier Butterworth-Heinemann, 2004.

[31] John Ågren. A revised expression for the diffusivity of carbon in binary fe-c austenite. *Scripta Metallurgica*, 20(11):1507–1510, 1986.

[32] A. W. Bowen and G. M. Leak. Solute diffusion in alpha- and gamma-iron. *Metallurgical Transactions*, 1(6):1695–1700, 1970.

[33] C. L. Briant and A. M. Ritter. The effects of deformation induced martensite on the sensitization of austenitic stainless steels. *Metallurgical Transactions A*, 11(12):2009–2017, 1980.

[34] Lawrence S. Darken, Robert W. Gurry, and Michael B. Bever. *Physical chemistry of metals*. CBS Publishers Distributors Pvt. Ltd., 2002.

[35] William D Jr. Callister. *Materials Science and Engineering*. Wiley-Blackwell, 2013.

[36] B Cina. Effect of cold work on the gamma to alpha transformation in some fe-ni-cr alloys. *J. Iron Steel Inst*, 177:406–422, 1954.

[37] R Langneborg. *Acta Met*, (12), 1964.

[38] E Bain. The nature of martensite. *Metall. Trans.*, 70:25, 1924.

[39] G.B. Olson and Morris Cohen. A mechanism for the strain-induced nucleation of Martensitic Transformations. 28:107–118, 1972.

[40] Gregory B. Olson and M Cohen. A General Mechanism of Martensitic Nucleation: Part I . General Concepts and the FCC HCP Transformation. *Metallurgical Transactions A*, 7(December):1897–1904, 1976.

[41] S. Kajiwara. Roles of dislocations and grain boundaries in martensite nucleation. *Metallurgical and Materials Transactions A*, 17(10):1693–1702, 1986.

[42] Junliang Liu. Scholar Commons Deformation Induced Martensitic Transformation In 304 Stainless Steels. 2016.

[43] Juho Talonen, Pertti Nenonen, Gersom Pape, and Hannu Hänninen. Effect of Strain Rate on the Strain-Induced [gamma] [arrow right] [alpha]' -Ma. *Metallurgical and Materials Transactions*, 36A:421, 2005.

[44] V. Mertinger, E. Nagy, F. Tranta, and J. Sólyom. Strain-induced martensitic transformation in textured austenitic stainless steels. *Materials Science and Engineering A*, 481-482(1-2 C):718–722, 2008.

[45] S. S.M. Tavares, D. Gunderov, V. Stolyarov, and J. M. Neto. Phase transformation induced by severe plastic deformation in the AISI 304L stainless steel. *Materials Science and Engineering A*, 358(1-2):32–36, 2003.

[46] S. K. Ghosh, P. Mallick, and P. P. Chattopadhyay. Effect of Cold Deformation on Phase Evolution and Mechanical Properties in an Austenitic Stainless Steel for Structural and Safety Applications. *Journal of Iron and Steel Research International*, 19(4):63–68, 2012.

[47] G B Olson and Morris Cohen. Kinetics of Strain-Induced Martensitic Nucleation. *Mat. Trans. A*, 6(4):791–795, 1975.

[48] J. Talonen, P. Aspegren, and H. Hänninen. Comparison of different methods for measuring strain induced α-martensite content in austenitic steels. *Materials Science and Technology*, 20(12):1506–1512, 2004.

[49] L. E. Murr, K. P. Staudhammer, and S. S. Hecker. Effects of Strain State and Strain Rate on Deformation-Induced Transformation in 304 Stainless Steel : Part I1 . Microstructural Study. 13(April), 1982.

[50] Arpan Das and Soumitra Tarafder. Experimental investigation on martensitic transformation and fracture morphologies of austenitic stainless steel. *International Journal of Plasticity*, 25(11):2222–2247, 2009.

[51] A Das, P Sivaprasad, P Chackraborti, and S Tarafder. Effect of strain rate on the strain-induced , $\rightarrow$ -martensite transformation and mechanical properties of austenitic stainless steels. *International Journal of Plasticity*, 25(11):2222–2247, 2009.

[52] K. Spencer, M. Véron, K. Yu-Zhang, and J. D. Embury. The strain induced martensite transformation in austenitic stainless steels: Part 1 – Influence of temperature and strain history. *Materials Science and Technology*, 25(1):7–17, 2009.

[53] Frank Hahnenberger, Marek Smaga, and Dietmar Eifler. Microstructural investigation of the fatigue behavior and phase transformation in metastable austenitic steels at ambient and lower temperatures. *International Journal of Fatigue*, 69:36–48, 2014.

[54] G.B. Olson and Morris Cohen. Kinetics of Strain Induced Martensitic Nucleation. *Metallurgical Transactions A*, 6A:791–795, 1975.

[55] S. S. Hecker, M. G. Stout, K. P. Staudhammer, and J. L. Smith. Effects of Strain State and Strain Rate on Deformation-Induced Transformation in 304 Stainless Steel: Part I. Magnetic Measurements and Mechanical Behavior. *Metallurgical Transactions A*, 13(4):619–626, 1982.

[56] T Angel. Formation of martensite in austenitic stainless steels effects of deformation, temperature and composition. *Iron and Steel Institute*, 177:165–174, 1957.

[57] Kazunori Sato, Michiyuki Ichinose, Yoshihiko Hirotsu, and Yasunobu Inoue. Effects of deformation induced phase transformation and twinning on the mechanical properties of austenitic fe-mn-al alloys. *ISIJ International*, 29(10):868–877, 1989.

[58] Y.f. Shen, X.x. Li, X. Sun, Y.d. Wang, and L. Zuo. Twinning and martensite in a 304 austenitic stainless steel. *Materials Science and Engineering: A*, 552:514–522, 2012.

[59] G. L. Huang, D. K. Matlock, and G. Krauss. Martensite formation, strain rate sensitivity, and deformation behavior of type 304 stainless steel sheet. *Metallurgical transactions. A, Physical metallurgy and materials science*, 20 A(7):1239–1246, 1989.

[60] Sebastien Allain, J. P. Chateau, and O. Bouaziz. A physical model of the twinning-induced plasticity effect in a high manganese austenitic steel. *Materials Science and Engineering A*, 387-389(1-2 SPEC. ISS.):143–147, 2004.

[61] R.E. Schramm and R.P. Reed. Stacking Fault Energies of Seven Commercial Austenitic Stainless Steels. *Metallurgical Transactions A*, 6A:1345–1351, 1975.

[62] F. Di Gioacchino and J. Quinta Da Fonseca. Plastic strain mapping with sub-micron resolution using digital image correlation. *Experimental Mechanics*, 53(5):743–754, 2012.

[63] Hassan Nashid, Charles Clifton, George Ferguson, Micheal Hodgson, Chris Seal, and Jay-Hyouk Choi. Relationship between hardness and plastically deformed structural steel elements. *Earthquakes and Structures*, 8(3):619–637, 2015.

[64] I. Nikitin and M. Besel. Correlation between residual stress and plastic strain amplitude during low cycle fatigue of mechanically surface treated austenitic stainless steel aisi 304 and ferritic–pearlitic steel sae 1045. *Materials Science and Engineering: A*, 491(1-2):297–303, 2008.

[65] Nathan A. Branch, Ghatu Subhash, Nagaraj K. Arakere, and Michael A. Klecka. Material-dependent representative plastic strain for the prediction of indentation hardness. *Acta Materialia*, 58(19):6487–6494, 2010.

[66] Xianguang Zhang, Kiyotaka Matsuura, Munekazu Ohno, and Seiichi Suzuki. Quantification of local plastic strain distribution beneath surface of deformed iron. *Materials Science and Engineering: A*, 564:169–175, 2013.

[67] H.k. Yang, V. Doquet, and Z.f. Zhang. Micro-scale measurements of plastic strain field, and local contributions of slip and twinning in twip steels during in situ tensile tests. *Materials Science and Engineering: A*, 672:7–14, 2016.

[68] Swati Ghosh and Vivekanand Kain. Microstructural changes in AISI 304L stainless steel due to surface machining: Effect on its susceptibility to chloride stress corrosion cracking. *Journal of Nuclear Materials*, 403(1-3):62–67, 2010.

[69] Young Geun Kim, Seon Yeob Li, Sungwon Jung, Seong Min Lee, Jiyoung Kim, and Young Tai Kho. Corrosion behaviors of sputter-deposited steel thin film for electrical resistance sensor material. *Surface and Coatings Technology*, 201(3-4):1731–1738, 2006.

[70] Adam J Schwartz, Mukul Kumar, Brent L Adams, and David P Field. *Electron backscatter diffraction in materials science*, volume 2. Springer, 2009.

[71] Edward M Lehockey, Yang-Pi Lin, and Olev E Lepik. Mapping residual plastic strain in materials using electron backscatter diffraction. In *Electron backscatter diffraction in materials science*, pages 247–264. Springer, 2000.

[72] TM Angeliu, PL Andresen, E Hall, JA Sutliff, S Sitzman, and RM Horn. Intergranular stress corrosion cracking of unsensitized stainless steels in bwr environments. In *Ninth International Symposium on Environmental Degradation of Materials in Nuclear Power Systems—Water Reactors*, pages 311–318. Wiley Online Library, 1999.

[73] GA Young, N Lewis, CK Battige, RA Somers, MA Penik, L Brewer, and M Othon. Quantification of residual plastic strains in ni-cr-mn-nb gtaw welds via electron backscatter diffraction. In *Sixth International Conference on Trends in Welding Research*, 2002.

[74] Hualong Li, Emilie Hsu, Jerzy Szpunar, Hiroshi Utsunomiya, and Tetsuo Sakai. Deformation mechanism and texture and microstructure evolution during high-speed rolling of az31b mg sheets. *Journal of materials science*, 43(22):7148–7156, 2008.

[75] Rickard R Shen and Pål Efsing. Overcoming the drawbacks of plastic strain estimation based on kam. *Ultramicroscopy*, 184:156–163, 2018.

[76] George Z. Voyiadjis, Peter I. Kattan, George Z. Voyiadjis, and Peter I. Kattan. *Advances in Damage Mechanics: Metals and Metal Matrix Composites*, pages vii–ix, 1999.

[77] Jean Lemaitre. *Handbook of materials behavior models*. Academic press, 2001.

[78] Z.l. Zhang, M. Hauge, J. Ødegård, and C. Thaulow. Determining material true stress–strain curve from tensile specimens with rectangular cross-section. *International Journal of Solids and Structures*, 36(23):3497–3516, 1999.

[79] I. Scheider, W. Brocks, and A. Cornec. Procedure for the determination of true stress-strain curves from tensile tests with rectangular cross-section specimens. *Journal of Engineering Materials and Technology*, 126(1):70–76, 2004.

[80] N.e. Hakiki, M.f. Montemor, M.g.s. Ferreira, and M. Da Cunha Belo. Semiconducting properties of thermally grown oxide films on aisi 304 stainless steel. *Corrosion Science*, 42(4):687–702, 2000.

[81] Mattias Calmunger, Robert Eriksson, Guocai Chai, Sten Johansson, and Johan J. Moverare. Surface phase transformation in austenitic stainless steel induced by cyclic oxidation in humidified air. *Corrosion Science*, 100:524–534, 2015.

[82] C.l. Briant and A.m. Ritter. The effect of cold work on the sensitization of 304 stainless steel. *Scripta Metallurgica*, 13(5):418, 1979.

[83] Simon Detriche, Sebastien Vivegnis, J-F Vanhumbeeck, Alexandre Felten, Pierre Louette, FU Renner, Joseph Delhalle, and Zineb Mekhalif. Xps fast depth profile of the native oxide layers on aisi 304, 316 and 430 commercial stainless steels and their evolution with time. *Journal of Electron Spectroscopy and Related Phenomena*, 243:146970, 2020.

[84] C.-O.A Olsson and D Landolt. Passive films on stainless steels—chemistry, structure and growth. *Electrochimica Acta*, 48(9):1093–1104, 2003.

[85] M Seo and N Sato. Surface characterization of stainless steels prepared with various surface treatments. *Transactions of the Japan Institute of Metals*, 21(12):805–810, 1980.

[86] Steve Trigwell and Guna Selvaduray. Effects of welding on the passive oxide film of electropolished 316l stainless steel. *Journal of materials processing technology*, 166(1):30–43, 2005.

[87] Jianyu Xiong, Swati Agarwala, Mike Yongjun Tan, and Maria Forsyth. The restoration of the passivity of stainless steel weldments in pickling solutions observed using electrochemical and surface analytical methods. *Corrosion*, 71(10):1248–1256, 2015.

[88] Mattias Calmunger, Robert Eriksson, Guocai Chai, Sten Johansson, and Johan J. Moverare. Surface phase transformation in austenitic stainless steel induced by cyclic oxidation in humidified air. *Corrosion Science*, 100:524–534, 2015.

[89] Frédéric Riffard, Henri Buscail, F Rabaste, Eric Caudron, Régis Cueff, Christophe Issartel, N Karimi, and Sébastien Perrier. Manganese effect on isothermal high temperature oxidation behaviour of aisi 304 stainless steel. In *Materials Science Forum*, volume 595, pages 1127–1134. Trans Tech Publ, 2008.

[90] NS Quan and DJ Young. Sulfidation behavior of an aluminum-manganese steel. *Oxidation of metals*, 25(1):107–119, 1986.

[91] B Pieraggi. Calculations of parabolic reaction rate constants. *Oxidation of metals*, 27(3):177–185, 1987.

[92] H Hindam and DP Whittle. Microstructure, adhesion and growth kinetics of protective scales on metals and alloys. *Oxidation of metals*, 18(5):245–284, 1982.

[93] Zhao Shen, Donghai Du, Lefu Zhang, and Sergio Lozano-Perez. An insight into pwr primary water scc mechanisms by comparing surface and crack oxidation. *Corrosion Science*, 148:213–227, 2019.

[94] Anette Nørgaard Hansson, Karen Pantleon, Flemming Bjerg Grumsen, and Marcel AJ Somers. Microstructure evolution during steam oxidation of a nb stabilized austenitic stainless steel. *Oxidation of Metals*, 73(1):289–309, 2010.

[95] Zhao Shen, David Tweddle, Hongbing Yu, Guanze He, Aakash Varambhia, Phani Karamched, Felix Hofmann, Angus J Wilkinson, Michael P Moody, Lefu Zhang, et al. Microstructural understanding of the oxidation of an austenitic stainless steel in high-temperature steam through advanced characterization. *Acta Materialia*, 194:321–336, 2020.

[96] Gary S Was, Sebastian Teysseyre, and Z Jiao. Corrosion of austenitic alloys in supercritical water. *Corrosion*, 62(11):989–1005, 2006.

[97] Juntao Yuan, Ximao Wu, Wen Wang, Shenglong Zhu, and Fuhui Wang. The effect of surface finish on the scaling behavior of stainless steel in steam and supercritical water. *Oxidation of metals*, 79(5):541–551, 2013.

[98] D. H. Lister, R. D. Davidson, and E. McAlpine. The mechanism and kinetics of corrosion product release from stainless steel in lithiated high temperature water. *Corrosion Science*, 27(2), 1987.

[99] R. L. Tapping, R. D. Davidson, E. Mcalpine, and D. H. Lister. Cheminform abstract: Composition and morphology of oxide films formed on type 304 stainless steel in lithiated high temperature water. *Chemischer Informationsdienst*, 17(46), 1986.

[100] D H Lister, E McAlpine, and N S McIntyre. *Proc. Conf. Water Chemistry of Nucl. Reactor Systems*, 3:69–75, 1984.

[101] M Warzee, C Sonnen, and Ph Berge. *Corrosion of Carbon Steels and Stainless Steels in Pressurised Water of High Temperatures.* 1967.

[102] I Michel and C Plog. *Metall.*, 31:252–256, 1977.

[103] Frank Michel and Reinhart Winkler. Ein neuer weg zur verbesserung der korrosionsschutzschichten auf stahl in heißwasser. *Materials and Corrosion/Werkstoffe und Korrosion*, 39(9):412–416, 1988.

[104] J Robertson. The mechanisms of high temperature aqueous corrosion of stainless steels. *Corrosion Science*, 32(4):443–465, 1991.

[105] B. Stellwag. The mechanism of oxide film formation on austenitic stainless steels in high temperature water. *Corrosion Science*, 40(2-3):337–370, 1998.

[106] R Winkler, F Huttner, and F Michel. Senkung der korrosionsrate im primaerkreislauf von druckwasserreaktoren zur begrenzung radioaktiver ablagerungen. *VGB Kraftwekstechnik*, 69(5):527–531, 1989.

[107] Takumi Terachi, Takuyo Yamada, Tomoki Miyamoto, Koji Arioka, and Koji Fukuya. Corrosion Behavior of Stainless Steels in Simulated PWR Primary Water — Effect of Chromium Content in Alloys and Dissolved Hydrogen — Corrosion Behavior of Stainless Steels in Simulated PWR Primary Water — Effect of Chromium Content in Alloys and Dissolve. *Journal of Nuclear Science and Technology*, 45(10):975–984, 2008.

[108] Stephen E. Ziemniak, Michael Hanson, and Paul C. Sander. Electropolishing effects on corrosion behavior of 304 stainless steel in high temperature, hydrogenated water. *Corrosion Science*, 50(9):2465–2477, 2008.

[109] J Morrison, N Johnson, T Hutchinson, T Caswell, B Connolly, and A Banks. *Effect of surface finish on the corrosion behaviour of grade 316L stainless steels in pressurized, high temperature, lithiated water.* 2015.

[110] M Bloom, C Newport, and W Fraser. Steel corrosion mechanisms. *Electrochemical Society*, 111:1343–1347, 1964.

[111] L. Douglas and F. C. Zyzes. The corrosion of iron in high-temperature water (part 1—corrosion rate measurements). *Corrosion*, 13(6):19–32, 1957.

[112] J.e. Castle and H.g. Masterson. The role of diffusion in the oxidation of mild steel in high temperature aqueous solutions. *Corrosion Science*, 6(3-4):93–104, 1966.

[113] SJ Rothman, LJ Nowicki, and GE Murch. Self-diffusion in austenitic fe-cr-ni alloys. *Journal of Physics F: Metal Physics*, 10(3):383, 1980.

[114] David Tice, Norman Platts, Keith Rigby, John Stairmand, and Howard Fairbrother. Environmentally Assisted Crack Growth of Cold-Worked Type 304 Stainless Steel in PWR Environments. *12th International Conference on Environmental Degradation of Materials in Nuclear Power System – Water Reactors*, pages 1037–1048, 2005.

[115] Sergio Lozano-Perez, David W. Saxey, Takuyo Yamada, and Takumi Terachi. Atom-probe tomography characterization of the oxidation of stainless steel. *Scripta Materialia*, 62(11):855–858, 2010.

[116] Nian Zhou, Ru Lin Peng, and Rachel Pettersson. Surface characterization of austenitic stainless steel 304L after different grinding operations. *International Journal of Mechanical and Materials Engineering*, 12(6):1–14, 2017.

[117] D R Tice, V Addepalli, K J Mottershead, M G Burke, F Scenini, S Lozano-Perez, and G Pimentel. *Microstructural Effects on Stress Corrosion Initiation in Austenitic Stainless Steel in PWR Environments D.R.*, page 775–792. 2017.

[118] M Warzee, J Hennaut, M Maurice, C Sonnen, J Waty, and P Berge. Effect of surface treatment on the corrosion of stainless steels in high temperature water and steam. *J. Electrochm. Soc.*, 112:670–674, 1965.

[119] S.e. Ziemniak and M. Hanson. Corrosion behavior of 304 stainless steel in high temperature, hydrogenated water. 2001.

[120] M Boisson, L Legras, F Carrette, O Wendling, T Sauvage, A Bellamy, P Desgardin, L Lafffont, and E Andrieu. *Comparative Study on Short Time Oxidation of Un-Irradiated and Protons Pre-Irradiated 316L Stainless Steel in Simulated PWR Water*. 2017.

[121] Alexandre La Fontaine, Hung-Wei Yen, Peter J. Felfer, Simon P. Ringer, and Julie M. Cairney. Atom probe study of chromium oxide spinels formed during intergranular corrosion. *Scripta Materialia*, 99:1–4, 2015.

[122] C. K. Mukhopadhyay, K. V. Kasiviswanathan, T. Jayakumar, and Baldev Raj. Acoustic emission from ageing-induced martensite formation in cold worked AISI type 304 stainless steel. *Scripta Metallurgica et Materiala*, 30(3):303–307, 1994.

[123] M. Martin, S. Weber, C. Izawa, S. Wagner, A. Pundt, and W. Theisen. Influence of machining-induced martensite on hydrogen-assisted fracture of aisi type 304 austenitic stainless steel. *International Journal of Hydrogen Energy*, 36(17):11195–11206, 2011.

[124] M. Asawa. Stress corrosion cracking regions on contour maps of dissolution rates for aisi 304 stainless steel in sulfuric acid solutions with chloride, bromide, or iodide. *Corrosion*, 43(4):198–203, 1987.

[125] Hamilton Ferreira Gomes De Abreu, Sheyla Santana De Carvalho, Pedro De Lima Neto, Ricardo Pires Dos Santos, Válder Nogueira Freire, Paulo Maria De Oliveira Silva, and Sérgio Souto Maior Tavares. Deformation induced martensite in an aisi 301ln stainless steel: characterization and influence on pitting corrosion resistance. *Materials Research*, 10(4):359–366, 2007.

[126] Mikhail Khadyko, David Morin, Tore Børvik, and Odd Sture Hopperstad. Tensile ductility of extruded aluminium alloy aa6063 in different tempers. *Materials Science and Engineering: A*, 744:500–511, 2019.

[127] Marion Fourmeau, Tore Børvik, Ahmed Benallal, and Odd Sture Hopperstad. Anisotropic failure modes of high-strength aluminium alloy under various stress states. *International Journal of Plasticity*, 48:34–53, 2013.

[128] Bjørn Håkon Frodal, David Morin, Tore Børvik, and Odd Sture Hopperstad. On the effect of plastic anisotropy, strength and work hardening on the tensile ductility of aluminium alloys. *International Journal of Solids and Structures*, 188:118–132, 2020.

[129] A Amine Benzerga, Nithin Thomas, and Joshua S Herrington. Plastic flow anisotropy drives shear fracture. *Scientific reports*, 9(1):1–9, 2019.

[130] A Krupkowski and S Kawinski. The phenomenon of anisotropy in annealed polycrystalline metals. *Journal of the Institute of Metals*, 75(11):869–880, 1949.

[131] WF Langkord, SC Snyder, and J Bausch. New criteria for predicting the press performance of deep drawing steels. *Trans, Amer. Soc. Metals*, 42:1197–1232, 1950.

[132] George Z Voyiadjis, George Z Voyiadjis, and Peter Issa Kattan. *Advances in damage mechanics: metals and metal matrix composites*. Elsevier, 1999.

[133] ME Babeshko and Yu N Shevchenko. Plastic incompressibility of anisotropic material. *International Applied Mechanics*, 41(3):256–263, 2005.

[134] Graham W. Cullen and Yannis P. Korkolis. Ductility of 304 stainless steel under pulsed uniaxial loading. *International Journal of Solids and Structures*, 50(10):1621–1633, 2013.

[135] G Centeno, AJ Martínez-Donaire, D Morales-Palma, C Vallellano, MB Silva, and PAF Martins. Novel experimental techniques for the determination of the forming limits at necking and fracture. In *Materials Forming and Machining*, pages 1–24. Elsevier, 2015.

[136] Robert E Zinkham. Anisotropy and thickness effects in fracture of 7075-t6 and-t651 aluminum alloy. *Engineering Fracture Mechanics*, 1(2):275–276, 1968.

[137] Instron. Dic replay.

[138] Bora Sener, Emre Esener, and Mehmet Firat. Modeling plastic anisotropy evolution of aisi 304 steel sheets by a polynomial yield function. *SN Applied Sciences*, 3(2), 2021.

[139] Manojit Ghosh, A. Miroux, and L.A.I. Kestens. Correlating r-value and through thickness texture in al–mg–si alloy sheets. *Journal of Alloys and Compounds*, 619:585–591, 01 2015.

[140] Wade Karlsen, Gonzalo Diego, and Bastian Devrient. Localized deformation as a key precursor to initiation of intergranular stress corrosion cracking of austenitic stainless steels employed in nuclear power plants. *Journal of Nuclear Materials*, 406(1):138–151, 2010.

[141] M Tsubota, Y Kanazawa, and H Inoue. The effect of cold work on the sec susceptibility of austenitic stainless steels. *Seventh International Symposium on Environmental Degradation of Materials in Nuclear Power Systems*, 1995.

[142] CO Ruud, DJ Snoha, ME Jacobs, and SD Weedman. Plastic deformation, residual stress, and crystalline texture measurements for in-process characterization of fcc metal alloys. In *Review of Progress in Quantitative Nondestructive Evaluation*, pages 1795–1801. Springer, 1989.

[143] Scott A Speakman. Estimating crystallite size using xrd.

[144] ASTM. E112-12 Standard Test Methods for Determining Average Grain Size. *ASTM Book of Standards*, 2014.

[145] Caroline A Schneider, Wayne S Rasband, and Kevin W Eliceiri. Nih image to imagej: 25 years of image analysis. *Nature Methods*, 9(7):671–675, 2012.

[146] Jade pro. *Materials Data Inc.*

[147] Aztec. *Oxford Instruments NanoAnalysis Asylum Research, Inc.*

[148] Hkl channel 5. *Oxford Instruments NanoAnalysis Asylum Research, Inc.*

[149] Kernel average misorientation (kam), Oct 2020.

[150] Raghuram Karthik Desu, Hansoge Nitin Krishnamurthy, Aditya Balu, Amit Kumar Gupta, and Swadesh Kumar Singh. Mechanical properties of austenitic stainless steel 304l and 316l at elevated temperatures. *Journal of Materials Research and Technology*, 5(1):13–20, 2016.

[151] R Rathbun. Strain aging behavior of austenitic stainless steels containing strain induced martensite. *Scripta Materialia*, 42(9):887–891, 2000.

[152] S. S. Hecker, M. G. Stout, K. P. Staudhammer, and J. L. Smith. Effects of strain state and strain rate on deformation-induced transformation in 304 stainless steel: Part i. magnetic measurements and mechanical behavior. *Metallurgical Transactions A*, 13(4):619–626, 1982.

[153] T. Angel. Formation of martensite in austenitic stainless steels effects of deformation, temperature and composition. *Iron and Steel Institute*, 177:165–174, 1957.

[154] S. Nishiyama and S. Morikawa. *Journal of the Japan Institute for Metals and Materials*, 1964.

[155] Zenji Nishiyama, Moris E. Fine, M. Meshii, S. Sato, and C. Marvin Wayman. *Martensitic transformation.* Academic Press, 1978.

[156] Arpan Das and Soumitra Tarafder. Experimental investigation on martensitic transformation and fracture morphologies of austenitic stainless steel. *International Journal of Plasticity*, 25(11):2222–2247, 2009.

[157] Juho Talonen, Hannu Hänninen, Pertti Nenonen, and Gersom Pape. Effect of strain rate on the strain-induced $\rightarrow$ -martensite transformation and mechanical properties of austenitic stainless steels. *Metallurgical and Materials Transactions A*, 36(2):421–432, 2005.

[158] K. Spencer, M. Véron, K. Yu-Zhang, and J. D. Embury. The strain induced martensite transformation in austenitic stainless steels: Part 1 – influence of temperature and strain history. *Materials Science and Technology*, 25(1):7–17, 2009.

[159] Frank Hahnenberger, Marek Smaga, and Dietmar Eifler. Microstructural investigation of the fatigue behavior and phase transformation in metastable austenitic steels at ambient and lower temperatures. *International Journal of Fatigue*, 69:36–48, 2014.

[160] G. H. Eichelman and F. C. Hull. Effect of composition on the temperature of spontaneous transformation of austenite to martensite in 18-8 type stainless steel. *Transations: American Society for Metals*, page 77–104, 1953.

[161] F. C. Monkman, F. B. Cuff, and N. J. Grant. Computation of ms for stainless steels. *Metal Progress*, 71(4):94, 1957.

[162] Sebastien Allain, J-P Chateau, and O Bouaziz. A physical model of the twinning-induced plasticity effect in a high manganese austenitic steel. *Materials Science and Engineering: A*, 387:143–147, 2004.

[163] R. E. Schramm and R. P. Reed. Stacking fault energies of seven commercial austenitic stainless steels. *Metallurgical Transactions A*, 6(7):1345–1351, 1975.

[164] Francois Abrassart. Stress-induced → martensitic transformation in two carbon stainless steels. application to trip steels. *Metallurgical Transactions*, 4(9):2205–2216, 1973.

[165] Nobuo Nakada, Hidetoshi Ito, Yoshikazu Matsuoka, Toshihiro Tsuchiyama, and Setsuo Takaki. Deformation-induced martensitic transformation behavior in cold-rolled and cold-drawn type 316 stainless steels. *Acta Materialia*, 58(3):895–903, 2010.

[166] Koh-Ichi Sugimoto, Mitsuyuki Kobayashi, and Shun-Ichi Hashimoto. Ductility and strain-induced transformation in a high-strength transformation-induced plasticity-aided dual-phase steel. *Metallurgical Transactions A*, 23(11):3085–3091, 1992.

[167] Greg McMahon, Bryan D Miller, and M Grace Burke. Correlative nanosims and electron microscopy methods for understanding deuterium distributions after fatigue testing of 304/304l stainless steel in deuterated water. *International Journal of Hydrogen Energy*, 45(38):20042–20052, 2020.

[168] James CM Li. Pile-up of dissociated dislocations and the strength-grain size relationship. *Philosophical Magazine*, 19(157):189–198, 1969.

[169] D.H. Lister, R.D. Davidson, and E. McAlpine. The mechanism and kinetics of corrosion product release from stainless steel in lithiated high temperature water. *Corrosion Science*, 27(2):113–140, 1987.

[170] Amar K. De, John G. Speer, David K. Matlock, David C. Murdock, Martin C. Mataya, and Robert J. Comstock. Deformation-induced phase transformation and strain hardening in type 304 austenitic stainless steel. *Metallurgical and Materials Transactions A*, 37(6):1875–1886, 2006.

[171] R. Langneborg. *Acta Met.*, 12:823, 1964.

[172] S.E. Ziemniak and M. Hanson. Corrosion behavior of 304 stainless steel in high temperature, hydrogenated water. *Corrosion Science*, 44(10):2209–2230, 2002.

[173] K. Kruska, S. Lozano-Perez, D Saxey, T Terachi, T Yamada, and G Smith. *15th International Conference on Environmental Degredation of Materials in Nuclear Power Systems - Water Reactors.*

[174] David J. Young. *High temperature oxidation and corrosion of metals.* Elsevier, 2016.

[175] X. Peng, J. Yan, Y. Zhou, and F. Wang. Effect of grain refinement on the resistance of 304 stainless steel to breakaway oxidation in wet air. *Acta Materialia*, 53(19):5079–5088, 2005.

[176] K. Kruska, S. Lozano-Perez, D Saxey, T Terachi, T Yamada, and G Smith. *15th International Conference on Environmental Degredation of Materials in Nuclear Power Systems - Water Reactors*, pages 939–946. 2012.

[177] T Shoji, K Sakaguchi, Z Lu, S Hirano, Y Hasegawa, T Kobayashi, K Fujimoto, and Y Nomura. Effects of cold work and stress on oxidation and scc behavior of stainless steels in pwr primary water environments. *Revue Generale Nucleaire*, 1:50–62, 2014.

[178] Takumi Terachi, Katsuhiko Fujii, and Koji Arioka. Microstructural characterization of scc crack tip and oxide film for sus 316 stainless steel in simulated pwr primary water at 320 c. *Journal of nuclear science and technology*, 42(2):225–232, 2005.

[179] R Soulas, M Cheynet, E Rauch, T Neisius, L Legras, C Domain, and Y Brechet. TEM investigations of the oxide layers formed on a 316L alloy in simulated PWR environment. pages 2861–2871, 2013.

[180] Stephen E Ziemniak, Michael Hanson, and Paul C Sander. Electropolishing effects on corrosion behavior of 304 stainless steel in high temperature, hydrogenated water. *Corrosion Science*, 50(9):2465–2477, 2008.

[181] Sergio Lozano-Perez, David W Saxey, Takuyo Yamada, and Takumi Terachi. Atom-probe tomography characterization of the oxidation of stainless steel. *Scripta Materialia*, 62(11):855–858, 2010.

[182] Tatsuo Maekawa, Masaru Kagawa, and Nobuo Nakajima. Corrosion behaviors of stainless steel in high-temperature water and superheated steam. *Transactions of the Japan Institute of Metals*, 9(2):130–136, 1968.

[183] SE Ziemniak and M Hanson. Corrosion behavior of 304 stainless steel in high temperature, hydrogenated water. *Corrosion Science*, 44(10):2209–2230, 2002.

[184] Torsten Ericsson. Stratified oxide scale growth on two cr-ni steels oxidized in high-pressure steam at 800 c. *Oxidation of Metals*, 2(2):173–205, 1970.

[185] T Ericsson. A study of the cr-depleted surface layers formed on four cr-ni steels during oxidation in steam at 600° c and 800° c. *Oxidation of Metals*, 2(4):401–417, 1970.

[186] M Warzee, C Sonnen, and P Berge. Corrosion of carbon steels and stainless steels in pressurized water at high temperatures. special report no. 9. Technical report, Societe d'Etudes, de Recherches et d'Applications pour l'Industrie, Brussels ..., 1967.

[187] E Schuster, KH Neeb, W Ahlfänger, R Henkelmann, and RT Järnström. Analyses of primary side oxide layers on steam generator tubes from pwrs and radiochemical issues on the contamination of primary circuits. *Journal of Nuclear Materials*, 152(1):1–8, 1988.

[188] T Nakayama and Y Oshida. Identification of the initial oxide films on 18-8 stainless steel in high temperature water. *Corrosion*, 24(10):336–337, 1968.

[189] Tatsuo Maekawa, Masaru Kagawa, Nobuwo Nakajima, and Sadayoshi Nagata. Corrosion of stainless steel in high temperature water. *Transactions of the Japan Institute of Metals*, 5(1):22–27, 1964.

[190] Oli systems. *OLI Systems, Inc.*

[191] Z Zeng, K Natesan, Z Cai, D Gosztola, R Cook, and J Hiller. Effect of element diffusion through metallic networks during oxidation of type 321 stainless steel. *Journal of materials engineering and performance*, 23(4):1247–1262, 2014.

[192] Jonah Erlebacher, Michael J. Aziz, Alain Karma, Nikolay Dimitrov, and Karl Sieradzki. Evolution of nanoporosity in dealloying. *Nature*, 410(6827):450–453, 2001.

[193] Carl Wagner. Reaktionstypen bei der oxydation von legierungen. *Zeitschrift für Elektrochemie, Berichte der Bunsengesellschaft für physikalische Chemie*, 63(7):772–782, 1959.

[194] N Mortazavi, C Geers, M Esmaily, V Babic, M Sattari, K Lindgren, P Malmberg, B Jönsson, M Halvarsson, JE Svensson, et al. Interplay of water and reactive elements in oxidation of alumina-forming alloys. *Nature materials*, 17(7):610–617, 2018.

[195] Majid Nezakat, Hamed Akhiani, Sami Penttilä, Seyed Morteza Sabet, and Jerzy Szpunar. Effect of thermo-mechanical processing on oxidation of austenitic stainless steel 316l in supercritical water. *Corrosion Science*, 94:197–206, 2015.

[196] Marc Vankeerberghen. Model for a spinel oxide film on an an fe-cr-ni alloy, ss304. In *16th International Conference on Environment Degradation of Materials in Nuclear Power Systems - Water reactors*, 8 2013.

[197] Jukka Vaari. Molecular dynamics simulations of vacancy diffusion in chromium (iii) oxide, hematite, magnetite and chromite. *Solid State Ionics*, 270:10–17, 2015.

[198] Masaki Mizouchi, Yoshihiro Yamazaki, Yoshiaki Iijima, and Koji Arioka. Low temperature grain boundary diffusion of chromium in sus316 and 316l stainless steels. *Materials transactions*, 45(10):2945–2950, 2004.

[199] Gerald H Meier, Keeyoung Jung, Nan Mu, Nazik M Yanar, Frederick S Pettit, J Pirón Abellán, Tomasz Olszewski, L Nieto Hierro, Willem J Quadakkers, and Gordon R Holcomb. Effect of alloy composition and exposure conditions on the selective oxidation behavior of ferritic fe–cr and fe–cr–x alloys. *Oxidation of Metals*, 74(5):319–340, 2010.

[200] Jun Takada, Sadahiro Yamamoto, and Masao Adachi. Diffusion coefficient of oxygen in alpha-iron determined by internal oxidation technique. *Zeitschrift fuer Metallkunde/Materials Research and Advanced Techniques*, 77(1):6–11, 1986.

[201] William C Hagel. Anion diffusion in α-cr2o3. *Journal of the American Ceramic Society*, 48(2):70–75, 1965.

[202] Langli Luo, Mao Su, Pengfei Yan, Lianfeng Zou, Daniel K Schreiber, Donald R Baer, Zihua Zhu, Guangwen Zhou, Yanting Wang, Stephen M Bruemmer, et al. Atomic origins of water-vapour-promoted alloy oxidation. *Nature materials*, 17(6):514–518, 2018.